

The Effect of Liquid Viscosity on the Polygonal Instabilities Observed  
within Hollow Vortex Core

Amr Mandour

A Thesis

In

The Department

of

Mechanical and Industrial Engineering

Presented in Partial Fulfilment of the Requirements

for the Degree of Master of Applied Science (Mechanical Engineering) at

Concordia University

Montreal, Quebec, Canada.

June 2010

© Amr Mandour, 2010



Library and Archives  
Canada

Bibliothèque et  
Archives Canada

Published Heritage  
Branch

Direction du  
Patrimoine de l'édition

395 Wellington Street  
Ottawa ON K1A 0N4  
Canada

395, rue Wellington  
Ottawa ON K1A 0N4  
Canada

*Your file* *Votre référence*  
ISBN: 978-0-494-70960-3  
*Our file* *Notre référence*  
ISBN: 978-0-494-70960-3

#### NOTICE:

The author has granted a non-exclusive license allowing Library and Archives Canada to reproduce, publish, archive, preserve, conserve, communicate to the public by telecommunication or on the Internet, loan, distribute and sell theses worldwide, for commercial or non-commercial purposes, in microform, paper, electronic and/or any other formats.

The author retains copyright ownership and moral rights in this thesis. Neither the thesis nor substantial extracts from it may be printed or otherwise reproduced without the author's permission.

#### AVIS:

L'auteur a accordé une licence non exclusive permettant à la Bibliothèque et Archives Canada de reproduire, publier, archiver, sauvegarder, conserver, transmettre au public par télécommunication ou par l'Internet, prêter, distribuer et vendre des thèses partout dans le monde, à des fins commerciales ou autres, sur support microforme, papier, électronique et/ou autres formats.

L'auteur conserve la propriété du droit d'auteur et des droits moraux qui protègent cette thèse. Ni la thèse ni des extraits substantiels de celle-ci ne doivent être imprimés ou autrement reproduits sans son autorisation.

---

In compliance with the Canadian Privacy Act some supporting forms may have been removed from this thesis.

Conformément à la loi canadienne sur la protection de la vie privée, quelques formulaires secondaires ont été enlevés de cette thèse.

While these forms may be included in the document page count, their removal does not represent any loss of content from the thesis.

Bien que ces formulaires aient inclus dans la pagination, il n'y aura aucun contenu manquant.

  
**Canada**

## Abstract

### **The Effect of Liquid Viscosity on Polygonal Pattern Instability Observed within Hollow Vortex Core**

Amr Mandour

The dynamics of liquid vortices generated by rotating a flat disc near the bottom of a cylindrical tank is investigated experimentally. Several former investigations have found that the main parameters affecting the flow behaviour are incorporated in two non-dimensional numbers: Reynold's number and the aspect ratio. Despite some evidence of the important role of fluid viscosity on the polygonal pattern instability behaviour observed within the hollow vortex core, a systematic study has not yet been carried out. This thesis examines the role of viscosity in the development, evolution, wave speed propagation and the overall transition of vortex core instabilities. The data analysis was performed using the digital image processing technique. Increasing the viscosity of the fluid by mixing glycerol with tap water at room temperature, was found to significantly decrease the polygonal patterns' limits of endurance and distort their geometry until all mode shapes were eventually destroyed and never recognized, beginning with high mode shapes progressively until the lower polygonal patterns are reached. Increasing the fluid viscosity to 22 times that of water resulted into an up to 25% augmentation of the maximum polygonal pattern speed. In all cases, the pattern speed ( $f_p$ ) was found to be almost  $1/3$  the disc speed ( $f_d$ ), which confirms the pure water results obtained by Vatistas et al. (2008). The effect of varying the viscosity on the transitional processes between subsequent polygonal patterns is also addressed in this thesis. Alike to the case of pure water, the transition between polygonal patterns is found to occur in two stages: a quasi-periodic phase followed by frequency locking.

## **Acknowledgements**

It has been an honour for me to work under the supervision of Dr. Vatistas and Dr. Ng. This thesis could not be completed without their encouragement, support and guidance.

I would also like to express my deepest appreciation to my friends Dr. Ait Abderrahmane and Dr. Fayed for their continuous advice and guidance. Dr. Kadem and Amy-Lee Gunter also contributed to the completion of this thesis.

I would like to thank Mr. Huard and Mr. Szczawinski from the Mechanical Engineering Department for the technical support they have provided during my research work.

I am sincerely grateful to my family, especially my father, Dr. Mandour for their moral and financial support during the past years. A special thank you goes to my fiancée for her patience, support and understanding.

## Table of Contents

<b>List of figures</b> .....	<b>vii</b>
<b>List of Tables</b> .....	<b>ix</b>
<b>Nomenclature</b> .....	<b>x</b>
<b>Chapter 1</b>	
<b>Introduction</b> .....	<b>1</b>
1.1 General.....	1
1.2 Swirling flow within cylindrical container .....	2
1.3 Polygonal patterns in different studying fields .....	3
1.4 Polygonal patterns in swirling flows.....	4
1.5 Motivation of the present study .....	11
1.6 Objective of the present study.....	11
<b>Chapter 2</b>	
<b>Experimental set-up and measuring techniques</b> .....	<b>13</b>
2.1 Experimental set-up .....	13
2.2 Measuring technique.....	15
2.2.1 Pattern's speed measurement.....	16
2.2.2 Disc's speed measurement and control .....	25
<b>Chapter 3</b>	
<b>The effect of liquid viscosity on polygonal instability behaviour</b> .....	<b>27</b>
3.1 Effects of flow parameters on polygonal pattern instability .....	27
3.2 The influence of viscosity on polygonal patterns formation and limits of endurance .....	29
3.2.1 Initial height $h_i = 20$ mm.....	30
3.2.2 Initial height $h_i = 30$ mm .....	32
3.2.3 Initial height $h_i = 40$ mm.....	33

3.3 Density influence on patterns formation.....	36
3.4 Polygonal pattern's frequency variation .....	38
3.4 Effect of density on pattern's rotating frequency.....	47
3.5 Concluding remarks .....	49
<b>Chapter 4</b>	
<b>Influence of viscosity on the transitional process between polygonal patterns .....</b>	<b>51</b>
4.1 Symmetry breaking in swirling flows.....	51
4.2 Transition between equilibrium states using water as the working fluid.....	53
4.2.1 Initial height $h_i = 40$ mm .....	53
4.2.2 Initial height $h_i = 20$ mm .....	63
4.3 Transition between equilibrium states using aqueous glycerol as the working fluid.....	65
4.3.1 Confirmation of the quasi-periodic stage in polygonal patterns transition .....	66
4.4 Concluding remarks .....	71
<b>Chapter 5</b>	
<b>Conclusion .....</b>	<b>74</b>
5.1 Contribution to knowledge.....	77
<b>Appendix A.....</b>	<b>82</b>
MATLAB algorithm .....	82
Experimental apparatus.....	85
Viscosity of aqueous glycerine solutions.....	86

## List of figures

<b>Figure 1</b> Experimental set-up. ....	14
<b>Figure 2</b> Polygonal patterns observed within hollow vortex core. ....	16
<b>Figure 3</b> (a) Dark image and its corresponding histogram; and (b) Same image and its corresponding histogram after the histogram copying technique was applied. ....	18
<b>Figure 4</b> (a) Original 8-bit gray-scale image acquired by camera; (b) Binary format (thresholded); (c) Extracted pattern boundary; and (d) Superposition of the extracted boundary on original image. ....	19
<b>Figure 5</b> Signature of the extracted boundary. ....	20
<b>Figure 6</b> Radial displacement time series at 10° angular orientation. ....	21
<b>Figure 7</b> Power spectrum of the processed set of images. ....	22
<b>Figure 8</b> MATLAB algorithm flowchart. ....	24
<b>Figure 9</b> Disc's speed controller loop. ....	26
<b>Figure 10</b> Kinematic viscosity vs. glycerol concentration. ....	30
<b>Figure 11</b> Phase diagram for polygonal patterns observed through the viscosity domain at $h_i = 20$ mm. .	31
<b>Figure 12</b> Phase diagram for polygonal patterns observed through the viscosity domain at $h_i = 30$ mm. .	33
<b>Figure 13</b> Phase diagram for polygonal patterns observed through the viscosity domain at $h_i = 40$ mm. .	35
<b>Figure 14</b> a) Oval pattern at constant parameters condition but three different viscosities; and (b) Triangular pattern at constant parameters condition but three different viscosities. ....	36
<b>Figure 15</b> Phase diagram for three different heights using water and brine as the working fluids. ....	37
<b>Figure 16</b> (a) Power spectra superposition for triangular pattern at three different heights; and (b) Power spectra superposition for all mode shapes at $h_i = 40$ mm. ....	39
<b>Figure 17</b> (a) Power spectra superposition for triangular pattern using three different viscosity fluids; and (b) Power spectra superposition at $h_i = 40$ mm for all mode shapes using a mixture with $4 \times \mu_{\text{water}}$ . ....	41
<b>Figure 18</b> (a) Pattern's frequency propagation with increasing disc's speed (b) Linear fitted slopes for frequency propagation. ....	43
<b>Figure 19</b> (a), (b) Pattern's frequency propagation with increasing disc's speed; and (c) Linear fitted slopes for frequency propagation at $h_i = 40$ mm. ....	45
<b>Figure 20</b> Linear fitted slopes for frequency propagation at $h_i = 20$ mm. ....	46

<b>Figure 21</b> (a) Power spectra superposition for triangular pattern using brine at three different heights; (b) Power spectra superposition at $h_i = 20$ mm for all mode shapes using brine; and (c) Linear fitted slopes for frequency propagation. ....	48
<b>Figure 22</b> (a), (b), (c) Oval pattern progression and corresponding power spectra; and (d) Oval to triangular transition $N=2$ to $N=3$ and corresponding power spectrum. ....	56
<b>Figure 23</b> (a), (b), (c) Triangular pattern progression and corresponding power spectra; (d) Transitional process from triangular to square pattern; and (e) Square pattern and corresponding power spectra.....	59
<b>Figure 24</b> Quasi-periodic state during triangular to square transition.....	62
<b>Figure 25</b> (a) Square to pentagonal transition; and (b) Pentagonal to hexagonal transition. ....	64
<b>Figure 26</b> Power spectrum for $N=2$ pattern replica.....	68
<b>Figure 27</b> Power spectrum of transition processes using patterns replica (a) $N=2$ to $N=3$ ; and (b) $N=3$ to $N=4$ .....	70
<b>Figure 28</b> Experimental apparatus .....	85



## List of Tables

<b>Table 1</b> Transition mode-locking frequencies for different viscosity fluids. ....	65
<b>Table 2</b> Patterns replica with corresponding functions. ....	67
<b>Table 3</b> Viscosity of aqueous glycerine solutions.....	86

## Nomenclature

$N$	Pattern's corners (sides)	number
$h_i, H$	Liquid's initial height	mm
$R$	Disc radius	m
$\tau_e$	Ekman time	s
$\nu$	Kinematic viscosity	m <sup>2</sup> /s
$f_d$	Disc's frequency	Hz
$f_p$	Pattern's frequency	Hz
$f_m$	Most powerful frequency	Hz
PSD	Power spectrum density	dB
$\mu_{\text{water}}$	Dynamic viscosity of water at room temperature	Pa·s

# Chapter 1

## Introduction

### 1.1 General

Vortex refers to the fluid motion in which the streamlines form concentric circles. Everyday vortices can be generated naturally or artificially, and their size may vary from a few centimetres to kilometres. Typical naturally occurring vortices include the geophysical vortices such as tornadoes, hurricanes, waterspouts, polar vortices, and circulation of oceans as well as the general circulation of the atmosphere and convection of clouds. This phenomenon is not restricted to Earth, in fact vortices are also observed in planetary atmospheres and in the motion of galaxies. The large impact of vortices in nature on human beings, makes it a topic of great interest to be explored, and this research eventually applied to industrial processes. In industry, vortices are generated by wing tips, cavitation behind propellers, cyclone combustion, vortex valves, swirl atomizers, drain holes and many others. Thus the effect of this line of research is far reaching and vastly beneficial.

Vortex dynamics has been a very significant element of fluid dynamics studies for many years. Hermann von Helmholtz (1858), the German physician, first introduced the three governing laws of vortex motion in his paper on hydrodynamic equations, which has been translated and published in English. This was followed by Kelvin's (1869) circulation theorem which stated that the circulation around a closed path in an inviscid flow is always conservative. In 1878, Alfred Mayer came out with the floating magnets experimental work modeling the appearance of electron configurations inside a molecule. By placing a large magnet with its South Pole pointing towards a bowl of water containing magnetized needles floating on the

surface, he found that the needles formed symmetric polygonal oriented configurations. Following Mayer, Lord Kelvin (1878) considered Helmholtz and Mayer's work in introducing his Vortex Atom Theory in which he represented atoms as point vortices rotating in a perfect fluid (aether). Many followers have contributed to Kelvin's work, but only from the hydrodynamic point of interest, to study the vortex dynamics.

## **1.2 Swirling flow within cylindrical container**

Vortices and symmetrical pattern formation are also experienced in laboratory experiments featuring swirling flows within cylindrical containers. One of the most interesting experiments is the one performed by Vatistas (1990) whereby swirling flow was developed within a cylindrical container by a rotating disc near its bottom under shallow water conditions. Continuous spinning up of the disc resulted in a gradual intensification of the swirling flow of the contained water. The flow remains symmetric and laminar at a relatively low rotational speed of the disc until a critical speed is reached and symmetry breaking phenomenon takes place. Two main flow regimes are speculated in such flow. The first is the rotating azimuthal flow as a result of the inertia forces generated by shearing between the rotating disc and the water in contact. The second flow is produced by both gravitational and centrifugal forces. The latter pushes the water radially outwards, towards the container's stationary side wall, where it rolls up due to the strong meridional forces produced by the shear layer flow along the side wall. Finally the water rotates back to the axis of symmetry of the flow, and therefore completes a secondary cyclic flow. When the vertex of the main vortex core touches the top surface of the disc, a circular portion of the disc becomes exposed, as seen from above. As the flow is further intensified, the circular vortex core is transformed into a series of progressive vortex core shapes starting from oval, and

progressing through triangular, square and pentagonal-like shapes, and terminating with hexagonal rotating cores.

### **1.3 Polygonal patterns in different studying fields**

The symmetric polygonal patterns observed in the arrangements of the magnetic needles in Mayer's experiments (1878) as well as in the hydrodynamics flow (such as the swirling flow, Vatistas 1990) were also experienced in many experiments in different physical fields. For example in space, Mason (1971) also observed similar shaped trajectories by a floating balloon above the South Pole in an attempt to study the global circulation of the atmosphere numerically. Ultraviolet stereographic images of the South pole of Venus taken from Mariner 10 showed an oval vortex cloud which was considered to be different from the rest of Venus cloud cover (Suomi & Limaye 1978). Moreover, Godfrey (1988) observed a hexagonal shape composed of rotating clouds at the north pole of Saturn at the radio rotation period, which was later explained, by Allison et al. (1990), as being a stationary Rossby wave. Numerical simulations done by Polvani and Dritschel (1993) on the dynamics of vortices on the surface of a sphere showed point vortices with oval ( $N=2$ ) up to hexagonal ( $N=6$ ) patterns. Similar polygonal shapes were also observed in nature; Maxworthy (1973) studied the topology of large scale dust devils and tornados using observable analysis. Using a Doppler radar, Bluestein and Pazmany (1999) featured asymmetric waves, eye cores, multiple vortices and spiral bands along the edge of the eye walls of tornadoes. In addition, Davies-Jones et al. (1986) found that the tangential speed of wind inside a tornado is almost linear with the core radius of the tornado, therefore, confirming a solid-body rotation for tornadic flows which features Rankine vortex flow. In optical experiments, similar polygonal patterns are observed by twisting a light beam along its axis of

propagation and projecting it onto a flat surface, a ring of light with dark center is observed known as optical vortex. Curtis and Grier (2004) observed polygonal geometries by modulating the optical vortices and they were able to observe particle trajectory patterns from oval  $N=2$  up to hexagonal flower shape pattern  $N=6$ .

In laboratory experiments, Gregory et al. (1955), using a china-clay coated rotating disc, recorded traces of six symmetrically oriented vortices. Moreover, Yarmchuk et al. (1979) observed and photographed both stationary, symmetric ( $N=1$  till 5) and distorted, asymmetric ( $N=6$  till 10) polygonal patterns when rotating superfluid helium. Due to the difficult conditions experienced near absolute zero they were unable to study the stability of these patterns. Also, on their experiments in pure electron plasmas, Driscoll and Fine (1990) were able to represent two dimensional vortex dynamics through magnetically confined columns of electrons forming both stable and unstable diocotrons modes. Recently, Ellegaard et al. (1998) using high viscous fluids, experienced stationary polygonal patterns when a vertical jet of liquid hits a flat ground at high Reynolds number.

#### **1.4 Polygonal patterns in swirling flows**

Swirling flows generated by rotation of one or multiple end walls and/or side walls in cylindrical containers have revealed the existence of similar polygonal patterns experienced in nature and the other mentioned experiments. The correspondence between both phenomena has inspired many investigations by researchers in studying swirling flows. Swirling flows dynamics in both closed and open containers depends mainly on two parameters: the Reynolds number (flow intensity) and the aspect ratio (height  $H$  to radius  $R$  ratio). The behaviour of the flow is significantly different in shallow and deep liquid conditions (Lopez et al. 2004). On one hand, in

deep configurations, ( $H/R > 1$ ), the symmetry breaking is mainly due to the jet-like shear layer near the boundaries which is forced towards the interior of the flow defining an internal solid-body vortex core rotation (Hirsa et al. 2002). On the other hand, in shallow liquid formation, the polygonal bifurcations are due to the extended solid body rotation region which becomes dominant to almost half the radius of the container, the boundary layer between the boundary jet-like shear layer and the interior body rotation is unstable which develops azimuthal rotating waves (Miraghaie et al. 2003). Mainly the meridional component of the flow field characterizes the flow behaviour; in small radii containers, the weak meridional flow develops the solid body rotation while for larger radii, the meridional effects are dominant and form the jet-like boundary. Not only the Reynolds number and aspect ratio play an important role in the dynamics of the swirling flow, but also the boundary conditions significantly affect the symmetry breaking and stability in such flows. Swirling flows in completely enclosed tanks are different from those experienced in open free surface counterparts. The first experimental study on swirling flows in an enclosed cylindrical container fully filled with liquid was performed by Vogel (1968). He observed and defined a stability range, in terms of aspect ratio and Reynolds number, for a vortex breaking phenomenon in the form of a bubble along the container's axis of symmetry. Escudier (1984) confirmed and further extended the earlier experiment, using laser-induced fluorescence technique. By increasing the aspect ratio and changing the working fluid properties, he recognised two further stability regions where two and three successive vortex breakdown bubbles are observed, respectively. At low Reynolds number the flow is fully axisymmetric. Further increasing the swirling flow, vortex breakdown took place followed by fully turbulent flow behaviour at high Reynolds number. Spohn et al. (1993) studied the effect of the existence of top endwall by reproducing Vogel's (1968) and Escudier's (1984) experiments but in an open

free surface cylindrical tank with a rotating bottom and found that the free surface affects significantly the formation and location of vortex core break down. Brøns et al. (2001) studied the spatial properties of such breakdown bubbles. Lopez (1998) and Lopez et al. (2002, 2006) studied swirling flows by rotating a cylindrical container completely filled with water with a co-rotating or counter rotating top endwall, both numerically and experimentally. Generally, at low rotational speed whether the top endwall is co-rotating or counter-rotating, the flow structure is steady and axisymmetric. However as the lid's relative rotational velocity to the cylinder rotational speed increases, the flow undergoes different flow behaviours. At high relative velocities, Lopez et al. (2002) observed stable azimuthal rotating waves with 4 and 5 lobes co-existing at a specific base Reynolds number and aspect ratio extending along a range of relative speeds. As the Reynolds number increased, a flow separation took place at the top endwall producing a free shear layer that resulted in a symmetry breaking configuration characterized by Hopf bifurcation.

As mentioned earlier, the general swirling flow is divided into the internal solid body rotation and the exterior shear layer jet-like flow. The interaction of both regions at their interface defines the behaviour and transitional development of the swirling flow.

Gallaire and Chomaz (2003), using a Rankine vortex model, were able to predict such interactions responsible for producing these instabilities. They showed numerically that Coriolis forces affect both regions significantly, leading to inertial Kelvin waves along the boundary of the interior core shape, while the exterior shear layer region is prone to dominant centrifugal forces which are opposed by radial pressure gradients producing instabilities known as centrifugal instabilities. The interactions between both regions undergo a Kelvin-Helmholtz instability, where small perturbations grow first to form waves before they roll up into vortices



conferring the interface polygonal pattern. Also, they have pointed out a possible coupling and resonance between Kelvin-Helmholtz and inertia waves.

Many experiments on swirling flows in cylindrical containers under shallow water conditions were concerned with studying the stability of the shear layer flow known as barotropic instability, observed in oceans and atmosphere, as well as the laminar to turbulent transitional flow. Hide and Titman (1967) used a cylindrical reservoir with a rotating endwall mounted on an independently rotating table and were able to study the stability of shear layer eddies formed along the inner cylindrical ring boundary. Below a critical relative rotating speed value between the disc and table was reached, the flow was axisymmetric. As the basic flow is further intensified, they experienced the formation of a regular rotating pattern with eddies located along its shear zone. The number of eddies were found to be decreasing with the rotating intensity of the flow. Later, Niño and Misawa (1984) using counter rotating concentric cylinders similar to the set-up of Hide and Titman (1967), characterized the flow based on Reynolds number and found that the number of eddies formed along the shear zone layer of the inner cylinder decrease with increasing Reynolds number. Although this confirmed the results of Hide and Titman (1967), they found it opposing to the expected results of the linear stability theory which states that the number of eddies or wave number should increase with Reynolds number (shear). Another interesting phenomenon encountered in their experiments was the fact that, as soon as the Reynolds number has exceeded a certain critical value, they recognized more than one stable, steady formation number of waves for the same Reynolds number on different runs. Yasushi (1999) and many others, also studied swirling flows transitions in Taylor (Couette) set up where the inner cylinder is rotating and the outer cylinder is stationary. Again, he recognized symmetry breaking as the relative rotating speed passed a critical value (Critical Reynolds

number). Fröh and Read (1999) also performed similar experiments studying the barotropic instability using a rotating cylinder filled with water, and both bottom and top endwalls relatively rotating and have observed similar shear layer break up forming  $N$  azimuthal wave vortices up to  $N=8$ .

The stability of circular shear layer with the thickness of the same order or less than the Ekman layer was investigated in the conditions where the effects of the centrifugal and Coriolis forces were minor, see Rabaud & Couder (1983) and Chomaz et al. (1988). Their observations considered the aspect ratio of the containing reservoir to be the determinant of the flow behaviour, the number of experienced rotating vortices, as well as, the transitional behaviour which followed two different routes depending on the container radius.

The recent study by S. Poncet and M.P Chauve (2007) on the shear-layer instability in a free surface tank using a rotating disk near the bottom with an inner concentric hub of different radii confirmed the results of Chomaz et al.(1988); assigning the Reynolds number, aspect ratio and the ratio of concentric cylinders radii as the their control parameters, they visualized and recorded clear steady axisymmetric rotating flow until a critical Reynolds number is reached where a consistent rotating polygonal pattern with  $N$  vortices at its sharp corners appeared. The number of  $N$  vortices ranging from 2-8 decreased with increasing Reynolds number, aspect ratio and radii ratio. At comparably high hub radii values to the disk, the rotating vortices were no longer recognized, instead they appeared as stationary point waves attached along the hub boundary. Since the number of vortices depends on the Ekman number which is based on the fluid depth, they characterized the flow instability being similar to the detached shear layer instabilities known as Stewartson shear layers (Stewartson 1957).

Poncet and Chauve (2007) experiments with no inner hub (radii ratio = 0) resemble to a large extent the ones performed by Vatistas (1990), who first reported an interfacial symmetry breaking (between solid (disc), liquid (working fluid) and gas (air)) of the hollow vortex core within a cylindrical tank with a rotating disk near its bottom. Both experiments were performed with free surface configuration under shallow water conditions. Although both experiments exhibited mainly two flow regions, an inner body rotation and an outer shear layer flow, Vatistas (1990) reported polygonal patterns with satellite vortices located at its vertices rotating around within the inner body rotation region with a dry core. On the other hand, Poncet and Chauve (2007) found the polygonal patterns to be the boundary distinguishing between the outer shear flow region and the inner two dimensional solid body region. In addition, Vatistas (1990) reported an increase in the number of polygonal sides (vortices) as the flow was intensified while Poncet and Chauve (2007) found the number of rotating vortices defining the polygonal sides to decrease with increasing the rotating disk speed. However, one should take into consideration that the ranges of flow speed and aspect ratio are much higher in Vatistas observations than Poncet and Chauve (2007). From the difference in flow behaviours stated above and the different swirling flows instabilities discussed earlier, one could predict that most likely the instability mechanisms leading to the pattern formation in Poncet and Chauve (2007) observations were due to Kelvin-Helmholtz instability while in Vatistas' experiments, the mechanism seemed to be the inertial instability (Kelvin waves).

These distinctions between the two experiments might explain the differences in bifurcation scenarios, polygonal shapes rotational speed as well as the flow transitional behaviour from one steady state (polygonal shape) to the other. The maximum number of waves (vortices) observed by Vatistas (1990) were six while Poncet and Chauve (2007) visualized and

recorded up to eight steady equally distributed vortices. The polygonal patterns observed in Vatistas (1990), Poncet and Chauve (2007) and Chomaz et al. (1988) became unstable when the control parameter (Reynolds number) exceeded a certain critical value. During spin up, bifurcations from one polygonal shape  $N$ -gon to  $(N+1)$ -gon were observed in Vatistas (1990) and  $N$ -gon to  $(N-1)$ -gon in both Poncet and Chauve (2007) and Chomaz et al. (1988). Chomaz et al. (1988) using two dimensional numerical simulation of swirling flows were able to thoroughly explain the difference in flow transition from one polygonal pattern to another based on the aspect ratio of the flow. For low aspect ratios, where high numbers of vortices were reached, the transition occurred in a very short time more like sudden flow behaviour while at high aspect ratios, the flow went through bifurcations and symmetrically breaking for the entire flow until it receded back to its new stable state. Through flow visualisation and spectral analysis they showed that the series of bifurcations were supercritical and they were analogous to the well known sub harmonics cascade that leads to turbulence.

Recent studies by Jansson et al. (2006) and Vatistas et al. (2008) triggered a rejuvenated interest in the interfacial symmetry-breaking of hollow vortex core first observed by Vatistas (1990). Jansson et al. (2006) who confirmed the earliest observations of Vatistas (1990) independently found the rotational speed of the polygonal patterns to vary in a complicated way with increasing disc speed, while Vatistas et al. (2008) showed a constant mode-locking speed for all patterns at different aspect ratios. Vatistas et al. (2008) also considered the transitional processes between different patterns and found them to follow a certain spectral development. Both Vatistas (1990) and Jansson et al. (2006) found the initial conditions in their experiments having no crucial effects on the flow behaviour other than producing minor hysteresis associated with the spin up and spin down sequence of flow transitions.

## **1.5 Motivation of the present study**

Whether in open or closed, single or multiple rotating endwalls and/or side walls, all previously discussed studies have considered the Reynolds number and the aspect ratio as being the two main (dimensionless) parameters controlling the flow behaviour. Moreover, all studies concerning symmetry breaking of axisymmetric flows considered the shear to play a crucial role in the flow behaviour and transition development. Although the working fluid's viscosity is expected to vary the entire shear behaviour along the boundary (Greenspan 1990) between different flow regions as mentioned earlier, as well as, the shear layer along the cylinder end and side walls, apparently, none of the above mentioned studies considered the kinematic viscosity of the working fluid as the primary control parameter which was found to influence the interfacial symmetry-breaking of swirling flows in free surface configuration. Using ethylene glycol (kinematic viscosity =15 times greater than water) as the working fluid, Jansson et al. (2006) observed similar polygons but with no more than three rotating vortices while recording up to  $N=6$ -gons when using water instead, under same experimental conditions. Also, Vatistas et al. (1992), under same experimental conditions of water, used Shell motor oil (kinematic viscosity of two orders of magnitude greater than water) as the working fluid and observed similar but unpredictable sequence of rotating vortices with wave numbers up to  $N=11$ . A systematic study on the effect of viscosity on the symmetry-breaking phenomenon is of great fundamental interest. Such study will help to develop the understanding of the phenomenon's mechanism and give a broad explanation for the phenomenon's varying parameters.

## **1.6 Objective of the present study**

In this thesis, the effect of the working fluid viscosity on the polygonal patterns

behaviour is investigated. Experiments were carried out in the set-up similar to Vatistas et al. (2008). The apparatus was modified to allow more accurate control and measurements. Specifically, the study will analyze, with the aid of image processing, the polygonal patterns formation, the limits of endurance, rotational speed variation and finally, the flow transitional behaviour between subsequent polygonal patterns

## Chapter 2

### Experimental set-up and measuring techniques

#### 2.1 Experimental set-up

The schematic of the experimental set-up used in all experiments is given in figure 1. This consisted of a stationary transparent cylindrical container made of plexiglass with an internal diameter of 284 mm. A 7 mm thick, 252 mm in diameter aluminum disc was screwed, 20 mm above the cylinder bottom, to a rotating vertical shaft which rested on a bearing and was connected to an electric motor through a rubber V-belt. A flywheel was attached to the shaft to enhance the constancy of the disc rotation and to compensate for any inertial losses. All components were mounted and supported on a heavy steel table standing on four shock absorber pads to minimize vibrational disturbances at high rotational speeds. Experiments with tap water, brine and aqueous glycerol mixture, as the working fluids, were conducted at three different initial liquid heights ( $h_i$ ) of 20, 30 and 40 mm above the rotating disc. A circular neon light was placed concentrically around the transparent vinyl coated cylinder for even distribution of light. A digital CMOS high-speed camera (pco.1200hs) with a resolution of 1280 x 1024 pixels was placed vertically above the cylinder using a tripod. A ruler was attached to the cylinder's wall for measuring the initial liquid height. A plastic beaker was used for measuring the liquid volumes. The viscosities of the used mixtures were obtained through technical data provided by a registered chemical company (Dow). A mercury glass thermometer was used to measure the working fluid's temperature variation before and after experimental runs.

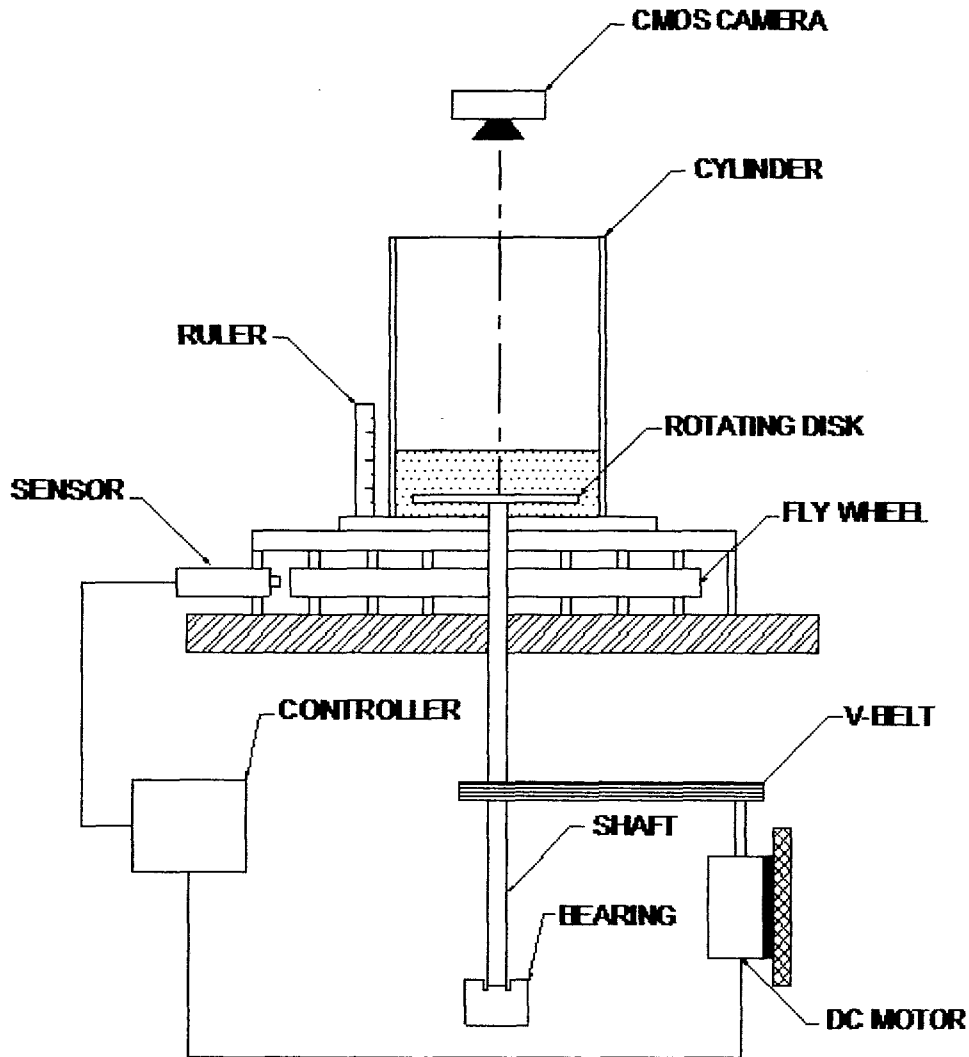


**Figure 1** Experimental set-up.

A kill switch was introduced to the system as a safety precaution in case of emergency. For better contrast between the liquid and the disc, the rotating disc was coated with a white opaque vinyl sheet and a soluble black dye was mixed with the working fluid before each experiment. The disc was rotated in the counterclockwise direction, and its speed was measured and controlled using a digital PID controller loop implemented on LABVIEW environment. The wobbling of the rotating disk was measured using a dial gauge and minimized, using a sand



sheet, to 30 micro inches axially and 5 micro inches eccentricity. The disc speed, liquid initial height and viscosity were the control parameters in this study.

## 2.2 Measuring technique

As the disc started rotating and at low rotational speeds, the liquid started moving gradually with the disc motion. The liquid at the axis of symmetry was moved outwards in the direction of the cylinder walls due to centrifugal forces and therefore, the liquid height in contact with the side wall increased gradually. The interaction between gravitational and centrifugal forces resulted in a wide-mouthed bell shaped free surface of the liquid. As the rotational speed of the disc, therefore the rotating fluid, went higher the vertex of the bell shaped free surface touched the surface of the disc exposing a hollow white portion of the disc. Further increase of the disc speed resulted in the formation of a sequence of polygonal patterns, with dry circular centers, ranging from oval up to hexagon patterns (see figure 2 for illustration). The CMOS camera acquired both coloured RGB and 8-bit gray-scale images, at 30 frames per second, for the top view of the formed polygonal patterns. The colored images were used in this thesis for better visualization of the patterns structure (as will be discussed in Chapter 4). On the other hand, the analysis of the data was conducted using the gray-scale images since they are simpler to deal with in image processing (as will be discussed in the next section). To avoid blurred images, the shutter speed of the camera was set to a maximum of 1/510 seconds. The shutter speed could not be further increased due to lighting limitation. Although the disc speed ranged, where all patterns appeared, from 1.7 to 5 Hz, the rotating pattern speed (as will be shown later) ranged only from 0.75 to 1.25 Hz and therefore, a sampling frequency of 30 fps was sufficient enough for the pattern's rotational speed measuring technique used in this thesis.

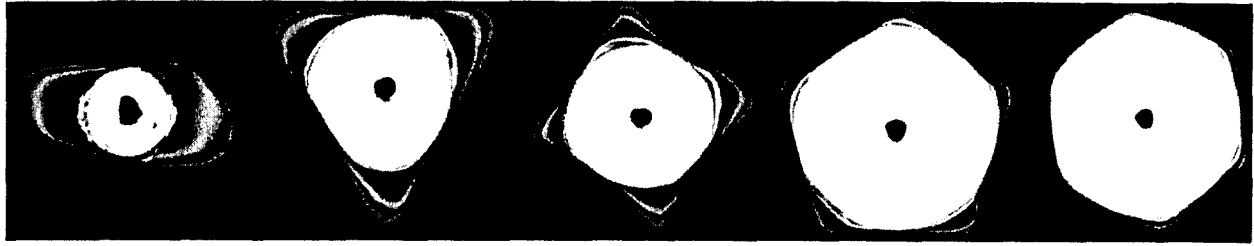


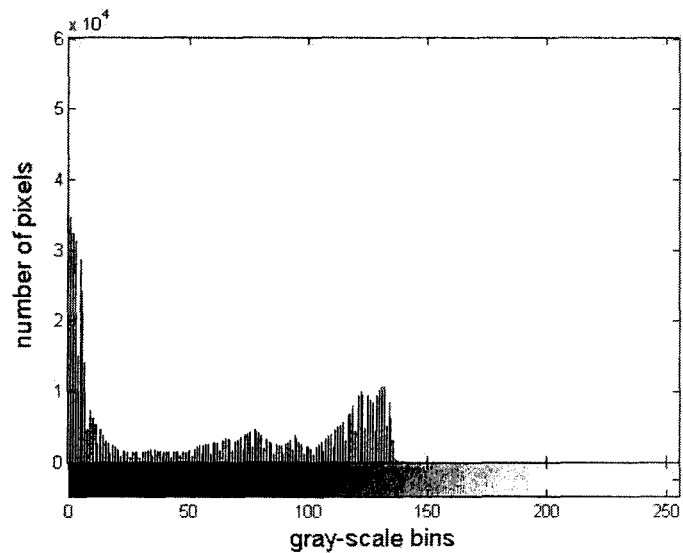
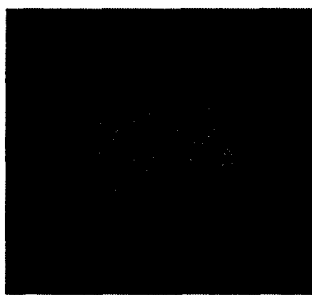
**Figure 2** Polygonal patterns observed within hollow vortex core.

### 2.2.1 Pattern's speed measurement

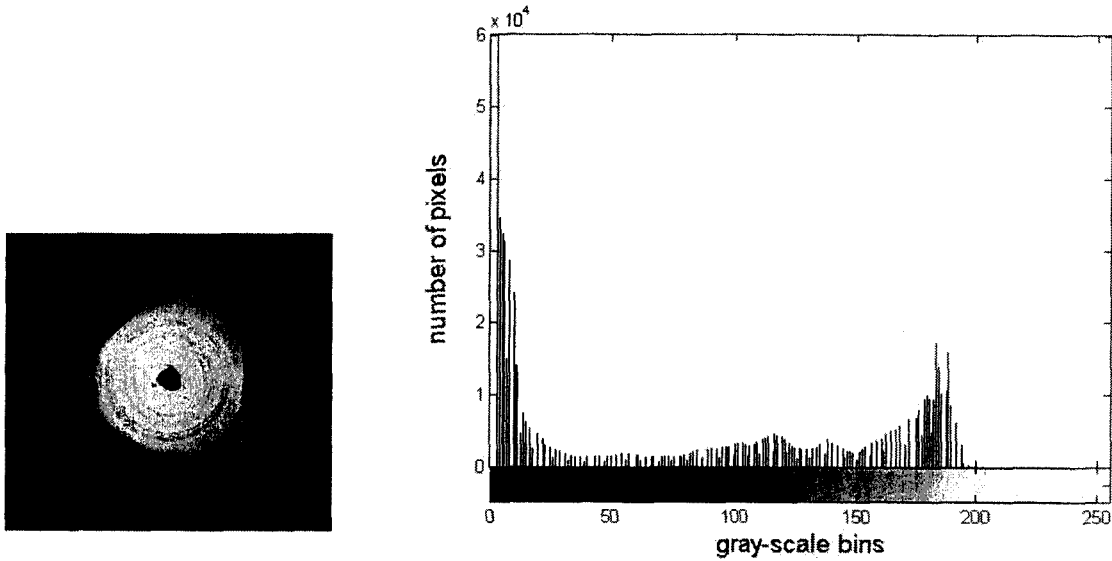
During all experiments, disc speed increments of 1 RPM have been used to ensure continuous shear propagation (S. Poncet and M. P. Chauve 2007). Sufficient time has been let between increments to ensure stabilized flow. This time was referenced by the Ekman time ( $\tau_e = R/\sqrt{\nu fd}$ ) which characterizes the evolution time in swirling flows (Greenspan 1990). For each three increments (3 RPM range) of the rotational speed of the disc, 1500 gray-scale images were acquired and recorded to a desktop computer. A modified version of an algorithm (Ait Abderrahmane 2008) implemented on MATLAB environment using image processing (toolbox) technique was used for automatic processing of the acquired images and outputting the pattern's frequency. A typical 8-bit gray-scale image acquired by the CMOS camera is shown in figure 4(a). As shown, the usage of the dark soluble liquid dye and the bright disc background are of great benefit in enhancing the contrast and clearness of the line of intersection between the disc's bright surface and the dark rotating liquid.

The first step in the used algorithm was image segmentation, which is converting the 8-bit gray-scale images to binary (black and white) using a certain threshold value to differentiate between the bright and dark portions of the image, being the disc surface and rotating liquid, respectively. Finding the best threshold value for such conversion is very important and

sensitive. A reasonable initial trial for the threshold value for a certain image segmentation process, is selecting a threshold value somewhere between the two grouped accumulations of pixels along the gray-scale bins of an image histogram. Although using a constant threshold value in image segmentation for a set of images with uniform gray-scale intensities is reasonably accurate, there was a difference in frequencies between the camera shutter speed and the fluorescent neon light intensity, back to back images had different brightness and therefore different gray-scale histograms. Consequently, a histogram matching technique (Gonzales et al. 2004) was implemented which was simply choosing a reference image (in this case, one of the brightest images) and copying its gray-scale histogram to other subsequent images (in this case, images of the same set) and therefore, applying a constant threshold value for their binary conversion (used in the original reference image). Figures 3(a) and (b) show a dark image and its corresponding histogram before and after the histogram copying technique is applied, respectively.



(a)



(b)

**Figure 3** (a) Dark image and its corresponding histogram; and (b) Same image and its corresponding histogram after the histogram copying technique was applied.

As shown in the above figures, the distribution of the image pixels were extended over larger range of the 8-bit gray-scale 255 bins when the copying technique was implemented. By moving the two groups of gray-scale pixels further apart from each other, the thresholding process became much easier and a constant threshold value could be applied for all images of the same set, therefore, confirming constant segmentation quality for all images of the same set.

Figure 4(b) shows the thresholded (binary) format of the initial gray-scale image (figure 4a) after applying the threshold. Pixels of the image with gray-scale values equal to or below the specified threshold value were assigned 0's (black pixels), on the other hand, pixels with gray-scale values above the threshold were assigned 1's (white pixels).

The second step was to extract the boundary edge of the region of interest. Since the intersection of the black region and the white region outlines the boundary of the hollow

polygonal patterns, an edge detection function was applied. The extracted boundary (figure 4(c)) of the binary image was filtered using a zero-phase filtering function, to avoid any phase distortion of the extracted set of contours, before they were proceeded to the next step. To check the accuracy of the extracted boundary contours, a random set of images for each run were selected and superimposed on their corresponding original gray-scale format images as shown in figure 4(d).

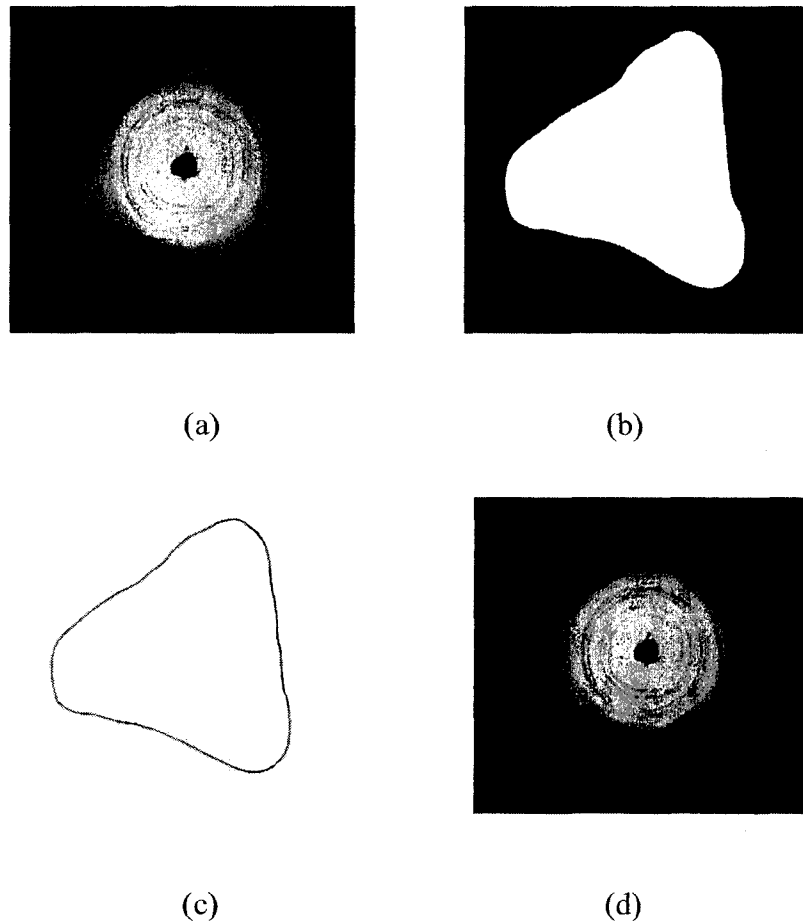


**Figure 4 (a) Original 8-bit gray-scale image acquired by camera; (b) Binary format (thresholded); (c) Extracted pattern boundary; and (d) Superposition of the extracted boundary on original image.**

It is clearly visible from the image that the extraction technique was of great accuracy

and reliability. To approximately quantify the accuracy of the algorithm, the set of sampled images were visually inspected using a pixel measuring tool in MATLAB. The average difference between the detected boundary contour and the original region of interest was found to be 6 pixels or 2%, measured from the centre of rotation of the disc. The maximum recognized error was 4.5% in less than 20% of the sampled images. The next step was extracting the radial displacement between the centroid of the extracted region and its edge, for all angular orientations (i.e.  $\theta = 0^\circ$  to  $360^\circ$ ). The MATLAB built in function that develops such extraction is known as signature function. The signature function was applied for the whole sequence of 1500 images for each run and a time series of the displacements was developed for each run at each angular orientation (360 time series). Figure 5 shows the corresponding signature plot of the sampled contour in figure 4(c).

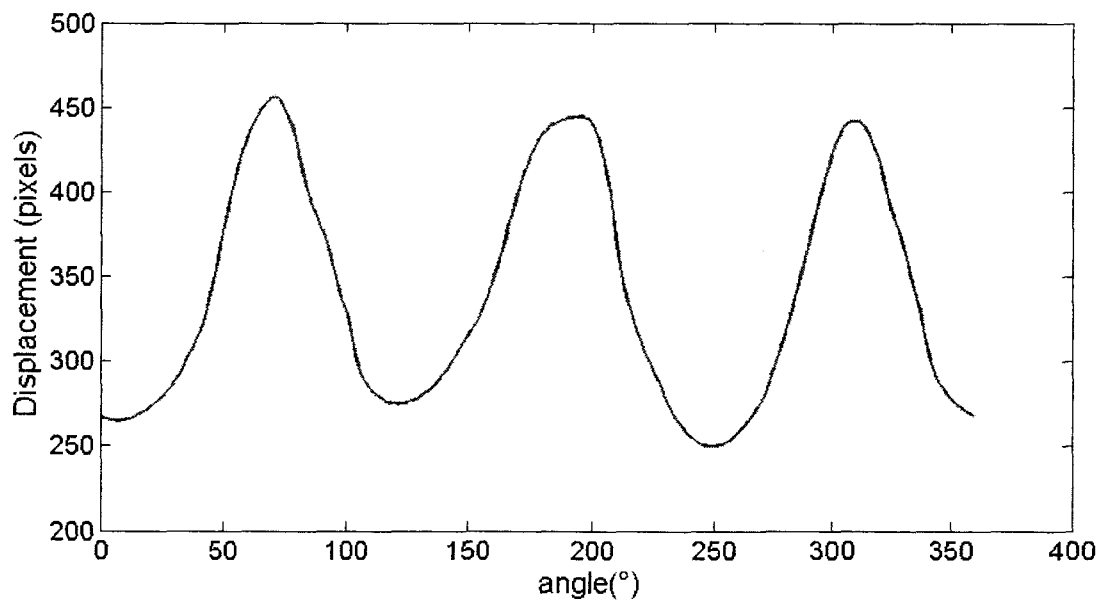


**Figure 5** Signature of the extracted boundary.

The extraction starts from  $0^\circ$  degree in the right horizontal direction and proceeds, in the

counter clock wise direction, all the way till 360 degrees (back to the initial point of extraction). The final step in computing the pattern's rotating speed was using the Fast Fourier Transform built-in function which transforms the developed time series data from the time domain to the frequency domain. Figure 6 shows a 10 seconds sample from the extracted time series.

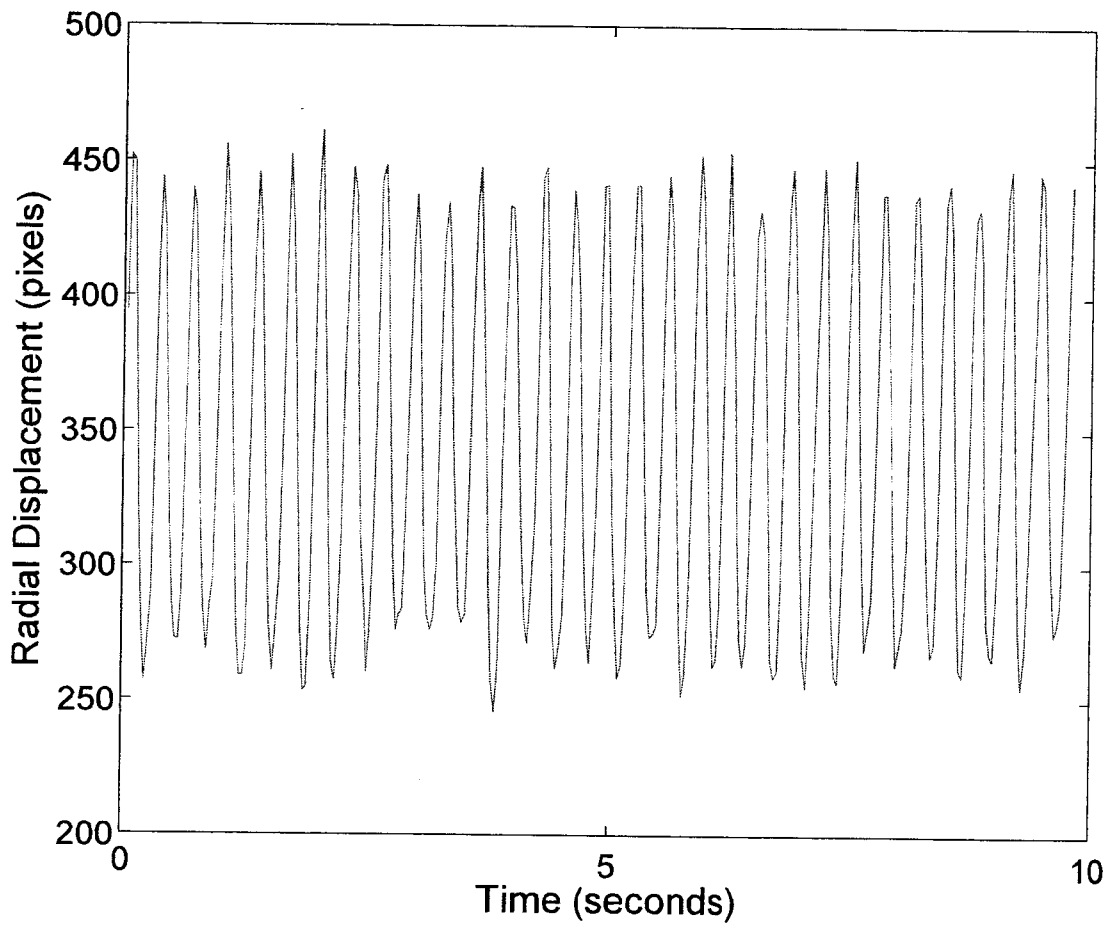


**Figure 6** Radial displacement time series at 10° angular orientation.

The frequency spectra from all 360 time series were then averaged and plotted against the signal power which corresponded to the square of the absolute radial displacements extracted in

the previous step. A typical power spectrum at a certain height and disc speed is shown below in figure 7.

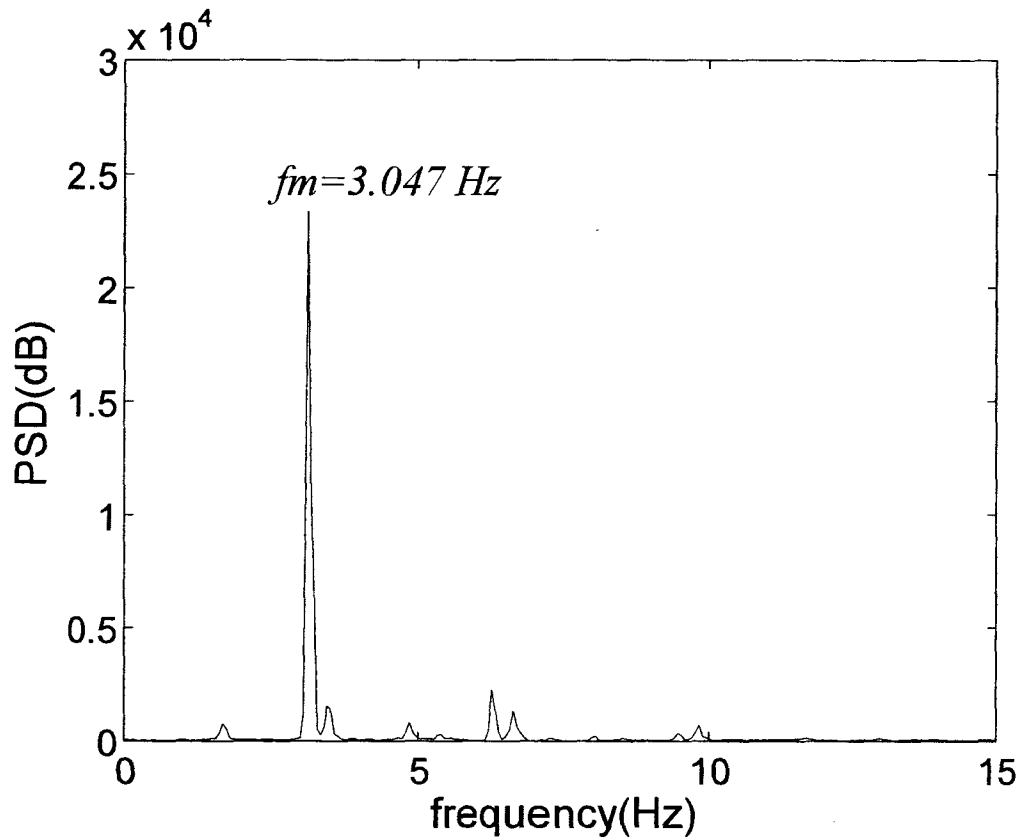


**Figure 7** Power spectrum of the processed set of images.

As shown in figure 7, the strongest peak along the frequency span corresponded to the pattern's apexes (corners) frequency (with longest radial displacement). Knowing the number of apexes ( $N$ ) or corners of the polygonal pattern for the computed time series, therefore the most powerful frequency  $f_m$  is related to the actual pattern's frequency  $f_p$  by  $f_p = f_m / N$ . In this example, knowing the number of apexes, being  $N=3$ , and since the most dominant peak occurred at  $f_m = 3.047$  Hz, therefore, the actual pattern's rotational speed using the above mentioned relation is



$f_p = f_m / N = 3.047 / 3 = 1.016$  Hz. Before applying the same procedure on all acquired sets of images, a sampling test has been done to verify the minimum number of images required for computing the power spectrum using the FFT technique. The minimum number of images required for the dominant frequency to be clearly visible and of relatively strong power, as compared to the associated noises, is 750. Therefore, doubling the sampling frequency was sufficient enough for obtaining reliable and accurate computations. After verifying the complete algorithm, all mode shapes rotational speeds were computed in the same manner. Figure 8 shows a flowchart of the algorithm used.

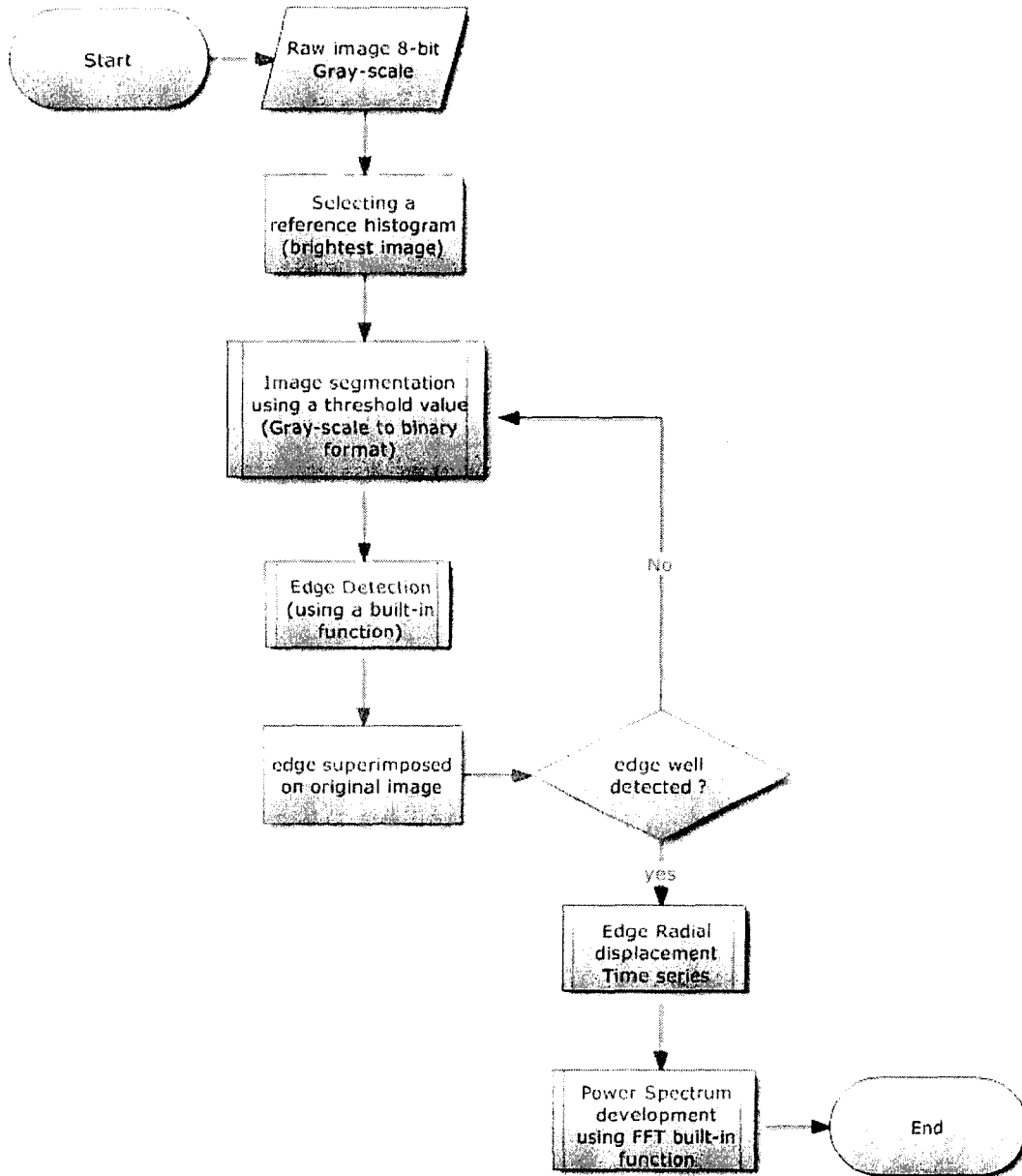


Figure 8 MATLAB algorithm flowchart.

### **2.2.2 Disc's speed measurement and control**

The motor speed, therefore the disc's speed, was controlled using a PID controller loop implemented on LABVIEW environment (see figure 9). By adjusting the controller inputs (P, I and D components), the controller then helps minimizing the induced error, between the desired and real time speeds, and therefore, ensures constant speed rotation of the disc. In order to measure the actual instant rotating speed of the disc, a reflecting photo sensor was placed facing the flywheel edge which is part of the rotating shaft. Twenty-four reflecting strips, 5 mm in width, were evenly distributed along the flywheel's circumference. The photo sensor acquired the reflecting light signals and transferred them to the desktop computer, via a data acquisition board, where the actual RPM of the flywheel (disc) is first calculated and then proceeded to the PID controller loop as a feedback input. The controller consisted of four main components, a Brush Type Pulse Width-Modulation Servo Amplifier (Advanced Motion Controls), an external power source (Philips), a data acquisition board (National Instruments) and a desktop computer. The PWM servo amplifier is used to assist controlling the speed of the motor. With a fast on/off switching feature, the PWM servo made the voltage passing to the DC Motor to be the average value of the voltage over time. The PWM servo amplifier is powered by an external 10V power source and the analog output of the servo amplifier is passed to the motor. The photo sensor measures the real time speed and feedback to the desktop computer through the data acquisition board. The PID controller loop measures the error between the set point (desired by operator) and the real time velocities and the new voltage value signal is passed back to the servo amplifier through the data acquisition board to complete the controller circuit.

Different combinations of P, I and D values were performed until an acceptable design

was confirmed based on the required accuracy and precision of the conducted experiments. The controller had an average error of 0.3%. In addition to constant speeds input, the controller allowed different desired input signals to be performed such as rotation in both directions signals, ramp input signal, sinusoidal input signal and many others.

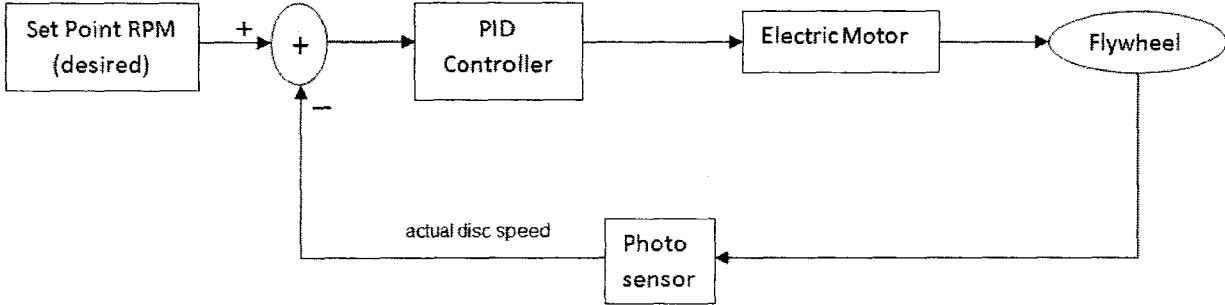


**Figure 9** Disc's speed controller loop.

## Chapter 3

### The effect of liquid viscosity on polygonal instability behaviour

#### 3.1 Effects of flow parameters on polygonal pattern instability

Various studies on free surface swirling flows within cylindrical containers have revealed many parameters that affect the flow behaviour in many different ways and to different extents. These parameters include: disc rotating speed, disc diameter, liquid initial height, working fluid properties, boundary conditions as well as initial conditions and the spin up or spin down rate (time history). In this chapter, the effects of all mentioned control parameters are summarized and the effect of the working fluid kinematic viscosity on the flow behaviour will be studied extensively. Increasing the working fluid initial height was observed not only shifting a certain pattern's limits of endurance towards higher disc frequency ranges, but also influencing the existence of polygonal patterns (Vatistas 1990). In our studied experiments, for small initial heights ( $h_i = 20$  mm),  $N=3$  to  $N=6$  patterns were observed, losing the lowest mode shape ( $N=2$ ). As the height started increasing, the oval pattern ( $N=2$ ) was recognized but higher mode shapes disappeared. For example, at  $h_i = 30$  mm, polygonal patterns  $N=2$  till  $N=5$  were observed and for  $h_i = 40$  mm,  $N=2$  till  $N=4$  were the only observed. In this thesis, experiments were done using water at even higher initial heights (up to  $h_i = 120$  mm). Patterns  $N=2$  and  $N=3$  were the only observed and persisted for longer ranges of disc's speed as the height increased, which confirms the observations of Jansson et al. (2006) using water in a similar set-up. Not only the liquid initial height, but also the rotating disc diameter had influence on the patterns formation and limits of endurance (Vatistas 1990). As the disc's diameter increases, the ranges of disc's speed where certain patterns existed are shifted towards lower disc frequency values (existed earlier)

and lasted longer segments of disc's speeds. The initial liquid height and disc diameter were considered together as a general control parameter in the form of aspect ratio ( $AR=h_i/R$ ) in many related studies. In barotropic flows, discussed in chapter 1, where concentric cylinders were co-rotating with relative velocities, varying the aspect ratio had huge influence on shear layer instabilities formation and evolution (Chomaz et al. 1988). At low  $AR$ 's, high number of shear layer instability vortices existed which is consistent with interfacial instability phenomenon observed in the set-up configuration discussed here. The number of vortices recognized in the phenomenon under investigation increased when either the initial height was decreased or the disc's radius was increased (Vatistas 1990).

Attempts of generating swirling flows in different geometrical containers partially filled with liquid, therefore varying the boundary conditions, have been studied and revealed different flow behaviour than the ones observed in cylindrical containers (Duck et al. 2001). Not only the container structure but also the states of the end and side walls have great influence on the swirling flow dynamics. Experiments with swirling flows driven by rotating one of the endwalls and/or sidewalls have been studied and the effect of the existence of top endwall on the flow behaviour has been observed to reveal different flow behaviours and responses (Spohn et al. 1993). An extensive study on the spin up/down rates in fully filled axisymmetric flows can also be found in (Duck et al. 2001). Vatistas (1990) found that the rate of spin up/down of partially filled swirling flows has huge influence on the polygonal patterns appearance associated with slight hysteresis. This effect was confirmed in the current study, i.e., the higher the jumps in spin up/down, the earlier the polygonal patterns appearance and therefore the transition processes taking place. The surface tension effects have been considered in Jansson et al. (2006). By

introducing a surfactant into a swirling flow partially filled with water, they found that the dependence of the polygonal instability phenomenon on the surface tension is almost negligible.

### **3.2 The influence of viscosity on polygonal patterns formation and limits of endurance**

Liquids with higher viscosity were found to resemble to great extend similar flow behaviour as of water, being the working fluid, but influencing the patterns formation. Jansson et al. (2006) found no more than  $N=3$  polygonal instabilities, using similar set-up and parameters condition as of water, but using ethylene glycol as the working fluid (15 times the viscosity of water). In this study, a more systematic study on the kinematic viscosity effects on instability patterns formation and limits of endurance has been done. Eight different aqueous glycerol mixtures were used in the experiments with viscosities varying from 1 up to 22 (0 ~ 75% glycerol) times the water's at room temperature (21°C). The detailed points of study were: 1, 2, 4, 6, 8, 11, 15 and 22 times the water's dynamic viscosity ( $\mu_{\text{water}}$ ) at room temperature. Although the viscosity of the mixture varied exponentially with the glycerol concentration (figure 10), closer points of study were conducted at low concentration ratios since significant effects have been recognized by just doubling the viscosity of water as it will be discussed below. The temperature of the working fluid was measured and recorded before and just after a typical experimental run and was found to be stable and constant (room temperature), therefore, the viscosity of the mixture was ensured to be constant and stable with time. Phase diagrams have been conducted and showed great approximation in defining the different phase regions for existing patterns in terms of disc's speed and initial height within the studied viscosity range.

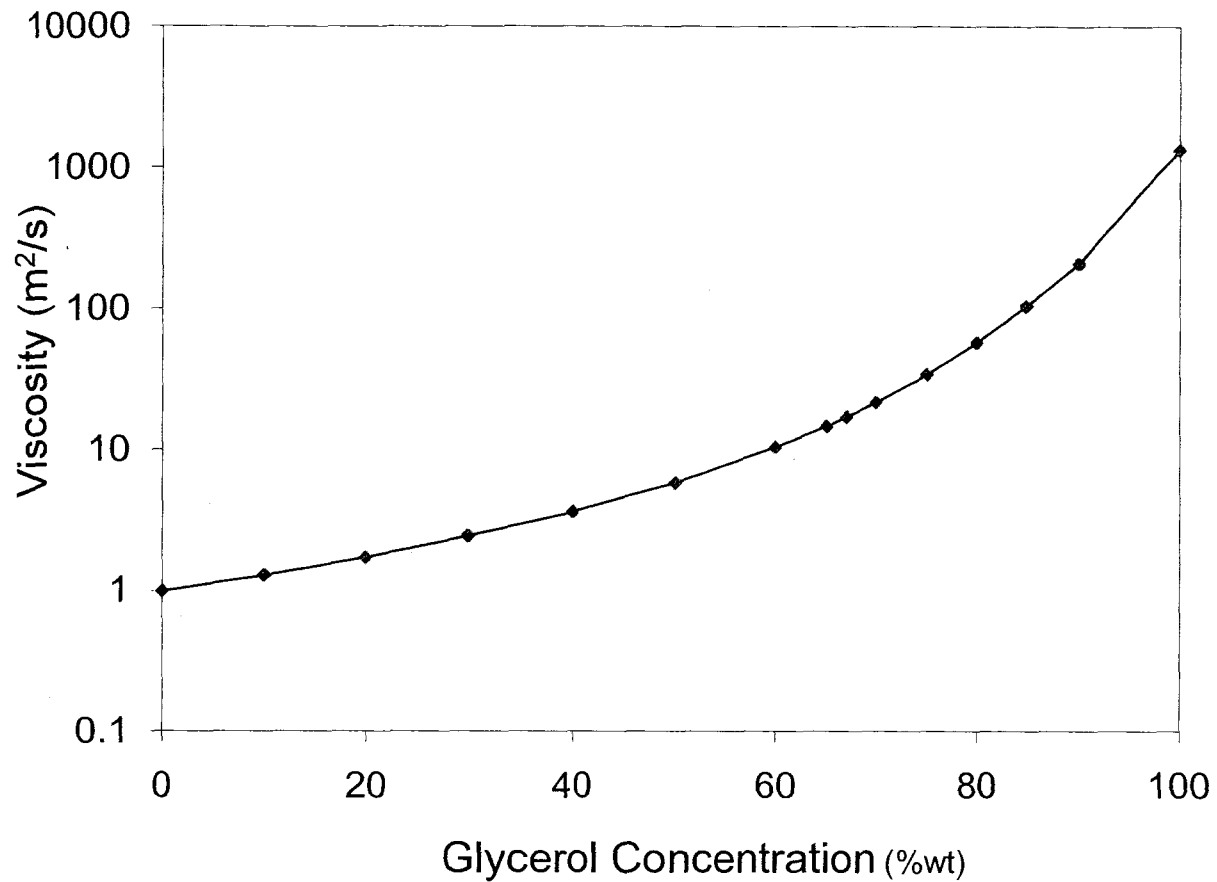


**Figure 10** Kinematic viscosity vs. glycerol concentration.

### 3.2.1 Initial height $h_i = 20$ mm

Figure 11 shows the phase diagram at the lowest initial height in this study ( $h_i = 20$  mm) where all 5 polygonal patterns are recognized using the current apparatus. This figure starts with water as the working fluid where the expected patterns were observed, being Triangle ( $N=3$ ), Square ( $N=4$ ), Pentagon ( $N=5$ ) and Hexagon ( $N=6$ ). By gradually mixing glycerol with water, therefore increasing the mixture kinematic viscosity, the limits of endurance of all four mode shapes decreased significantly until the highest mode shape ( $N=6$ ) disappeared at viscosity equal to 2 times that of water, leaving only  $N=5$ ,  $N=4$  and  $N=3$  patterns. When the viscosity reached 4



$\times \mu_{\text{water}}$ , both square and pentagon patterns were not observed. Triangular pattern was the only persisting equilibrium state but eventually, it was even destroyed as viscosity reached  $8 \times \mu_{\text{water}}$ , leaving no polygonal patterns for the rest of the studied viscosity domain. An interesting observation from the first phase diagram plot is the fact that, it could have been reasonably presumed that increasing the viscosity would dominate the shear forces within the entire flow, therefore expecting early arrivals of polygonal patterns in terms of the disc rotating speed. Such prediction is clearly confirmed in figure 11. As the viscosity increased, all patterns occurred earlier until they eventually vanished.

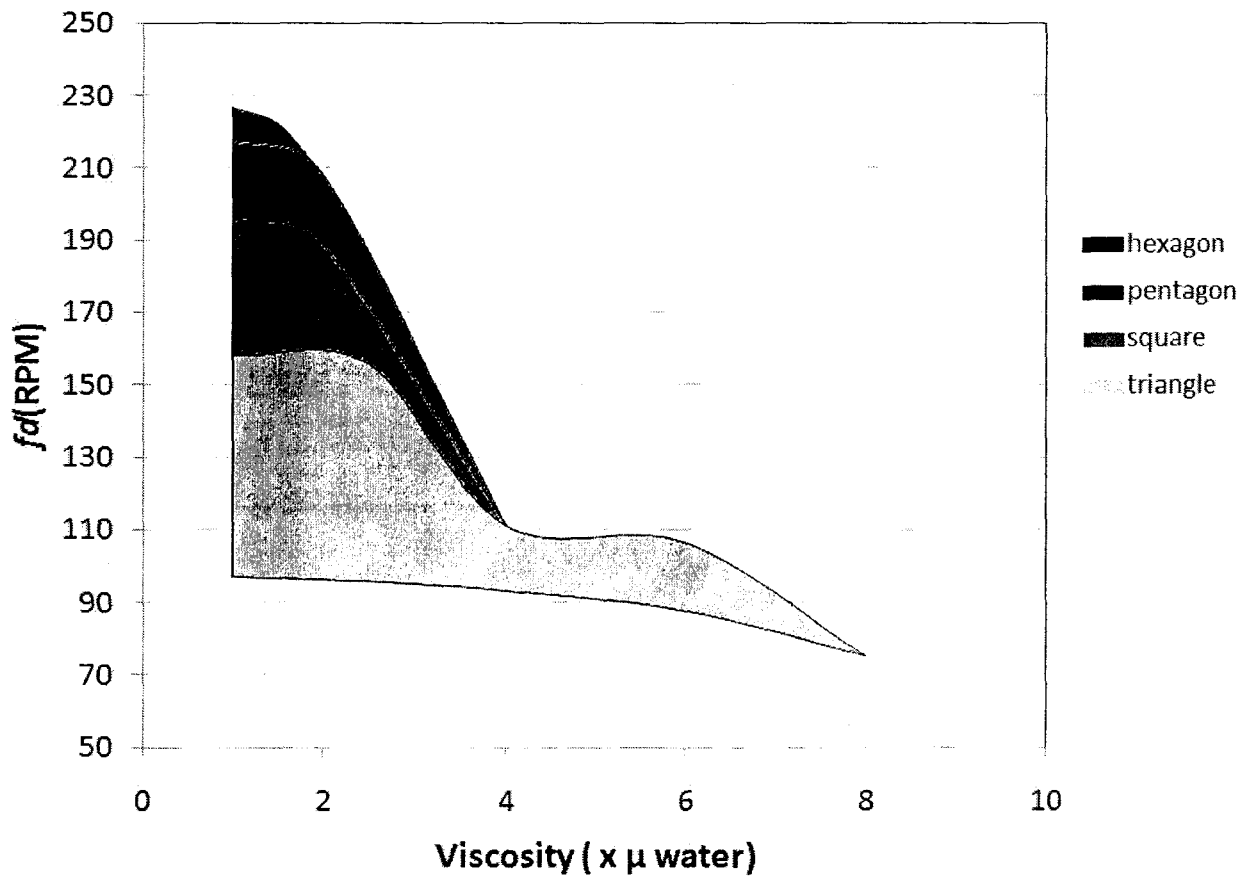


**Figure 11** Phase diagram for polygonal patterns observed through the viscosity domain at  $h_i = 20$  mm.

### 3.2.2 Initial height $h_i = 30$ mm

Moving to the intermediate initial height ( $h_i = 30$  mm) in this study, the phase diagram (figure 12) followed almost the same behaviour as in lower initial height. Using water ( $1 \times \mu_{\text{water}}$ ), oval, triangle, square and pentagon patterns were observed as explained earlier. As the working fluid viscosity increased, pentagon pattern first disappeared at double the water's viscosity followed by the square pattern at  $8 \times \mu_{\text{water}}$ . Surprisingly, the oval pattern also disappeared when viscosity reached  $8 \times \mu_{\text{water}}$ , leaving the triangular pattern as the only recognized pattern. At the highest aqueous glycerol mixture concentration ( $22 \times \mu_{\text{water}}$ ), no patterns were recognized. Therefore, it is expected that the triangular pattern is fully destroyed somewhere between the studied concentration points (65% and 75% glycerol or  $15$  and  $22 \times \mu_{\text{water}}$ ). It is worth mentioning that the polygonal patterns followed the same trend by appearing at lower disc speed range until the triangular pattern became the only recognized instability where it followed a different trend and persisted for high RPM range. At high viscosity values, unstable, non-defined hollow vortex cores were observed until the triangle ( $N=3$ ) pattern was formed.

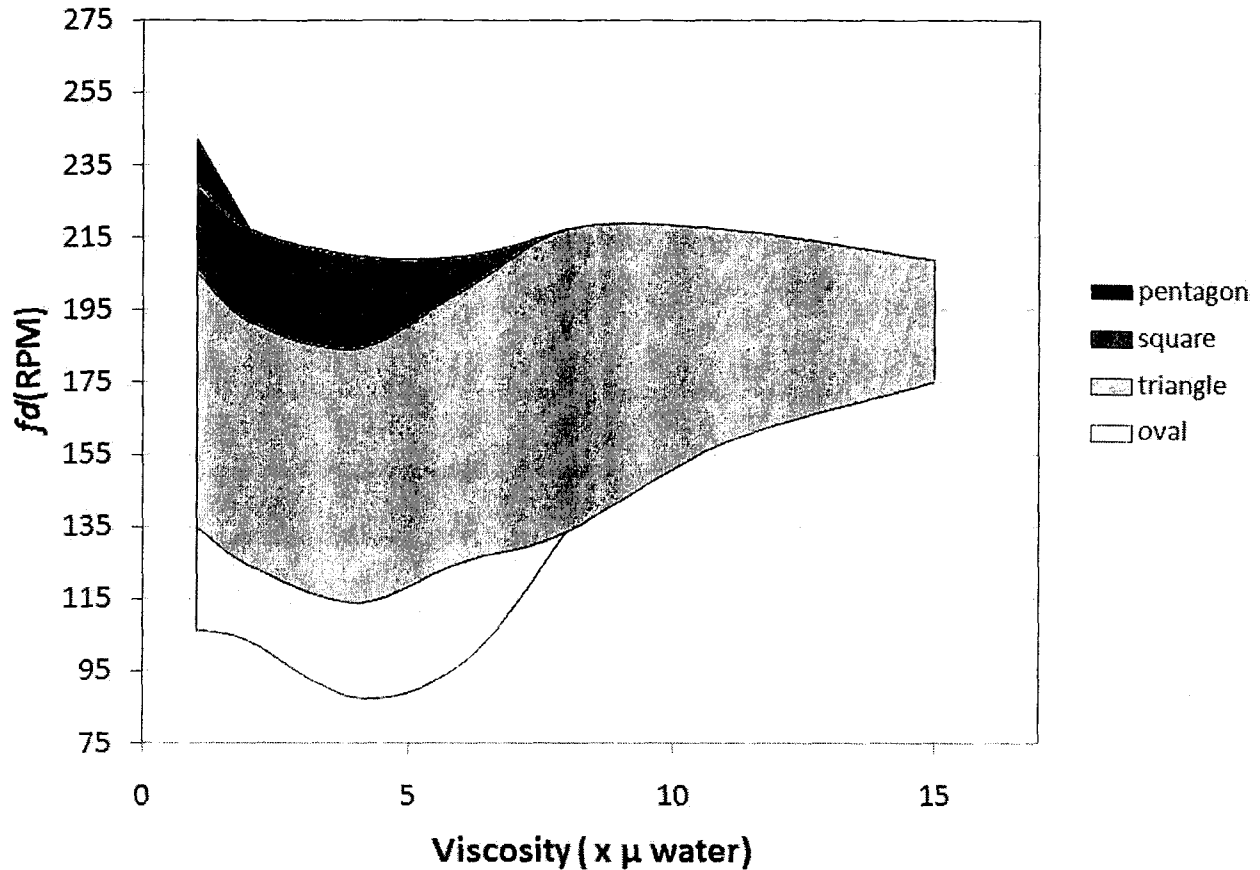


**Figure 12** Phase diagram for polygonal patterns observed through the viscosity domain at  $h_i = 30$  mm.

### 3.2.3 Initial height $h_i = 40$ mm

At  $h_i = 40$  mm (figure 13), oval ( $N=2$ ), triangle ( $N=3$ ) and square ( $N=4$ ) polygonal patterns were the only experienced ones using water as the working fluid. Gradually increasing viscosity of the fluid by adding glycerol, all three mode shapes' limits of endurance decreased significantly until the highest mode shape ( $N=4$ ) disappeared at viscosity equal  $6 \times \mu_{\text{water}}$ , leaving only  $N=3$  and  $N=2$  patterns as the only persisting patterns for the rest of the studied viscosity domain. It is expected that the flow will follow the same behaviour as in lower heights which means losing both patterns eventually if the viscosity is increased beyond the studied region. The

general trend of the early appearance of polygonal patterns was also observed at this initial height.

It is clearly observed from all performed experiments that the triangular pattern is the most persisting and stable pattern recognized and it is also associated with the oval pattern at high initial heights. A reasonable explanation for such observation might be the fact that as the polygonal patterns sides increase, the apexes (corners) become less sharp. Moreover, increasing the liquid's viscosity has direct proportionality with the shear forces which in incompressible flows governed by Navier-Stokes Equation gives rise to the deviatoric stress tensor of the flow which helps flattening pattern's boundary, therefore, distorting its well defined geometry and sharp apexes (G.K. Batchelor 2000). These two facts make it clearer why higher mode shapes are the first to disappear as the fluid's viscosity was increased gradually. Figure 14, shows oval and triangular patterns observed at same speeds and initial heights but different liquid viscosities (1, 8,  $22 \times \mu_{\text{water}}$ ). It can be easily recognized that the patterns boundary became distorted and the sharp corners of the polygonal patterns diverged and became much flattened, consequently as the viscosity increased.

So far, the liquid's viscosity was found to have the tendency of initiating the polygonal instability patterns at earlier disc's speeds, at the same time, it worked as a destructive parameter for the interfacial symmetry breaking phenomenon observed within the hollow vortex core. Both conclusions are consistent with experiments done by Jansson et al. (2006) using ethylene glycol at equivalent aspect ratios.

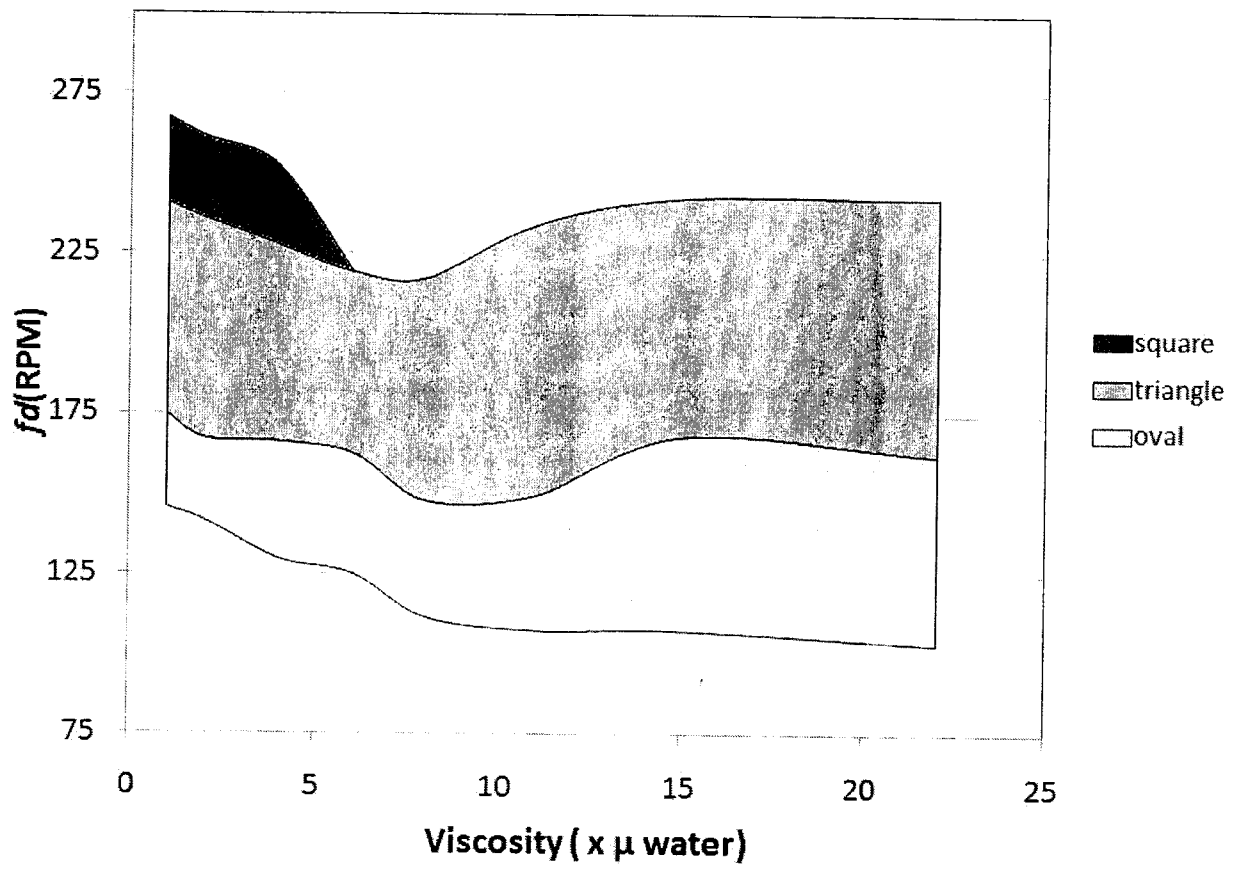
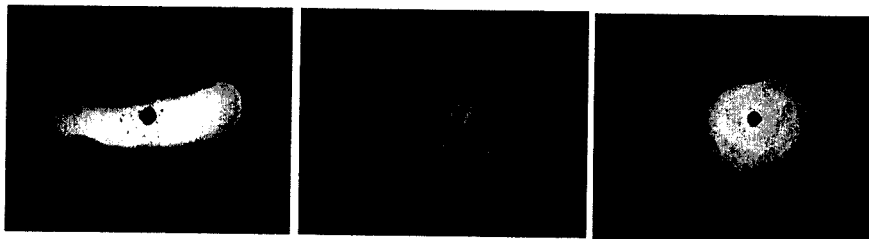
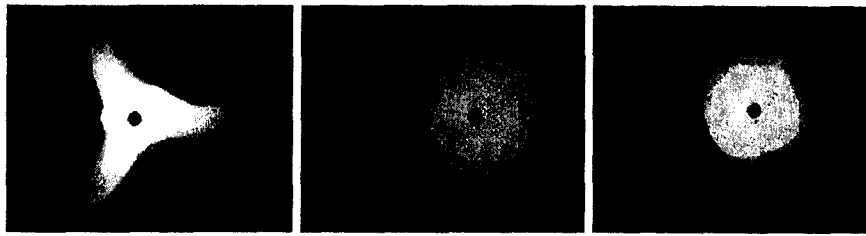


Figure 13 Phase diagram for polygonal patterns observed through the viscosity domain at  $h_i = 40$  mm.



(a)



(b)

**Figure 14** a) Oval pattern at constant parameters condition but three different viscosities; and (b) Triangular pattern at constant parameters condition but three different viscosities.

### 3.3 Density influence on patterns formation

Although, the effects of varying the kinematic viscosity of the working fluid on the polygonal patterns formation and limits of endurance have been studied, it is important to realize that mixing glycerol with tap water would indeed result in varying two individual parameters conditions at the same time, namely, the dynamic viscosity and specific gravity of the fluid. Therefore, it is important to carry further experiments being able to vary just one parameter at a time to analyze their effects on the polygonal patterns instability solely. The maximum change in fluids specific gravity in our study was 1.18, when using 75% glycerol in the aqueous glycerol mixture, at room temperature. Using brine (salt saturated water) was sufficient enough to slightly vary the specific gravity of the fluid, without significantly changing any other fluid's characteristics consequently, therefore, accounting for the slight change of density when the water/glycerol mixture was used. Saturating water with salt at room temperature resulted in a specific gravity of 1.254. Brine was used as the working fluid in three experimental runs at the three different heights under investigation. Brine was found to act in almost a similar behaviour as water. Varying the specific gravity of the working fluid has slightly influenced the pattern

formation and limits of endurance. The main observation was the fact that, increasing the specific gravity of the working fluid has slightly increased the limits of endurance of high mode shapes for all initial fluid heights (see figure 15); making them last longer ranges of disc's rotational speeds ( $f_d$ ). No other significant changes did occur when slightly increasing the working fluid's density by almost 25.4%.

Therefore, one can confidently consider the slight change in the working fluid's specific gravity, when using a mixture of glycerol and water, is of almost no effect as compared to the great influence associated with varying the viscosity of the fluid.

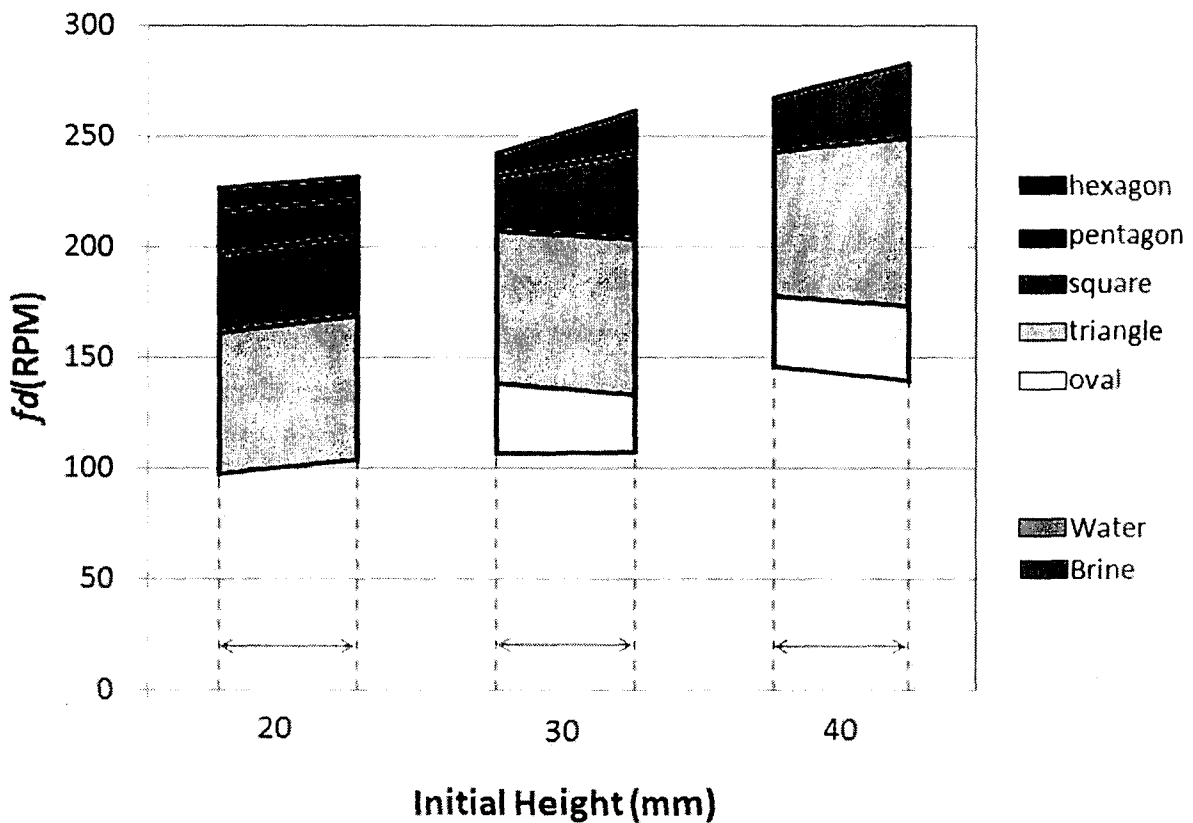
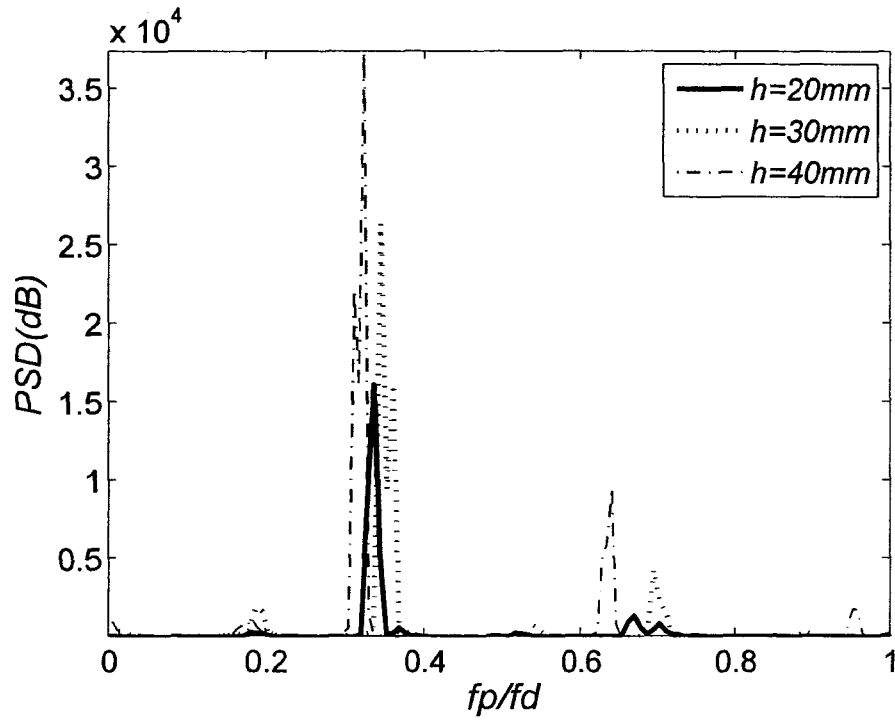


**Figure 15** Phase diagram for three different heights using water and brine as the working fluids.

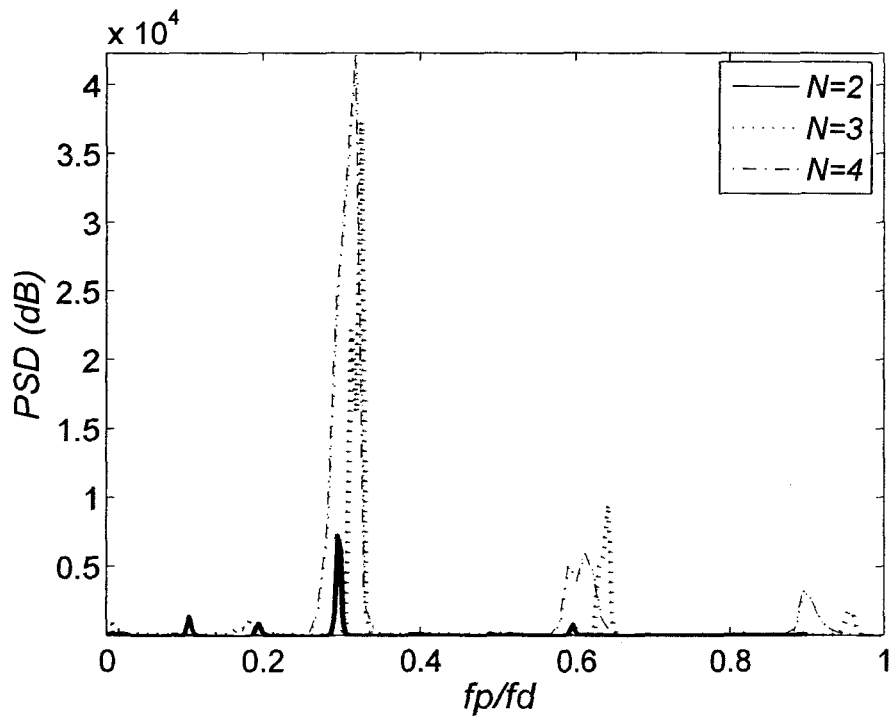
### 3.4 Polygonal pattern's frequency variation

In order to provide further quantification of the phenomenon, more detailed analysis on the experimental results obtained at the three different initial liquid heights (20, 30, 40 mm) with the 8 different liquid mixtures stated earlier are now discussed. Automatic processing of the images was executed using the MATLAB algorithm explained in Chapter 2 and the pattern's speed was computed for each set of images. Jansson et al. (2006) using similar set-up have observably quantified the polygonal pattern to rotating disc's frequencies with a mode-locking ratio of  $1/N$  for all corresponding polygonal  $N$ -sided patterns except for the oval pattern where the ratio was  $2/3$ . Vatistas et al. (2008) using water as the working fluid have found that the stable pattern's frequency to disc's speed ratio is approximately constant and equal to  $1/3$  irrespective of the mode shapes or the water initial height. The observation of Vatistas et al. (2008) has been confirmed for the three different heights studied in this thesis using similar measuring technique. Figure 16(a) shows a superposition of the triangular pattern power spectra at three different initial heights using water as the working fluid. The strongest peaks coincided at a frequency ratio ( $f_p/f_d$ ) of approximately  $1/3$  as shown in the figure, with a maximum deviation of 0.03 Hz or 9%. Similar mode-locking ratio was also confirmed for all other mode shapes. Figure 16(b) shows the power spectra for all  $N$ -gons observed at initial height  $h_i = 40$  mm using water as working fluid.





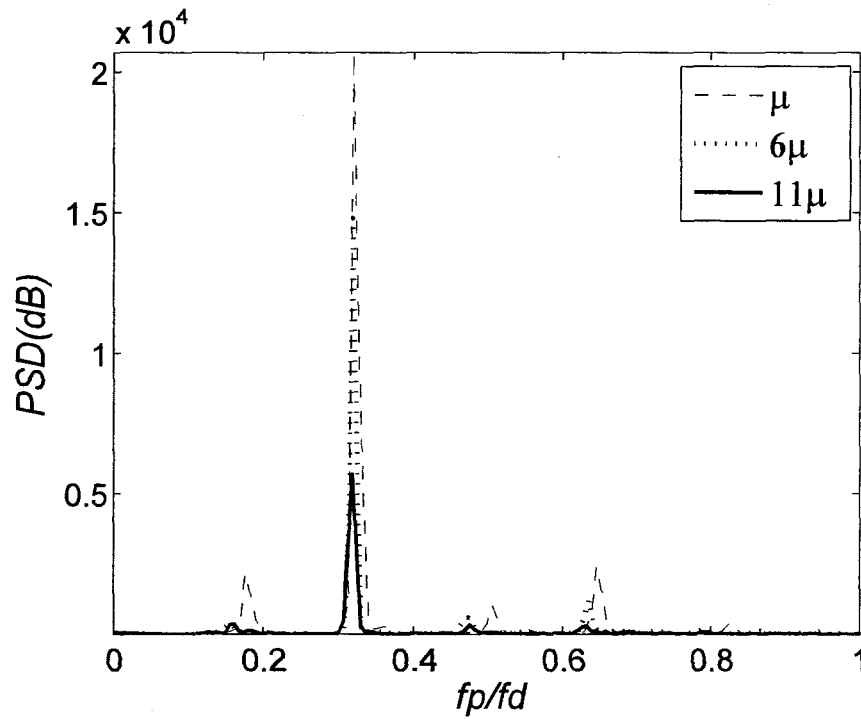
(a)



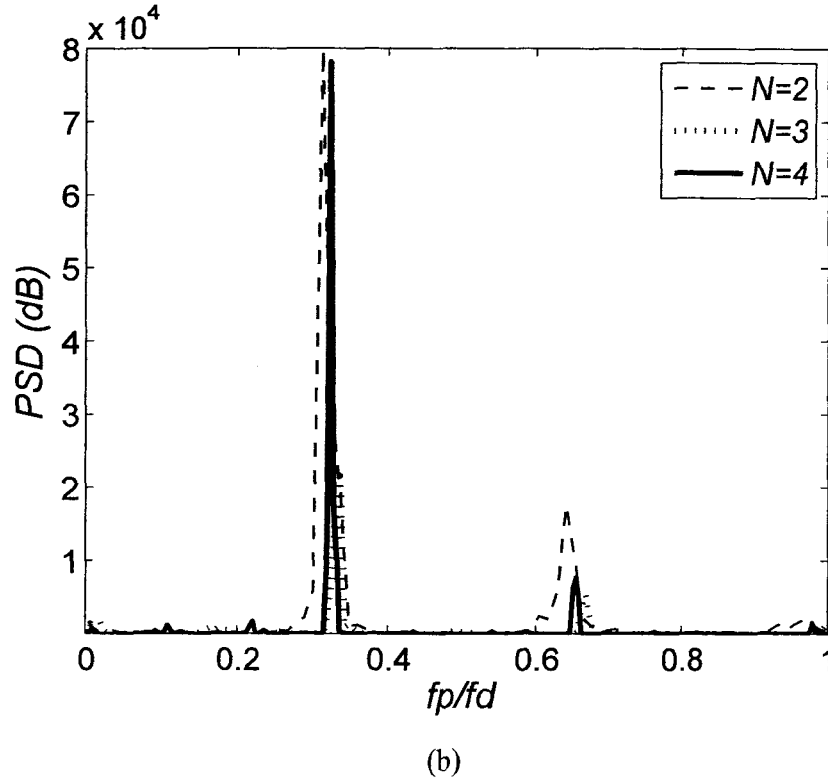
(b)

**Figure 16** (a) Power spectra superposition for triangular pattern at three different heights; and (b) Power spectra superposition for all mode shapes at  $h_i = 40$  mm.

Various viscous mixtures were also found to satisfy the same mode-locking frequency ratio with 6% average deviation. Figure 17(a) shows a superposition of triangular pattern observed using fluids with three different viscosities ranging from one, six and eleven times the water's viscosity. It is clearly shown that the normalized pattern frequencies also overlapped at the same mode-locking ratio of approximately  $1/3$ . Figure 17(b) also shows the power spectra of all patterns recognized using aqueous glycerol mixture with four times the viscosity of water.



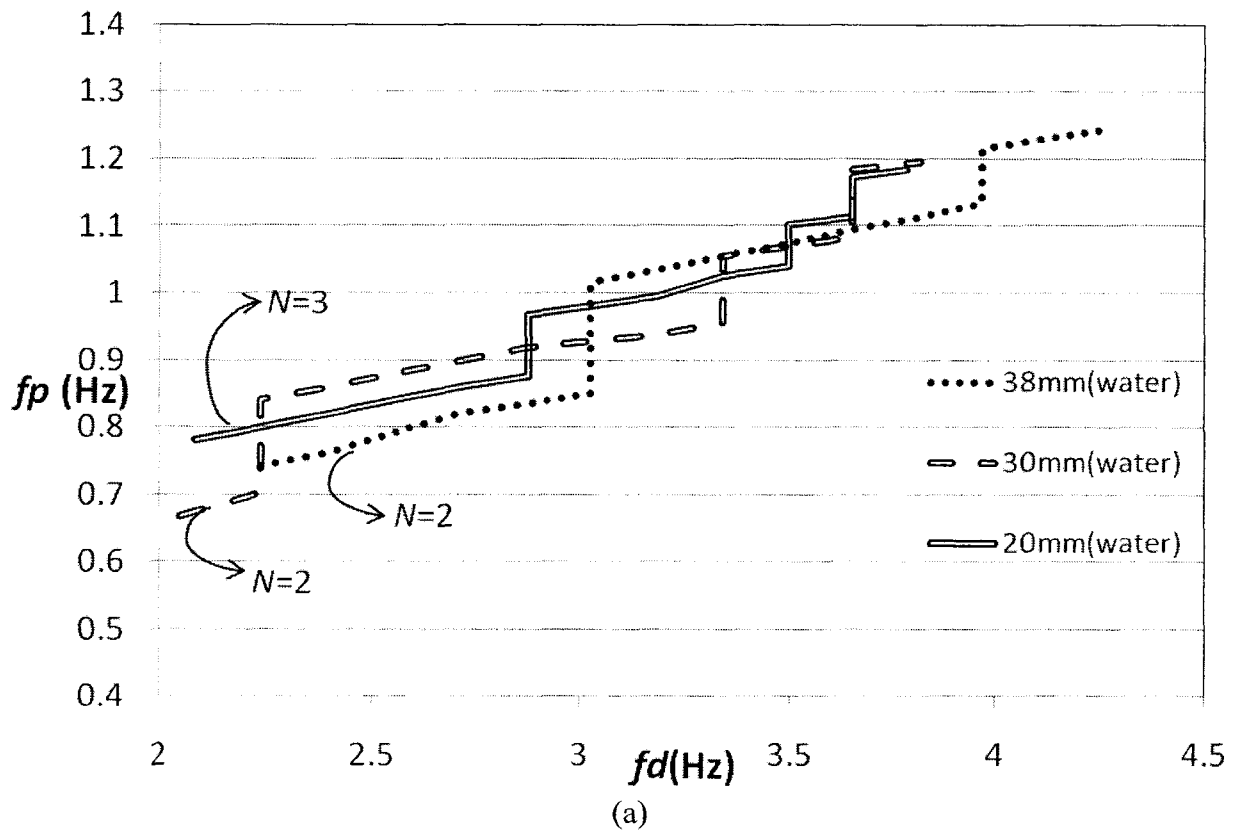
(a)

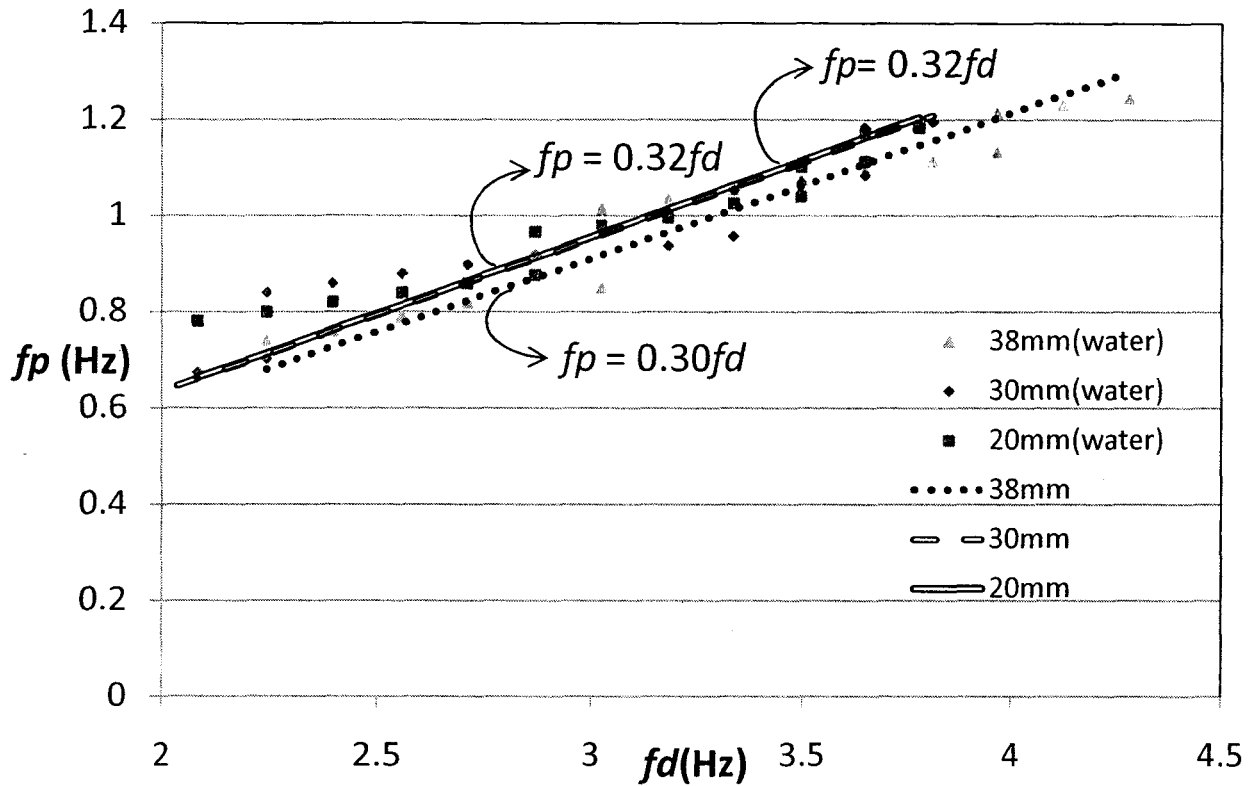


**Figure 17** (a) Power spectra superposition for triangular pattern using three different viscosity fluids; and (b) Power spectra superposition at  $h_i = 40$  mm for all mode shapes using a mixture with  $4 \times \mu_{\text{water}}$ .

All frequencies plotted above corresponded to stable patterns; i.e. steady-state polygonal patterns at the beginning of their range of existence. The speeds of the patterns increased linearly with the disc's rotational speed for all mode shapes. An abrupt jump in the pattern's frequency took place during transitional process from any mode  $N$  to a higher  $N+1$  mode shape. Figure 18(a) shows the relationship between the pattern's speed ( $f_p$ ) and the disc's frequency ( $f_d$ ) using water at three initial liquid heights. It is found that the pattern's speed for all heights increases linearly, with approximately constant slopes for all polygonal patterns, with the disc's speed. The sudden jumps in pattern's frequencies correspond to transition processes between two subsequent mode shapes (polygonal patterns). As it was discussed in the last section, for initial

water height of 20 mm, polygonal patterns  $N=3$  up till  $N=6$  were observed. As for  $h_i = 30$  mm, the observed polygonal patterns were  $N=2$  (oval) all the way up to  $N=5$  (pentagon). On the other hand, polygonal patterns  $N=2$ ,  $N=3$  and  $N=4$  are the only observed patterns at initial water height  $h_i = 40$  mm. Therefore, the first growing straight line corresponds to the triangular pattern for the lowest height and oval pattern for the other two heights. The vertical jump in the pattern's frequency corresponds to the transition to a subsequent higher mode shape, respectively. Linear fitted curves for the scattered relationship plot at all initial heights have been plotted (see figure 18(b)). The zero intercept slopes of the general propagation of the pattern's frequency during the entire phenomenon's disc frequency span confirm the mode-locking frequency ratio of approximately  $1/3$  found by Vastitas et al. (2008).

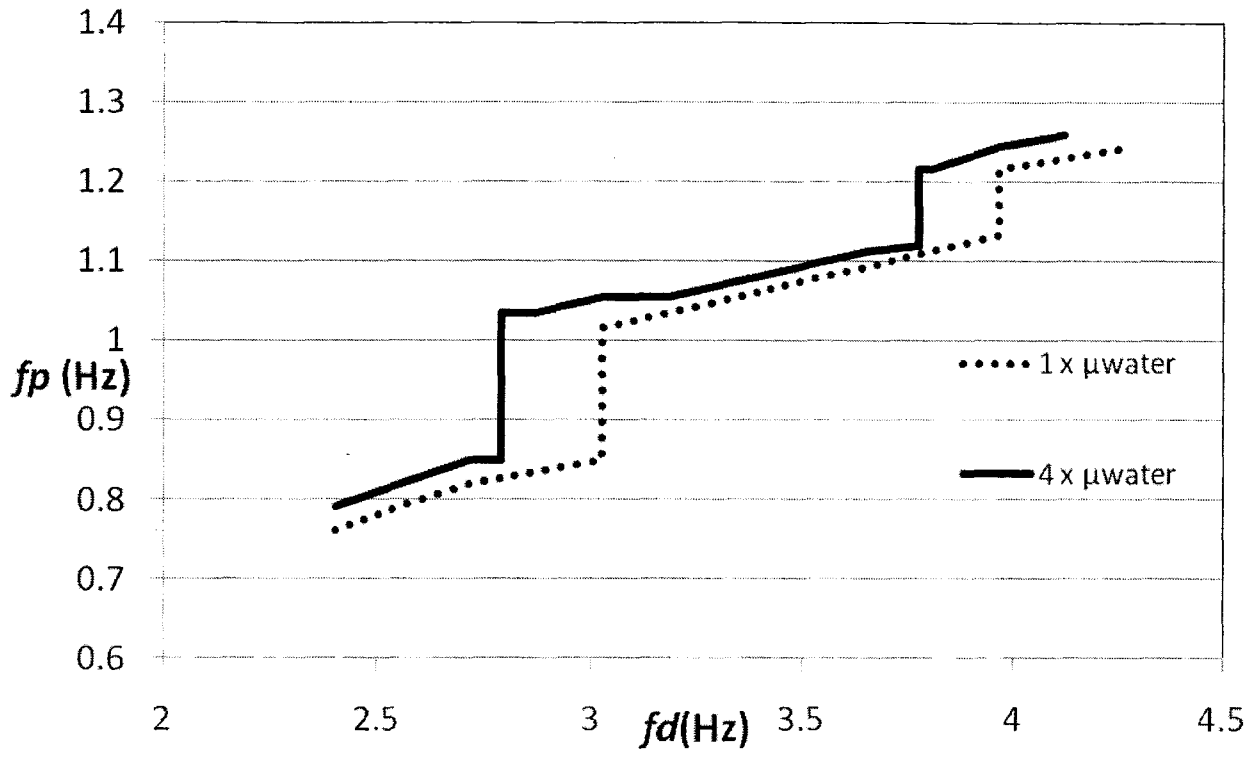




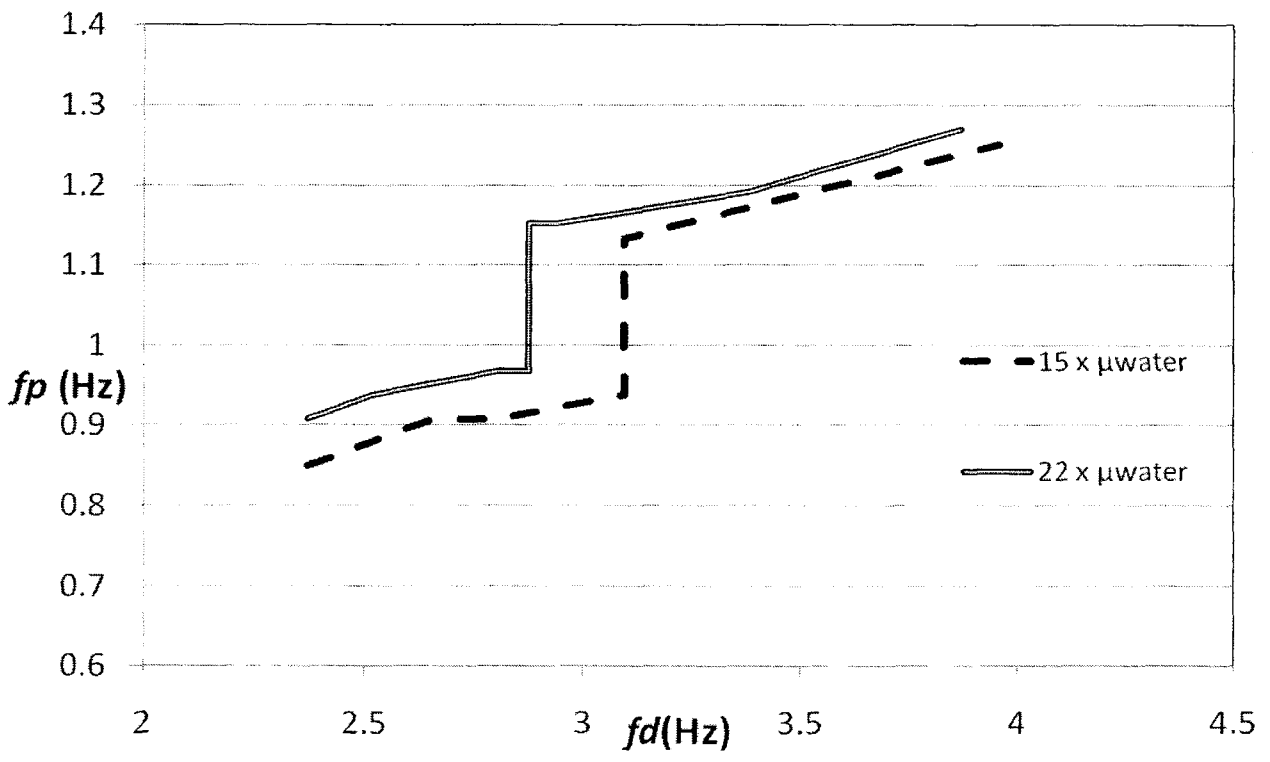
(b)

**Figure 18** (a) Pattern's frequency propagation with increasing disc's speed (b) Linear fitted slopes for frequency propagation.

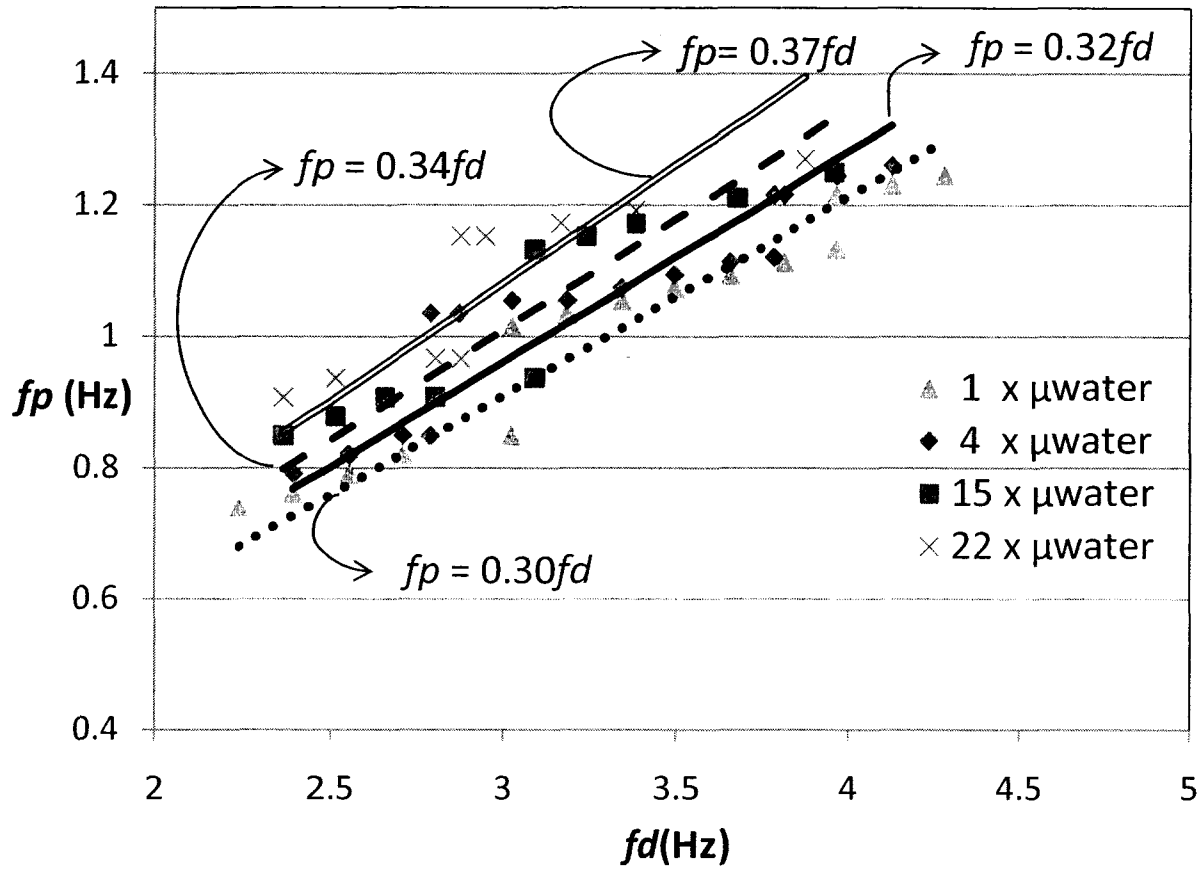
Similar relationship curves were developed for higher viscous working fluids. Figure 19(a) shows the relationship between both frequencies at same initial height of  $h_i = 40$  mm but using water and aqueous glycerol mixture with viscosity  $4 \times \mu_{\text{water}}$ . It appears obvious that higher viscous flow shows relatively faster rotating speeds ( $f_p$ ) through the entire disc frequency range ( $f_d$ ). Moreover, the earlier transition between all mode shapes is clearly visible here. Figure 19(b) shows another plot for the polygonal patterns frequency propagation using working fluids with higher viscosities of  $15$  and  $22 \times \mu_{\text{water}}$ , at the same initial height of  $h_i = 40$  mm.



(a)



(b)



(c)

**Figure 19** (a), (b) Pattern's frequency propagation with increasing disc's speed; and (c) Linear fitted slopes for frequency propagation at  $h_i = 40$  mm.

At these two viscosities, the oval and triangular patterns are the only observed patterns, the polygonal frequencies followed similar trend as the one observed at lower viscosities. The higher viscous fluid shows faster rotating speeds through the entire disc varied frequency range as well as the transition process which also moved toward lower disc speeds confirming the same behaviour.

Figure 19(c), plots the linear fitted straight lines for all four different viscosity working fluids with their corresponding line style. It is clearly shown that the rate of propagation of the polygonal pattern's rotational speed increased gradually with increasing liquids viscosity. A maximum increase of about 25% in the polygonal pattern's rotational frequency has been recorded between the maximum and the minimum viscosity values used in this study. Figure 20 shows also the linear fitted straight lines for the scattered polygonal pattern speed propagation with increasing disc speed at three different viscosities and initial liquid height of  $h_i = 20$  mm. The rate of polygonal patterns speed up increase gradually as the viscosity is increased.

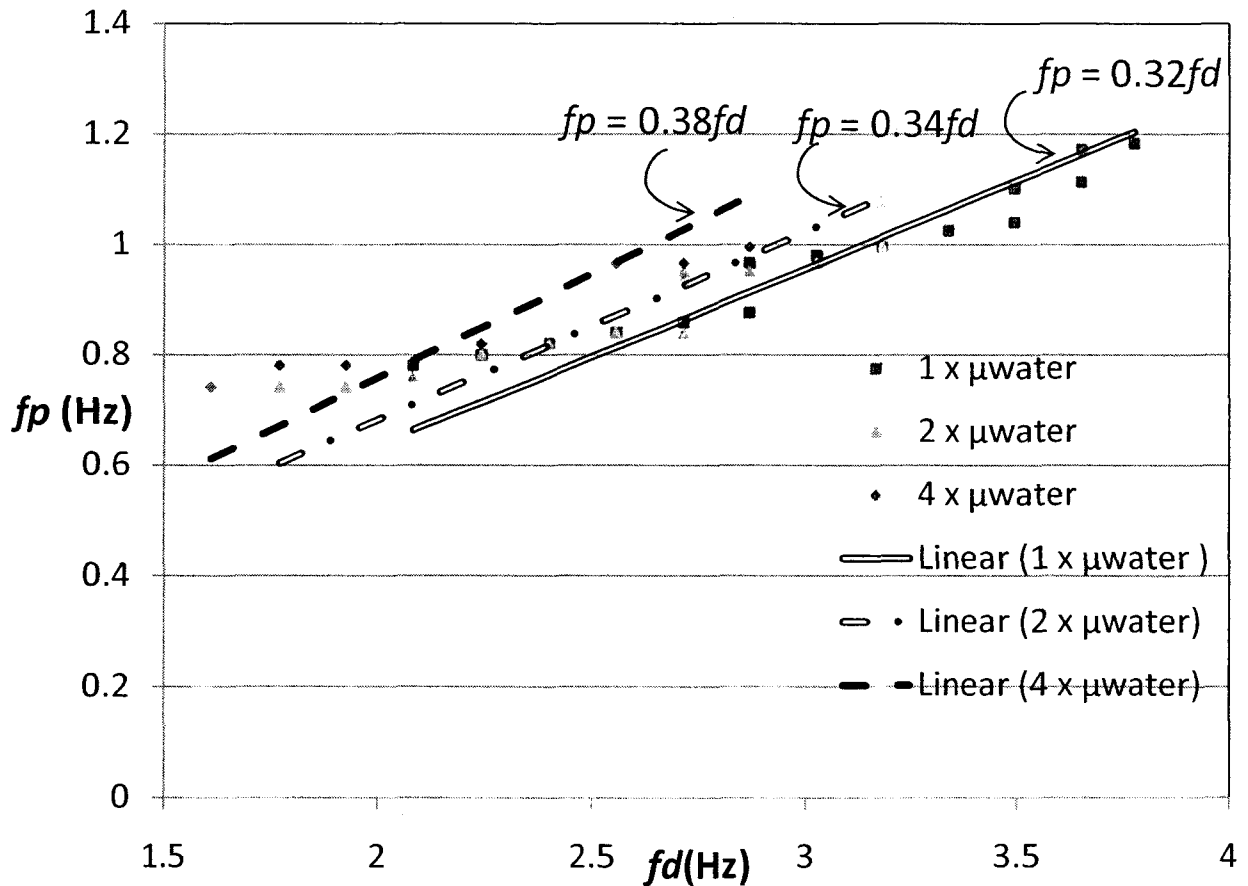
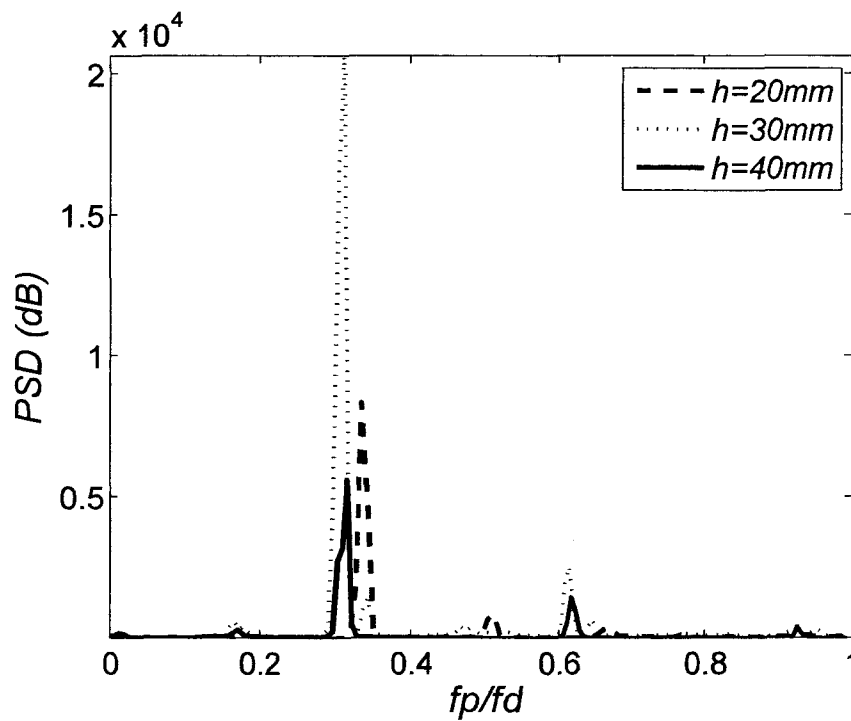


**Figure 20** Linear fitted slopes for frequency propagation at  $h_i = 20$  mm.

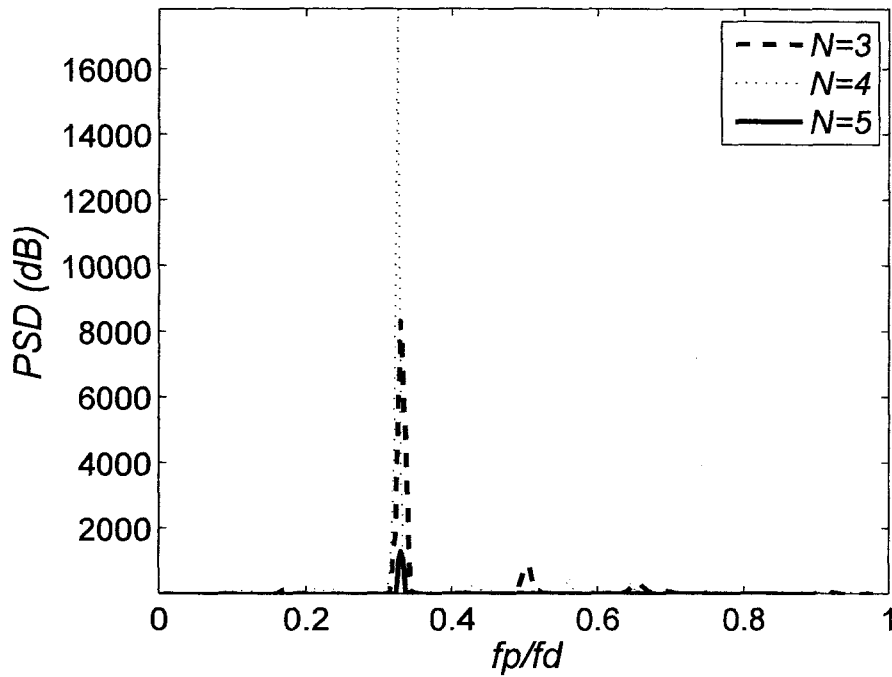


### 3.4 Effect of density on pattern's rotating frequency

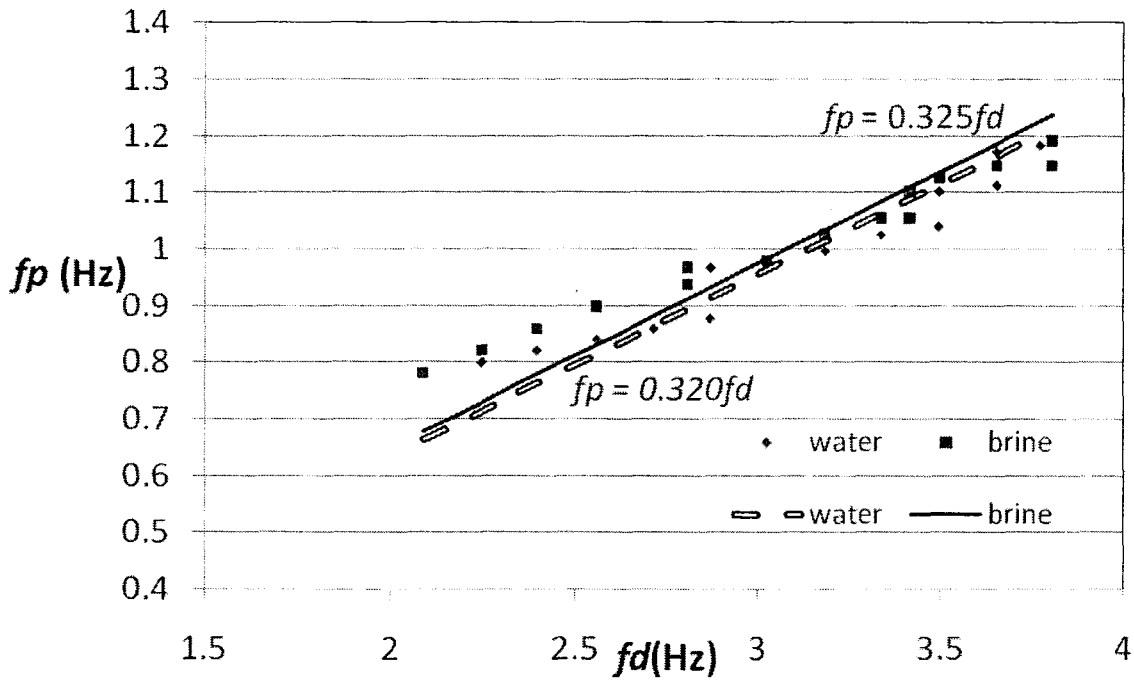
The change of the pattern's frequency with increasing disc speed followed almost the same trend as using water with mode-locking frequency ratio of approximately  $1/3$  (see figure 21(c)). Figures 21 (a) and (b) shows the superposition of the extracted power spectra for triangle patterns at the three different studied heights and all mode shapes recognized at  $h_i = 20$  mm, respectively, using brine as the working fluid. A negligible increase in the polygonal patterns' rotational frequencies has been recognised when slightly increasing the working fluid's specific gravity. As a result, it could be concluded, that slightly increasing the specific gravity of the working fluid has essentially no influence on the polygonal patterns' rotating speeds.



(a)



(b)



(c)

**Figure 21** (a) Power spectra superposition for triangular pattern using brine at three different heights; (b) Power spectra superposition at  $h_i = 20$  mm for all mode shapes using brine; and (c) Linear fitted slopes for frequency propagation.

### 3.5 Concluding remarks

In this chapter, the effect of varying the working fluid's viscosity has been analyzed based on three main criteria, being the polygonal patterns instability formation, limits of endurance and rotational speeds. Phase diagrams defining the observed polygonal patterns at three different initial heights and along a certain range of viscosity values have been constructed. Two main observations have been recognized. First, it was found that gradually increasing the viscosity of the rotating fluid resulted in early developments and transitions of polygonal mode shapes in terms of disc's rotational speed. Second, the viscosity has been recognized as a destructive parameter of the polygonal instability observed under shallow liquid conditions within the hollow vortex core. All mode shapes recognized using water as the working fluid have been destroyed and disappeared as the viscosity of the working fluid was increased gradually. Triangular patterns were the only long lasting stable shapes for all heights and viscosities values studied which might be recognized as the most persisting and stable polygonal pattern observed in such symmetry breaking phenomenon.

The second part of this chapter dealt with analyzing the variation in the rotating polygonal pattern's speeds. It has been confirmed that all mode shapes follow a constant increasing propagation of rotating frequency of about  $1/3$  (Vatistas et al. 2008). Furthermore, it was found that increasing the viscosity of the fluid resulted in significant increase in the liquids rotating speeds (up to 25% increase) for the same disc's speeds. An explanation for such observation might be the fact that, increasing the liquid's viscosity intensified the azimuthal shear forces experienced in the rotating flow, which has been confirmed by many studies as

being the main driving force for the development and propagation of such polygonal instabilities observed within a hollow vortex core (Jansson et al.2006, Gallaire and Chomaz 2003).

## Chapter 4

### Influence of viscosity on the transitional process between polygonal patterns

#### 4.1 Symmetry breaking in swirling flows

The identification and characterization of the transition from symmetrical to non-symmetrical swirling flows is of fundamental interest. As stated in chapter 1, many research studies were devoted in studying the mechanism and the nature of the symmetry breaking phenomenon observed in swirling flows within cylindrical containers.

Whether confined or free surface flow, the general conclusion from all studies confirmed the fact that, generally, the Reynolds number and aspect ratio (water initial height  $H$  / cylinder container radius  $R$ ) are the two main parameters influencing the symmetry breaking phenomenon's behaviour. Specifically, the shear forces between working fluids and the endwalls and/or between different flow regimes within the swirling flow are the dominant and original driving forces for such phenomenon occurrence. In fully filled confined flows, the flow is triggered by both sides and end walls while in open cylindrical containers, the top endwall does not exist and the surface acts freely. Vogel (1968) and Escudier (1984) studied the transitional process in confined flows and found that symmetry breaking occurs when a critical Reynolds number was reached for each different aspect ratio. Vogel (1968) used water as the working fluids in his study where he observed and defined a stability range, in terms of aspect ratio and Reynolds number, for the vortex breakdown phenomenon which occurred in the form of a moving bubble along the container's axis of symmetry. Escudier (1984) later extended the study by using an aqueous glycerol mixture (3 to 6 times the viscosity of water) and found that varying the working fluid viscosity caused changes in the critical Reynold's number values. He also

observed that for a certain range of aspect ratio and viscosity, the phenomenon of vorticity breakdown has changed in behaviour, revealing more vortices breakdown stability regions than the conventional experiments using water as the working fluid.

Where in open free surface containers under shallow liquid conditions using water as the working fluid, Vatistas (1990) studied the transitional flow visually and found that the range of the disc's RPM where the transitional process occurs shrink as the mode shapes number increase. Jansson et al. (2006) concluded that the endwall shear layers as well as the minute wobbling of the rotating disc are the main two parameters influencing the symmetry breaking phenomenon and the appearance of the polygonal patterns. Vatistas et al. (2008) studied the transition between polygonal patterns from  $N$  to  $N+1$ , using image processing techniques, with water as the working fluid and found that the transition process from  $N$  to a higher mode shape of  $N+1$  occurs when their frequencies ratio ( $N/N+1$ ) locks at  $(N-1/N)$ , therefore following a devil staircase scenario which also explains the fact that the transition process occurs within a shorter frequency range as the mode shapes increase. Speculating the transition process as being a bi-periodic state, the only way for such system to lose its stability is through frequency locking (Bergé et al. 1984). Recently, Ait Abderrahmane et al. (2009) studied the transition between equilibrium states under similar configurations using nonlinear theory approach and found that the transition occurs in two steps being, a quasi-periodic and frequency locking stages.

Having shown the effect of viscosity on the equilibrium states (i.e. stable polygonal patterns), in this chapter, the influence of liquid's viscosity on the swirling flows symmetry breaking mainly during the transition of mode shapes from  $N$  to  $N+1$  pattern will be studied using similar image processing approach used in Vatistas et al. (2008). It is interesting to find out

whether the liquid viscosity will have influence on the transition process as it the case in fully filled swirling flows or not.

## **4.2 Transition between equilibrium states using water as the working fluid**

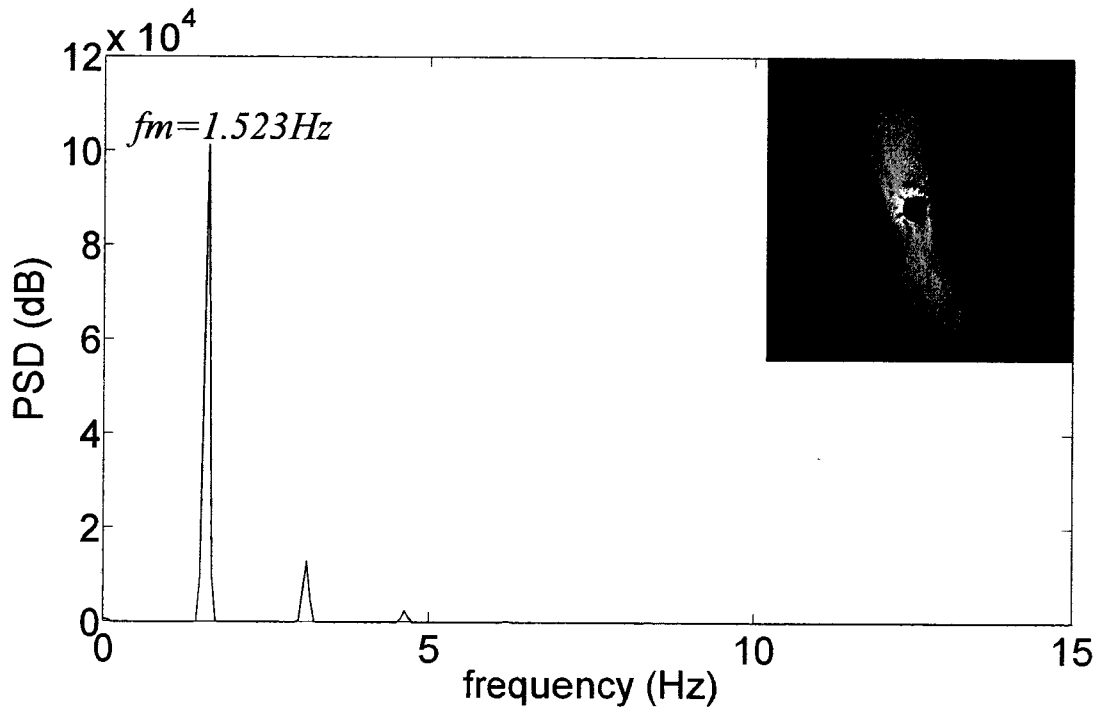
Experiments done by Vatistas et al. (2008) were performed using water at two initial heights (aspect ratios) of 30 and 40 mm. Due to the fact that the ranges of disc's RPM shrink significantly as the equilibrium states (mode shapes) increase, Vatistas et al. (2008) limited their study for the transition processes between modes 2 to 4. In this section, the transition process explained by Vatistas et al. (2008) will be confirmed and further extended by using water as the working fluid at two different initial heights (40 mm and 20 mm). The latter, allowed the transition processes between the rest of the mode shapes (4 to 6) to be captured and further analyzed.

### **4.2.1 Initial height $h_i = 40$ mm**

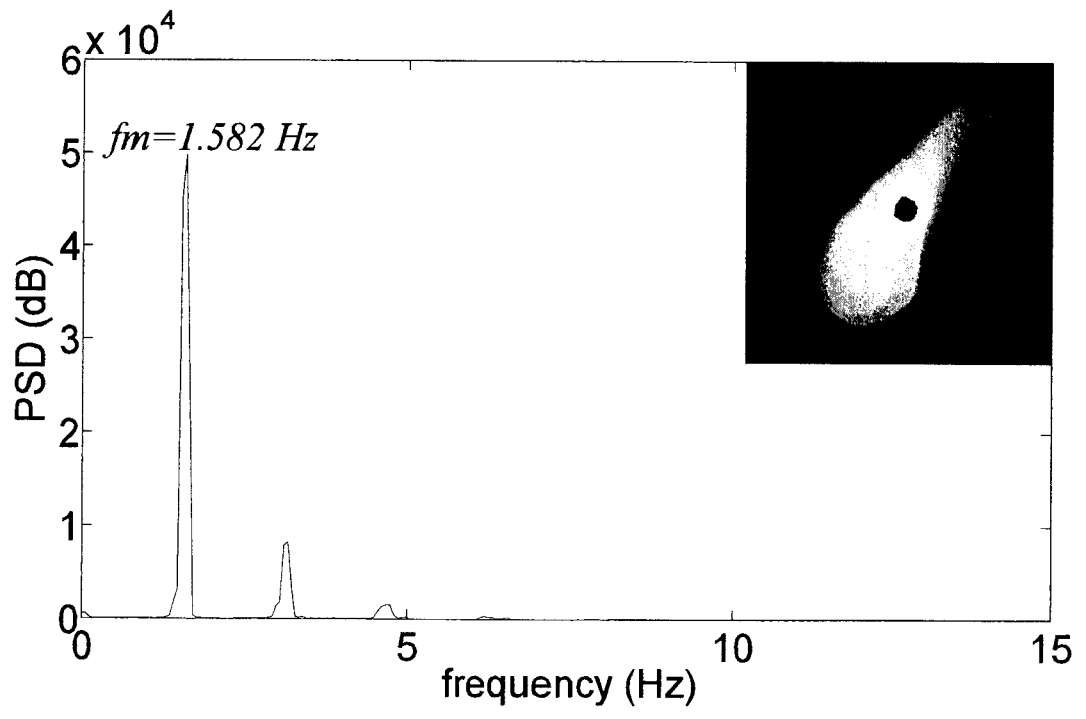
First experiment was done at initial height  $h_i = 40$  mm where transitions from  $N = 2 \rightarrow N = 3$  and  $N = 3 \rightarrow N = 4$  were recorded and analyzed using power spectral analysis as described in chapter 2. Similar to the procedure used in chapter 3, starting with stationary undisturbed flow, the disc speed was set to its starting point of 50 RPM and was then increased with increments of 1 RPM. Sufficient time was let after each increment for the flow to stabilize. At a disc speed of 2.43 Hz (146 RPM), the first mode shape (Oval) appeared on top of the disc surface. At the beginning of the  $N=2$  equilibrium state, the vortex core is fully flooded. While increasing the disc speed gradually, several sets of 1500-bit gray-scale images were captured and recorded. Recorded sets ranged 3 RPM in between. Systematic tracking of the patterns speed and shape evolution were recorded and the recorded images were processed using the same algorithm

procedure described in chapter 2. The evolution of the oval equilibrium state shape and rotating frequency is shown in figures 22(a-d). Starting with a flooded core at  $f_p = 0.762$  Hz in figure 22(a) where the vertex of the inverted bell-like shape free surface barely touched the disc surface, figure 22(b) shows the oval pattern after gaining more centrifugal force by increasing the disc speed by 9 RPM; the core became almost dry and the whole pattern gained more size both longitudinally and transversely with a rotating frequency of  $f_p = 0.791$  Hz. It is clearly shown that at this instant, one of the two lobes of the pattern became slightly fatter than the other. Figure 22(c) shows shape development and rotational speed downstream the  $N=2$  range of existence. It is important to mention that once the oval pattern is formed, further increase in the disc speed - therefore the centrifugal force applied on the fluid- curved up the oval pattern and one of the lobes became even much fatter giving it a quasi-triangular shape. Figure 22(d) features the end of the oval equilibrium pattern in the form of a quasi-triangular pattern and therefore the beginning of the first transition process ( $N=2$  to  $N=3$ ). The transition process was recorded, processed and the corresponding power spectrum was generated. The power spectral analysis revealed two dominant frequencies from the extracted time series function developed from the captured images: frequency  $f_m$  corresponds to the original oval pattern and frequency  $f_s$  corresponds to the growing subsequent wave  $N=3$ , which is a travelling soliton-like wave superimposed on the original oval pattern therefore forming the quasi-triangular pattern (Ait Aberrahmane et al. 2009). Further increasing the disc speed resulted in forming and stabilizing the triangular mode shape ( $N=3$ ) with a flooded core; both the troughs and apexes of the polygonal pattern receded and the core area shrank significantly.

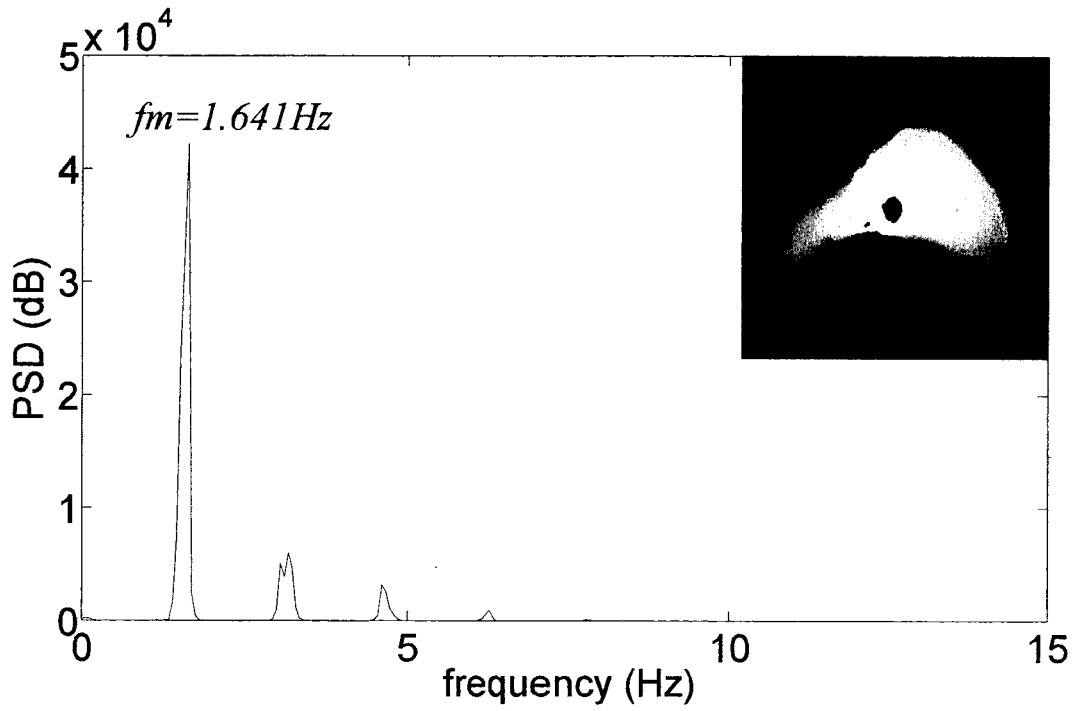




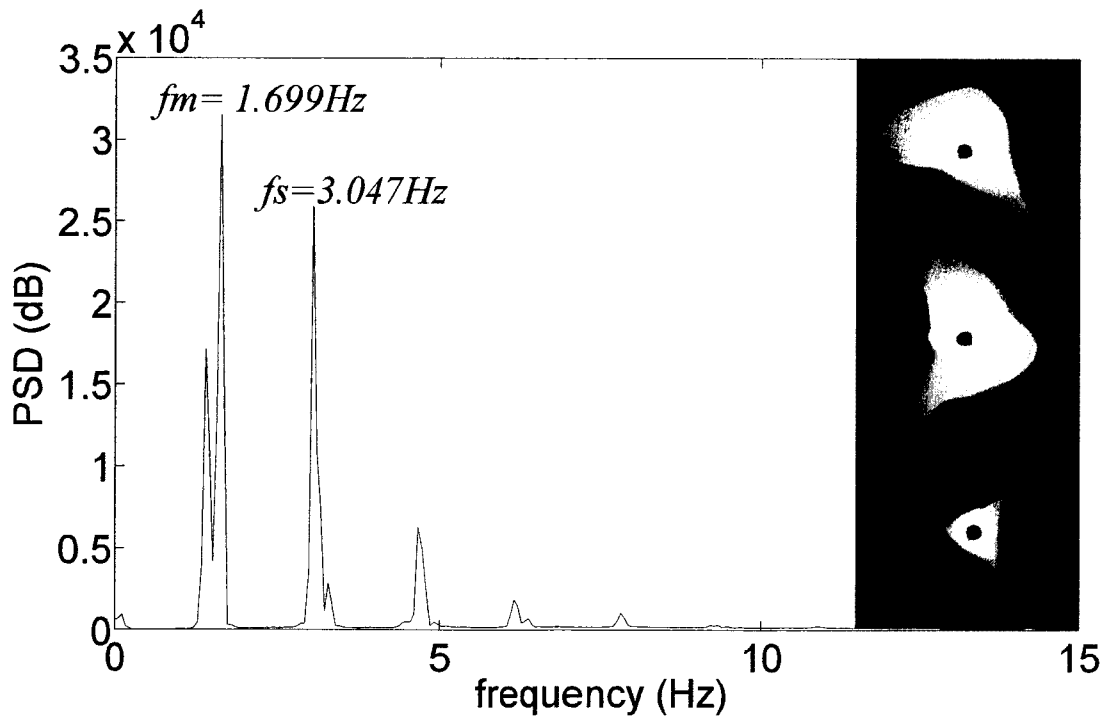
(a)



(b)



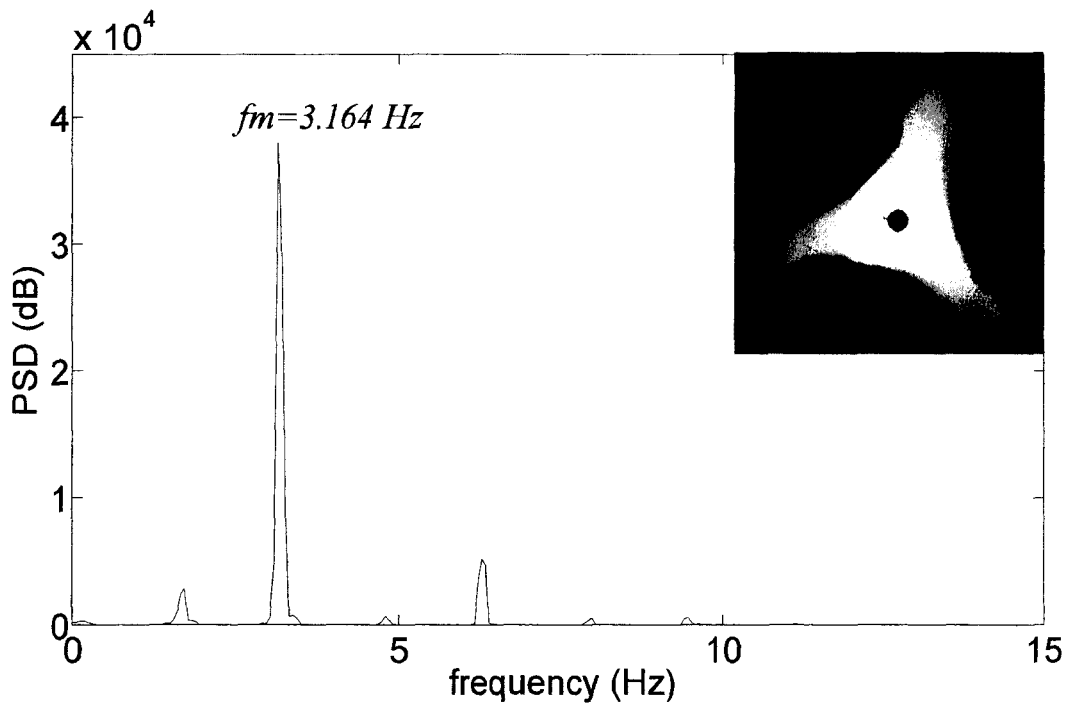
(c)



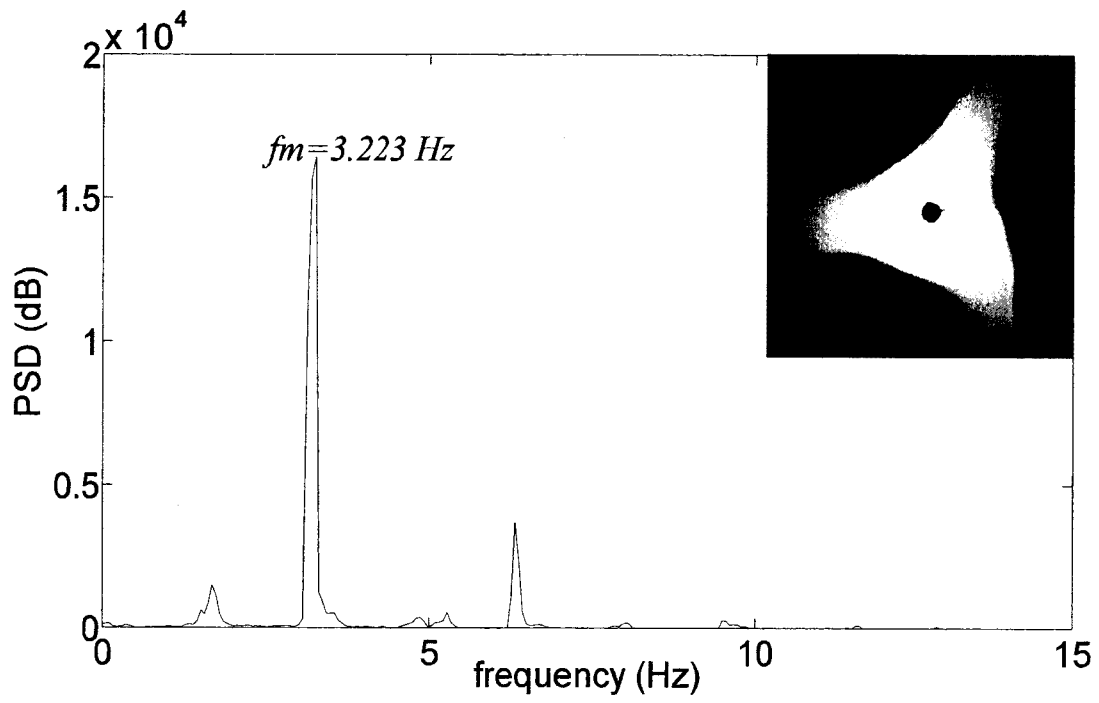
(d)

**Figure 22** (a), (b), (c) Oval pattern progression and corresponding power spectra; and (d) Oval to triangular transition  $N=2$  to  $N=3$  and corresponding power spectrum.

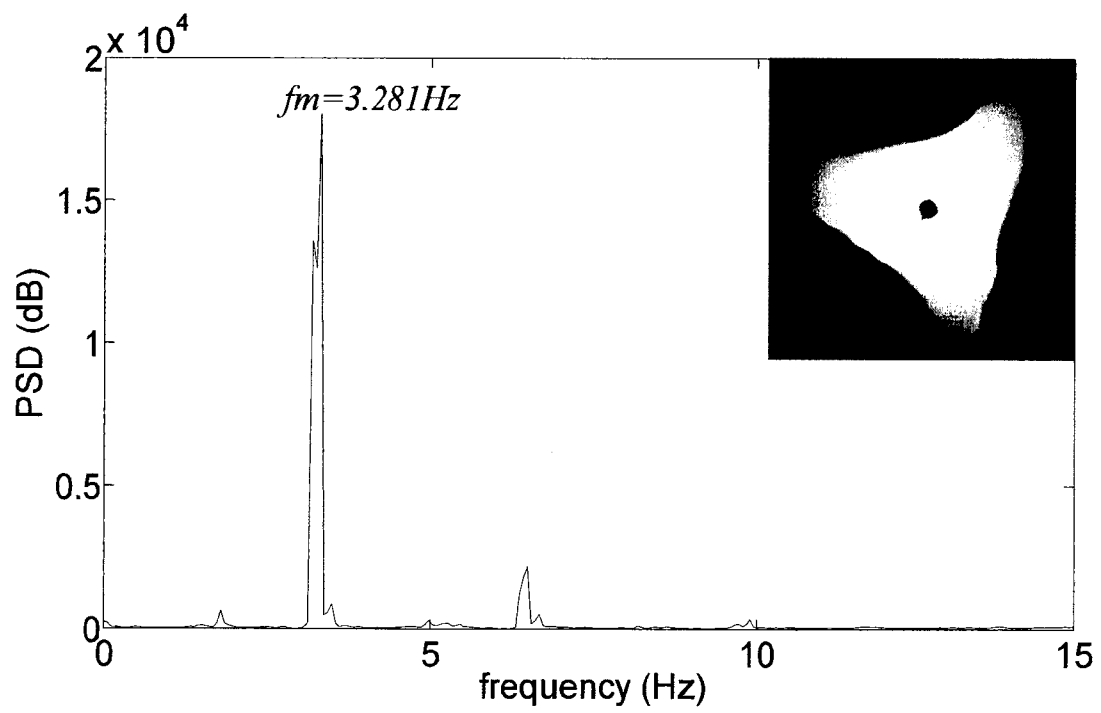
Following the same procedure, the development of the triangular pattern and its transition to square ( $N=4$ ) shape were recorded, image processed and analyzed. Figures 23 (a-e) show the power spectra plots and their corresponding sample image from the set recorded and used in generating each of the power spectra. Similarly, the behaviour of the oval pattern's shape development and transition was also respected for the triangular pattern evolution. The pattern's spin-up rate shows a linear trend as discussed in chapter 3.



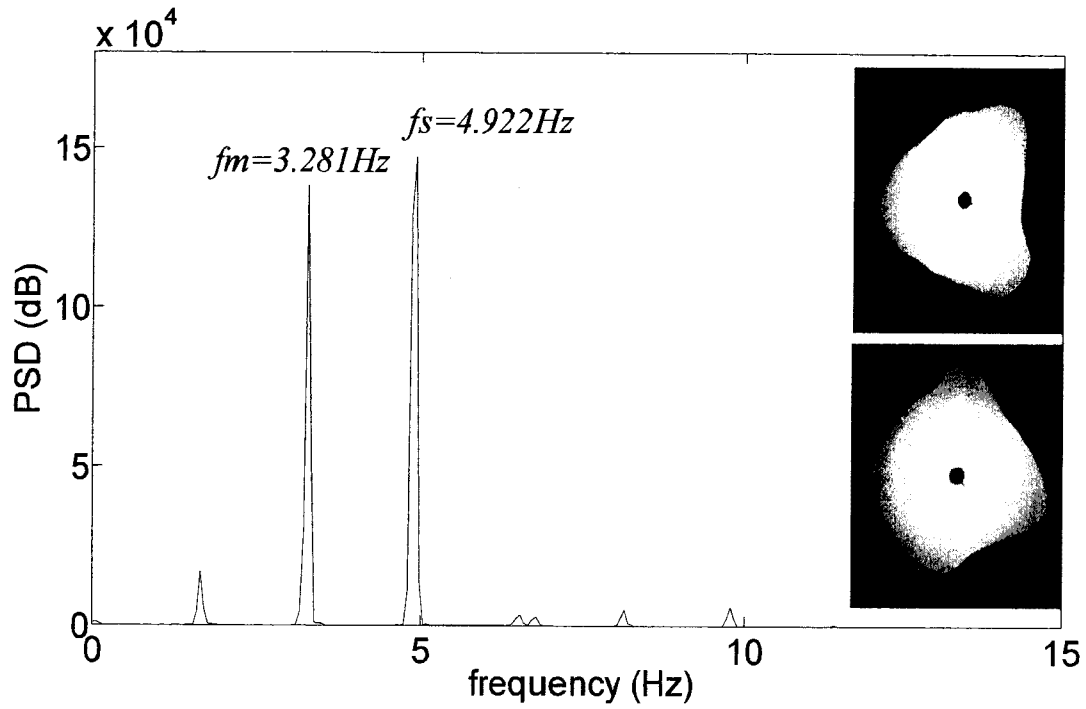
(a)



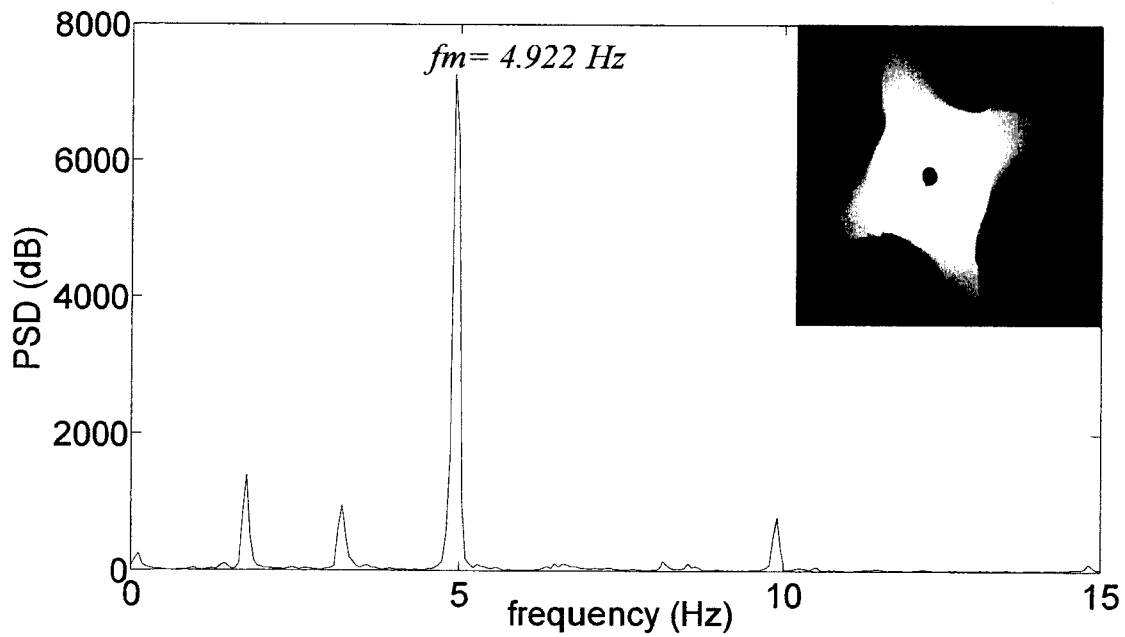
(b)



(c)



(d)



(e)

**Figure 23** (a), (b), (c) Triangular pattern progression and corresponding power spectra; (d) Transitional process from triangular to square pattern; and (e) Square pattern and corresponding power spectra.

Ait Aberrahmane et al. (2009) has described the transition process in the form of a rotating solid body  $N$  shape associated with a traveling “soliton” like wave along vortex core boundary layer. In this thesis, the evidence of such soliton-like wave is revealed. Figure 23 (a) shows the stable triangular pattern just few RPM downstream after the transition process took place. The equivalent evolution of the triangular pattern through its existing range is shown in figures 23 (a-c). Just before transition took place, colored images were recorded for better visualization. The colored images were found very useful in illustrating the observed stratification of the hollow vortex core where each colored layer indicates a unique water depth within the vortex core. It is worth noticing that the water depth increases continuously as we move away from the center of the disk (due to the applied centrifugal force). Starting with the central white region which corresponds to a fully dry spot of the core and going gradually through different water depth phases until reaching the black color region right outside the polygonal pattern boundary layer. Moving to the most interesting part which is the transition process, figure 24 features the quasi-square pattern mentioned earlier. Giving a closer look at the sequence of images, one could easily identify the following: the three lobes or apexes of the polygonal pattern are divided into one flatten apex and two almost identical sharper apexes. Keeping in mind that the disc, therefore the polygonal pattern, is rotating in the counter clockwise direction and that the sequence of images is from left to right, by tracking the flatten lobe, one could easily recognize that an interchange between the flatten lobe and the subsequent sharp lobe (ahead) takes place (see third row of images). In other words, now the flatten apex receded to become a sharp stratified apex and the sharp lobe gained a more flattened shape. Such result visually confirms the fact that transition takes place through a soliton-like wave travelling along the vortex core boundary but with a faster speed than the parent pattern. This first stage of

the transition process was called the quasi-periodic stage in Ait Abderrahmane et al. (2009) study. The quasi-periodic stage takes place in all transitions until the faster travelling soliton-like wave synchronizes with the patterns rotational frequency forming and developing the new higher state of equilibrium pattern. Vastistas et al. (2008) found that the synchronization process takes place when the frequencies ratio of both pattern ( $N$ ) and the subsequent pattern developed by the superimposed soliton wave ( $N+1$ ) lock at a ratio of  $(N-1)/N$ . Therefore, for transition from  $N=2$  to  $N=3$ , the synchronization takes place when the frequencies ratio are rationalized at  $1/2$ . And the transition  $N=3$  to  $N=4$ , takes place when the ratio between both frequencies are equal to  $2/3$ . In the above illustrated two transition processes, the frequency ratio for first transition was equal to  $f_N / f_{N+1} = f_m / f_s = 1.699/3.047=0.56 \approx 1/2$ . On the other hand, the second transition took place when  $f_N / f_{N+1} = f_m / f_s = 3.28/4.922=0.666 \approx 2/3$ . Both results confirm Vastistas et al. (2008) observation.

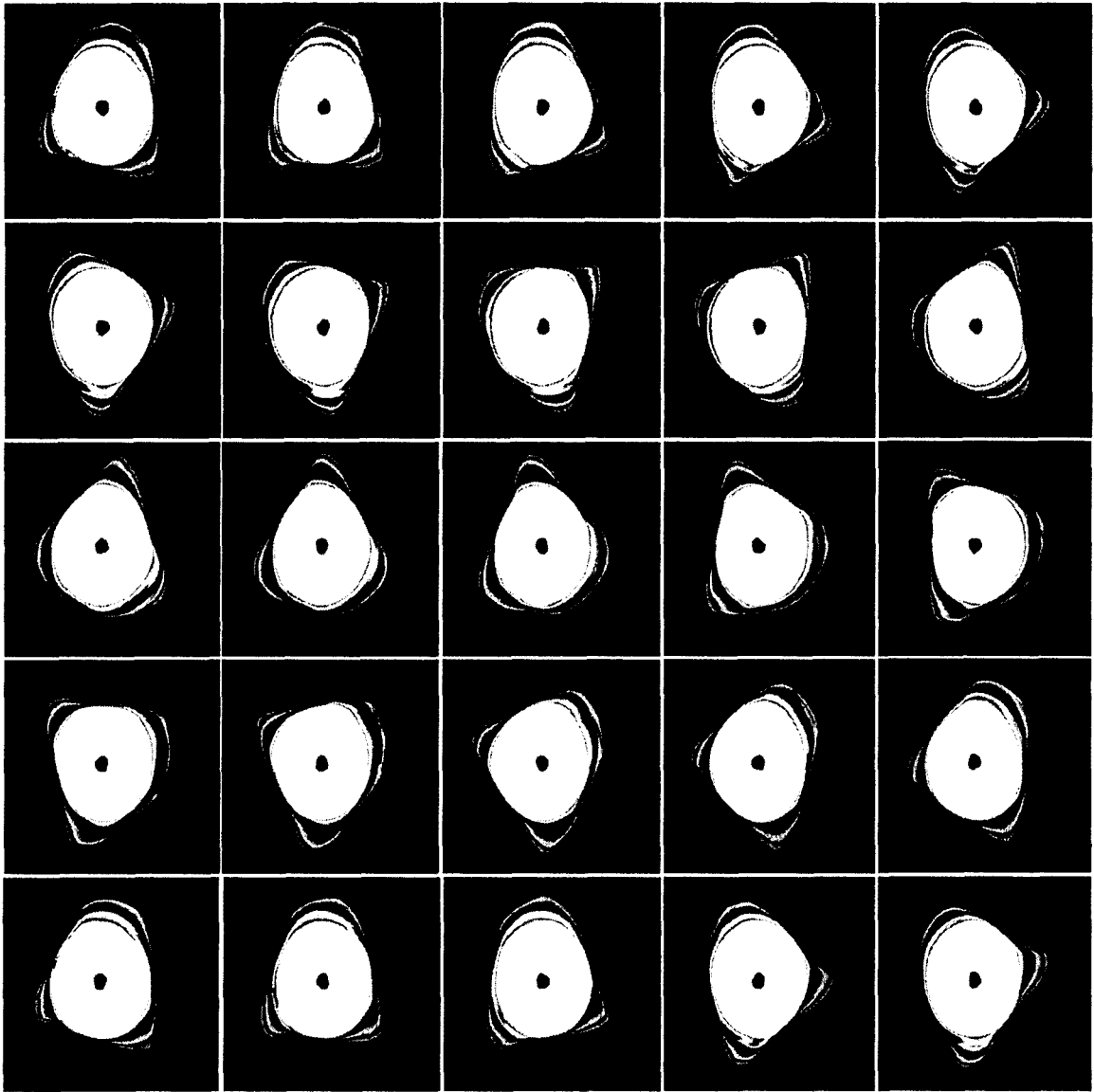
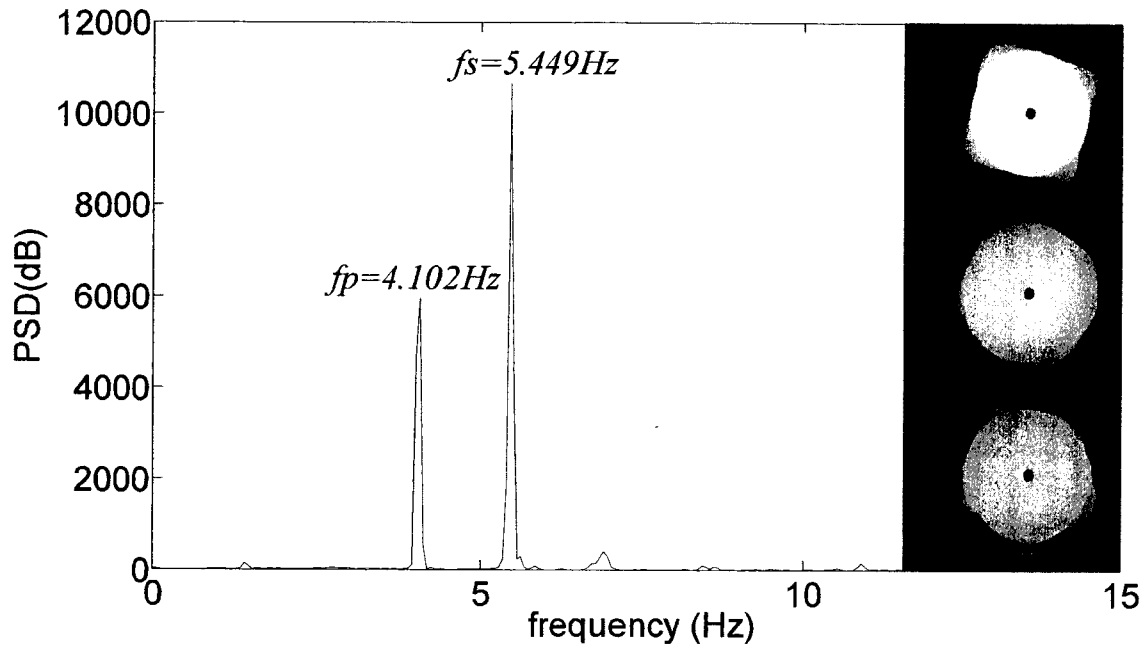


**Figure 24** Quasi-periodic state during triangular to square transition.

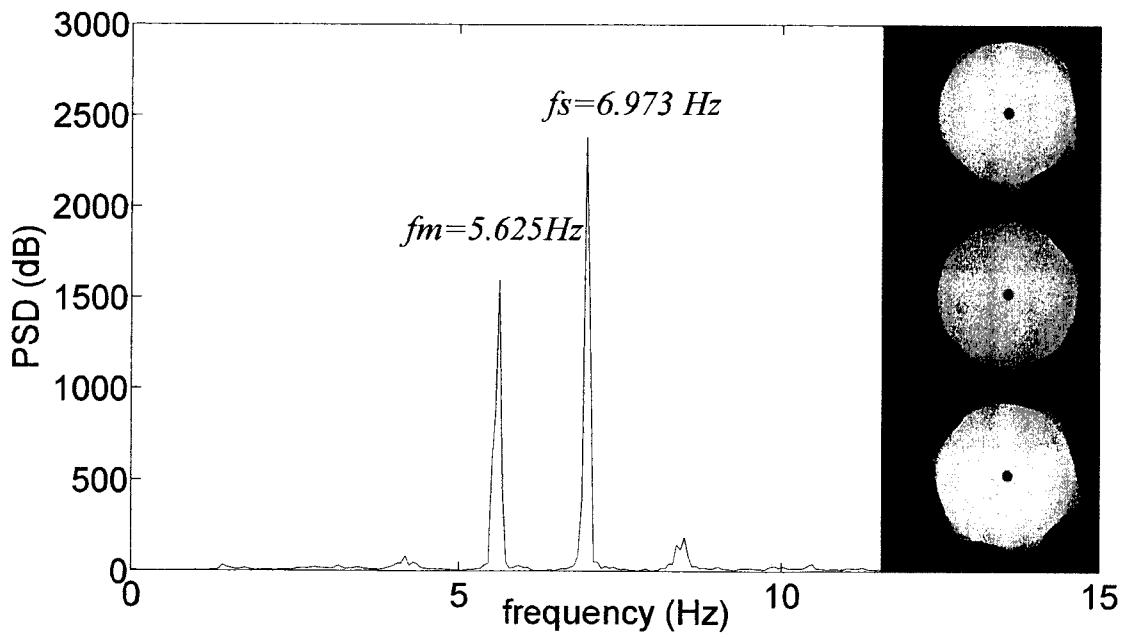


#### 4.2.2 Initial height $h_i = 20$ mm

Following the same trend, the second experiment was conducted using water at an initial height of 20 mm. At this low aspect ratio, transition between higher mode shapes was tracked and recorded. Using similar set-up and experimental procedure, the transition from square mode ( $N=4$ ) to pentagonal pattern ( $N=5$ ) and from pentagonal to hexagonal pattern ( $N=6$ ) were successfully recorded and image processed for the first time in such analysis. Following the same behaviour, the transition occurred at the expected frequency mode-locking ratio. Figure 25(a) shows the third polygonal transition, from  $N=4$  to  $N=5$ . The frequency ratio of the parent pattern to the soliton-like wave is  $f_m/f_s = 4.102/5.449 = 0.753 \approx 3/4$ . Similarly, figure 25(b) shows the transition power spectrum for the final transition process between polygonal patterns, which is from  $N=5$  to  $N=6$  polygonal patterns. The frequency ratio  $f_m/f_s = 5.625/6.973 = 0.807$  which is almost equal to the expected rational value  $4/5$ . With these two experimental runs, the explanation of the transition process between polygonal patterns observed within the hollow vortex core of swirling flows generated in cylinder containers under shallow water conditions is confirmed for all transitional processes.



(a)



(b)

Figure 25 (a) Square to pentagonal transition; and (b) Pentagonal to hexagonal transition.

### 4.3 Transition between equilibrium states using aqueous glycerol as the working fluid

One of the main objectives of this thesis is finding the influence of the liquid viscosity not only on the existence and limits of endurance of polygonal patterns, but also, the transitional process from any  $N$  mode shape to a higher  $N+1$  mode shape. As mentioned in chapter 3, eight different liquid viscosities were used in this study ranging from 1 up to 22 times the viscosity of water. All transitional processes between subsequent mode shapes were recorded, and acquired images were processed. Using the same procedure as in last section, the frequency ratio of the parent pattern  $N$  to the subsequent growing wave  $N+1$  has been computed and tabulated in table 1 as follows:

**Table 1** Transition mode-locking frequencies for different viscosity fluids.

Initial height ( $h_i$ )		$h_i = 20$ mm			$h_i = 30$ mm			$h_i = 40$ mm	
Transition ( $N$ ) - ( $N+1$ )		3 - 4	4 - 5	5 - 6	2 - 3	3 - 4	4 - 5	2 - 3	3 - 4
<b>Viscosity x <math>\mu</math> water</b>	<b>1</b>	0.697	0.787	0.829	0.545	0.68	0.74	0.558	0.69
		4.6%	4.9%	3.6%	9.0%	2.0%	1.13%	11.6%	3.5%
	<b>2</b>	0.667	0.747	--	0.558	0.671	--	0.557	0.678
		0.1%	0.4%	--	11.6%	0.7%	--	11.4%	1.7%
	<b>4</b>	0.64	--	--	--	0.671		0.557	0.686
		4.0%	--	--	--	0.7%		11.4%	--
	<b>6</b>	--	--	--	--	0.6667		0.55	--
						0.0%		10.0%	
	<b>8</b>					--		0.536	
								7.2%	
	<b>11</b>							0.58	
								16.0%	
	<b>15</b>							0.552	
								10.4%	
	<b>22</b>							0.559	
								11.8%	
									$f_m / f_s$
									% error

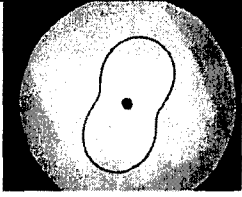
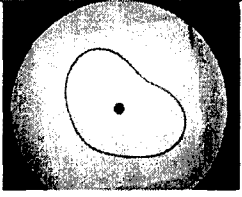
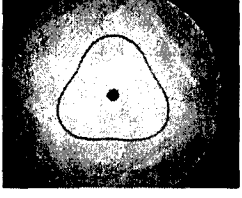
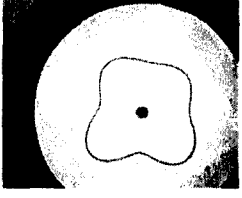
As shown in the table, the maximum deviation (% error) from the expected mode-locking frequency ratio ( $f_m/f_s$ ) always appeared in the first transition ( $N=2$  to  $N=3$ ). A reasonable explanation for such induced error is the fact that, the higher the number of apexes per full pattern rotation, the more accurate is the computed speed of the pattern using the measuring technique explained before. Therefore, throughout the conducted analysis, the most accurate pattern's speed is the hexagon and the least accurate is the oval pattern. Apart from that significant deviation, one can confidently confirm that even at relatively higher viscous swirling flows, the transition between polygonal patterns instabilities takes place when the parent pattern ( $N$ ) frequency and the developing pattern ( $N+1$ ) frequency lock at a ratio of  $(N-1)/N$  (Vatistas et al. 2008).

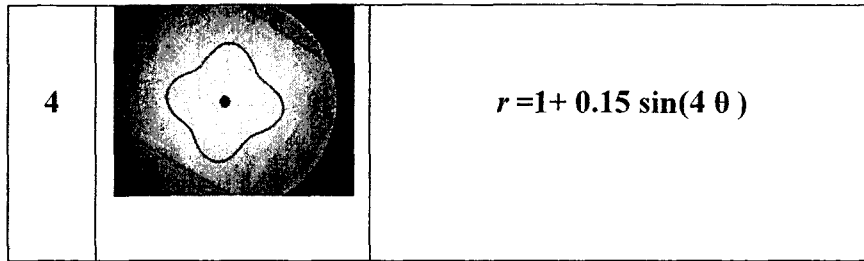
#### **4.3.1 Confirmation of the quasi-periodic stage in polygonal patterns transition**

As explained earlier, transition has been found to occur in two main stages being the quasi-periodic and the frequency-locking stages (Abderrahmane et al. 2009). In the last section, it was found that frequency mode-locking does exist in polygonal patterns transition irrelative of the mode shapes, liquid heights and the liquid viscosity (within the studied region). In this section, the quasi periodic phase will be further proven and confirmed. Earlier in this chapter, the quasi-periodic state in the transition of  $N=3$  to  $N=4$ , using water as the working fluid, was observably described in figure 24. To further analyze the quasi-periodic stage, a technique has been developed which animates the actual polygonal patterns instabilities but without the existence of the speculated travelling soliton-like wave along the patterns boundary layer. Using MAPLE plotting program, all mode shapes replica have been plotted and printed. Table 2 shows the plots and their corresponding plotting functions. Printed figures were placed on the rotating

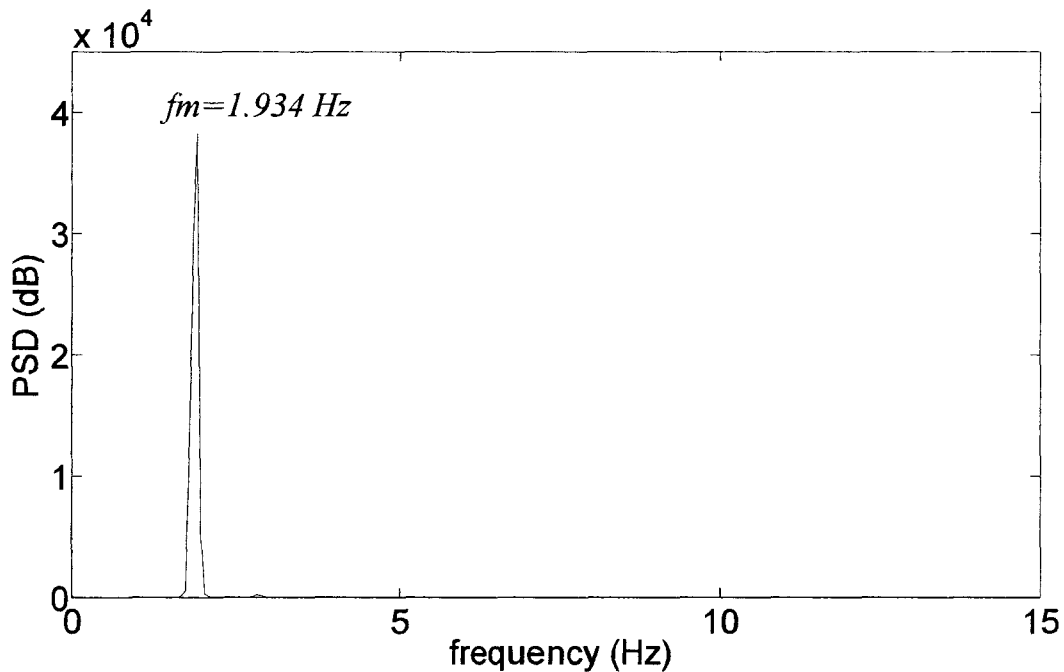
disc under dry conditions one at a time. The disc was rotated with corresponding pattern's expected speeds under normal working conditions. Such technique gave full control of the rotating pattern. Therefore, both speed and geometry of the patterns were known at all times. Sets of 1500 8-bit images were captured and processed using similar computing procedure.

**Table 2** Patterns replica with corresponding functions.

<i>N</i>	Pattern plot	Plot function
2		$r = 1 + 0.2 \sin(2 \theta)$
2 - 3		$r = 1 + 0.2 \sin(2 \theta) + 0.1 \sin(3 \theta + 1)$
3		$r = 1 + 0.1 \sin(3 \theta)$
3 - 4		$r = 1 + 0.1 \sin(3 \theta) + 0.15 \sin(4 \theta + 1)$



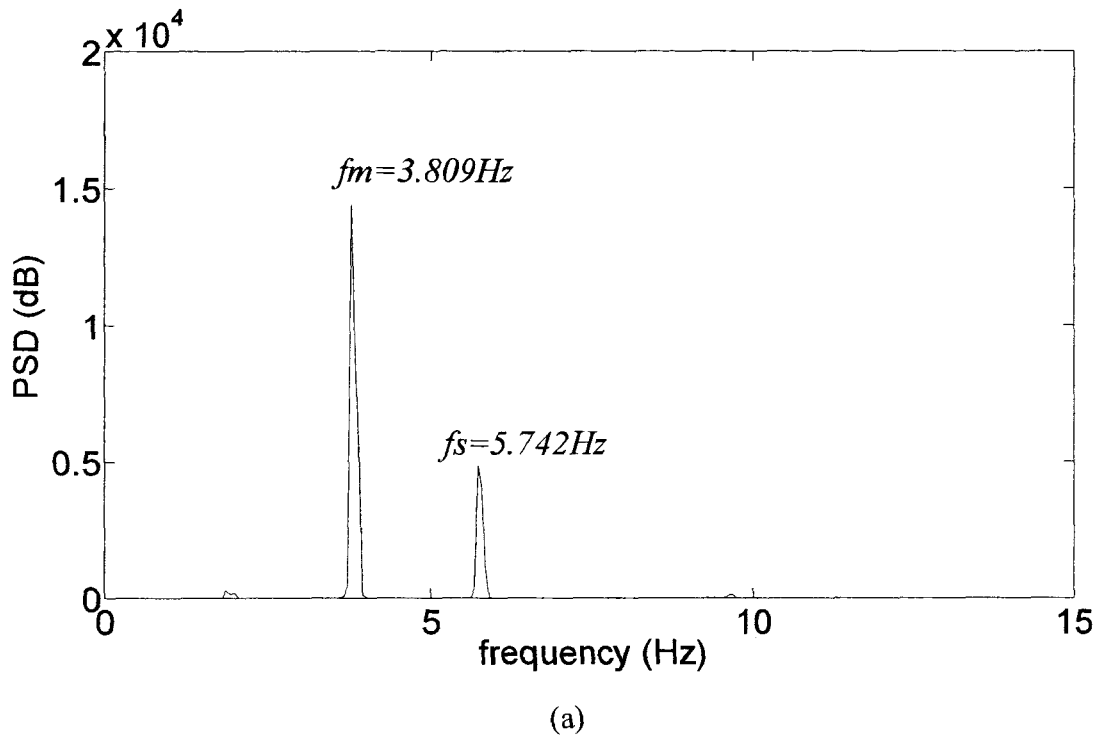
Power spectra of processed sets of images revealed similar frequency plots. Starting with the oval-like shape, the disc was rotated at a constant speed of 1 Hz and the power spectrum was generated from the extracted images and plotted as shown in figure 26.



**Figure 26** Power spectrum for  $N=2$  pattern replica.

Since the oval pattern speed is controlled in this case (by disc speed), the frequency extracted could have been presumed to be double the disc frequency (2 Hz). The actual

frequency extracted is shown in figure 26,  $f_m = 1.934$  Hz (3.3% error). Following the same procedure, other polygonal patterns replica were printed to the disc, rotated, captured and processed subsequently. Figures 27 (a) and (b) show the power spectra generated from rotating the quasi-triangular and the quasi-square patterns, respectively.



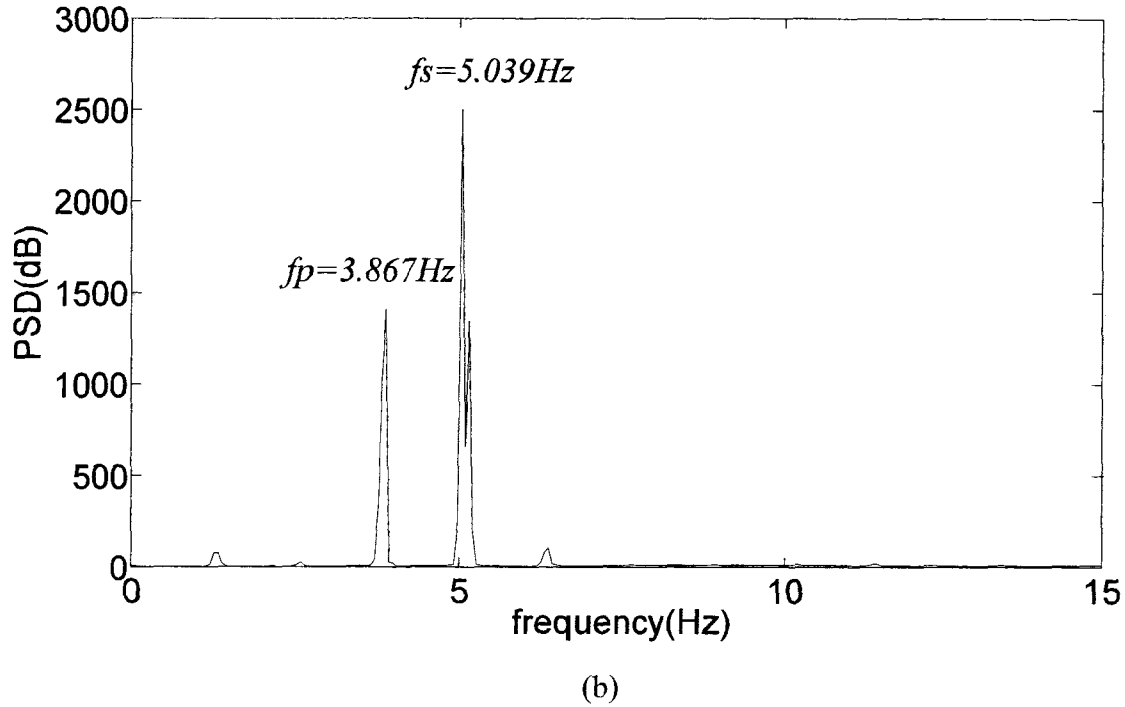


**Figure 27** Power spectrum of transition processes using patterns replica (a)  $N=2$  to  $N=3$ ; and (b)  $N=3$  to  $N=4$ .

Figure 27 (a) shows a power spectrum generated from the set of pictures featuring a quasi-triangular pattern captured at 30 fps. The power spectrum revealed two dominant frequencies being  $f_m=3.809$  Hz and  $f_s=5.742$  Hz corresponding to the oval and triangular patterns, respectively. Since the quasi-triangular pattern is stationary and under full control, it could have been presumed that the frequency ratio  $(N/N+1)$  would have a value of  $2/3$  since the replica pattern is generated by superimposing the oval and triangular functions. The actual extracted frequency was  $f_m/f_s=3.809/5.742=0.663 \approx 2/3$ . Comparing this frequency ratio with the real polygonal patterns mode-locking ratio  $1/2$  explained earlier in this chapter, it is clear that the ratio is totally different which proves that both patterns are not behaving similarly although having generally similar instantaneous geometry, therefore, the actual rotating pattern does not



rotate rigidly as the pattern replica does, but rather deforms in such a way that the ratio of the two frequencies is smaller which confirms the idea of the existence of the fast rotating soliton-like wave ( $f_s$ ).

Indeed, moving to the second transition process, triangular to square, as shown in figure 27(b). The frequency ratio was found to be  $3/4$  as expected since the function used to plot the quasi-square pattern is the superposition of both functions used in plotting the pure triangular and square patterns shown in table 2. Comparing this ratio with the actual mode-locking ratio  $2/3$  observed with real polygonal patterns, it is clearly obvious that the ratio is still smaller which respects the existence of a faster rotating wave along the triangular pattern boundary that eventually develops the subsequent square pattern as visualized earlier using the colored images. From these two experiments, along with the visual inspection discussed earlier in this chapter, the existence of the fast rotating soliton-like wave ( $N+1$ ) along the parent pattern boundary layer ( $N$ ) is verified, therefore, the quasi-periodic stage.

#### **4.4 Concluding remarks**

In this chapter, the transition process experienced between polygonal patterns instabilities observed within the hollow vortex core of rotating flows in cylindrical container has been analyzed. In the experiments of Ait Abderrahmane et al. (2009), the transition between polygonal patterns was explained to occur through two main phases. The first phase included a quasi-periodic behaviour between the two mode shapes included in the transition. The second stage included frequency mode-locking of both subsequent patterns when the bi-periodic state loses its stability through synchronization of both frequencies (Bergé et al. 1984). In this thesis, both stages have been considered individually and the explanation of Ait Abderrahmane et al. (2009)

was further validated and analyzed. First, the quasi-periodic stage was tackled using two different techniques, being a natural visually-based technique and an ad-hoc animated technique. The first technique was performed by simply recording a sequence of colored images of the transitional processes between different polygonal patterns and analyzing the behaviour of the varying stratification of the pattern's boundary with time. Although, from the visual point of view, the existence of a fast moving wave along the parent pattern boundary confirms explanation of Ait Abderrahmane et al. (2009), another method was implemented to further enhance that proof. This method considered plotting similar patterns replica using MAPLE program, attaching them to the disc's top surface and reproducing similar experiments but under dry conditions. Images of the artificial polygonal patterns were captured, processed and finally compared with the original experiments considered using real flows. The processed data have pointed out a significant conceptual idea that gave a complete meaningful confirmation of the first transitional stage. If the real quasi-polygonal patterns were rigidly rotating, the frequency ratio of both superimposed wave functions would have been proportional to their number of corners which is not the case here. The second part of this chapter dealt with the second stage of polygonal instabilities transition which includes frequency mode-locking (synchronization) of subsequent polygonal patterns. The frequency mode-locking between any  $N$  sided polygonal pattern to the subsequent  $N+1$  pattern was confirmed to follow a devil staircase scenario (Vatistas et al. 2008) following a consistent ratio of  $N-1/N$ . Although the liquid viscosity was found to vary the existence, limits of endurance and relative speeds of the polygonal patterns, the frequency mode-locking ratio of subsequent patterns was found to be respected irrespective of the fluid viscosity and mode shapes. In this thesis, the transitions between high mode shapes

were captured and further analyzed, therefore completing the extensive explanation done by Ait Abderrahmane et al. (2009).

## Chapter 5

### Conclusion

The main objective of this research study was to determine the effect of liquid viscosity, of the working fluid, on the instability of polygonal patterns observed within the hollow vortex core generated by rotating a disc near the bottom of a cylindrical container under shallow liquid conditions. The lack of a systematic study in this topic made it of great interest to explore. The effect of liquid viscosity has been measured based on three main criteria, the existence and limits of endurance of polygonal patterns, the polygonal patterns rotating speed and finally, on the transitional behaviour between subsequent polygonal patterns. The viscosity was varied by mixing glycerol with tap water. Gradually increasing the liquid's viscosity was found to vary the existence and limits of endurance of the polygonal instabilities observed within the hollow vortex core. The limits of endurance of all polygonal patterns were found to decrease significantly by increasing the liquid viscosity until all mode shapes were eventually destroyed and never recognized, beginning with high mode shapes and progressing to lower polygonal patterns. For all studied heights, increasing the viscosity initiated the instabilities earlier, therefore shifting the whole phenomenon towards lower values of disc speeds, which is consistent with the experiments done by Jansson et al. (2006) using ethylene glycol as the working fluid. Generally, the oval and triangular patterns were found to be the most persisting polygonal instabilities throughout the study. A reasonable explanation for such observation is the fact that, governing the swirling flow by Navier-Stokes equation, it is speculated that since the viscosity dominates the shear forces in the flow, therefore, it gives rise to the deviatoric stress tensor of the flow surface diverging its apexes and therefore distorting its geometry. Since the

apexes or corners of the polygonal patterns become less sharp as they increase in number, it is reasonable that mode shapes will lose their configuration progressively, starting with high mode shapes (least sharp) and progressing to low mode shapes (most sharp), as the viscosity is increased gradually making the triangular and oval patterns the longest lasting patterns recognized.

Another new finding concerns the polygonal patterns rotational speed variation as the disc speed was increased. Gradually increasing the liquid viscosity was found to increase the relative speed of the polygonal patterns. A maximum speed increase of 25% was recognized by increasing the working fluid viscosity to 22 times the viscosity of water, at initial height of 40 mm. The general polygonal pattern speed ( $f_p$ ) propagation rate with increasing disc speed ( $f_d$ ) was found to concise approximately around  $f_p/f_d=1/3$  which confirms the results obtained by Vatistas et al. (2008).

Mixing glycerol with water has not only increased the liquid viscosity, but its specific gravity as well. Brine was used in the experiments as the working fluid to vary the specific gravity of the liquid solely without significantly changing any other parameters. It was found that increasing the specific gravity of water by 25% had an almost negligible effect on all studying criteria as compared to the effect associated with varying the viscosity.

The effect of varying the working fluid viscosity on the transitional processes between subsequent polygonal patterns was addressed in this thesis. In his study, Ait Abderrahmane et al. (2009) considered the polygonal patterns transitional process to take place through two subsequent phases: a quasi-periodic stage and a frequency mode-locking stage. Both stages have been further confirmed and analyzed. The transitional process was analyzed using the same 8

different viscosity mixtures. The quasi-periodic stage was first tackled using two different techniques, a visual method and an animated method. The deformation of the colored stratified boundary layers of polygonal patterns were inspected during transition process of polygonal patterns and the existence of a fast rotating wave-like deformation was recognized which confirms the idea of the co-existence of a soliton-like wave that initiates the quasi-periodic stage at the beginning of the transition. In order to further materialize this observation, experiments were re-conducted using fixed patterns replica featuring the quasi-periodic geometry of polygonal patterns under dry conditions. Such technique allowed full control of the patterns geometry and speed at all time, therefore working as a reference to the real experiment performed under wet conditions. The experiments revealed an interesting basic idea that was useful when addressing the significant difference in behaviour associated with the real patterns transitions. The second part of the transition process included the frequency mode-locking ratio of subsequent patterns. Dealing with the first part of the transition process as being a bi-periodic state or phase, in order for such state to lose its stability, a synchronization event has to occur (Bergé et al. 1984). This synchronization has been confirmed to occur when the frequency ratio of the parent pattern  $N$  to the subsequent pattern  $N+1$  rationalized at  $(N-1)/N$  value (Vatistas et al. 2008). The frequency mode-locking phenomenon was found to be respected even at relatively higher viscosity fluids when mixing glycerol with water.

## **5.1 Contribution to knowledge**

Despite some evidences of the important role of the fluid viscosity on the polygonal pattern instabilities observed within the hollow vortex core, a systematic study has not yet been carried out. This thesis contributed to the understanding of the role of viscosity in the development, evolution, propagation speed and transition processes of the polygonal instabilities experienced within hollow vortex core. With this study, one could confidently recognize the role of the shear stresses experienced within swirling flows on the symmetry breaking and polygonal insatiability experienced within cylinder containers by a rotating disc near its bottom under shallow liquid conditions.

## References

- H. Ait Abderrahmane (2008) *Two Cases of Symmetry Breaking of Free Surface Flows*. Ph.D. Thesis, Concordia University, Montreal, Canada.
- H. Ait Abderrahmane, M.H.K. Siddiqui and G.H. Vatistas (2009) Transition between Kelvin's equilibria. *Phys. Rev. E* 80, 066305.
- M. Allison, D.A. Godfrey and R.F. Beebe (1990) A wave dynamic interpretation of Saturn's Polar hexagon. *Science* 247(4946), 1061-1063.
- G.K. Batchelor (2000) *An Introduction to Fluid Dynamics*. Cambridge University Press.
- H.B. Bluestein and A.L. Pazmany (1999) Observations of tornadoes and other convective phenomena with a mobile, 3-mm wavelength, Doppler radar. *Bulletin of the American Meteorological Society* 81 (12).
- M. Brøns, L.K. Voigt and J.N. Sørensen (2001) Topology of vortex breakdown bubbles in a cylinder with a rotating bottom and a free surface. *J. Fluid Mech.* 428, 133-148.
- Dow Chemical Company (1995-2010).
- P.W. Duck and M.R. Foster (2001) Spin-up of homogeneous and stratified fluids. *Annu. Rev. Fluid Mech.* 33, 231-63.
- J.E. Curtis and D.G. Grier (2004) Modulated optical vortices. *Optical Society of America* 28, 872-874.
- C.F. Driscoll and K.S. Fine (1990) Experiments on vortex dynamics in pure electron plasmas. *Phys. Fluids* B2, 1359.
- D. Durkin and J. Fajans (2000) Experiments on two-dimensional vortex patterns. *Phys. Fluids* 12, 289.
- M.P. Escudier (1984) Observations of the flow produced in a cylindrical container by a rotating endwall. *Experiments in Fluids* 2, 189-196.
- W.G. Fröh and P.L. Read (1999) Experiments on a barotropic rotating shear layer. Part 1. Instability and steady vortices. *J. Fluid Mech.* 383, 143-173.
- F. Gallaire and J.M. Chomaz. (2003) Instability mechanisms in swirling flows. *Phys. Fluids* 15 (9), 2622.



- D.A. Godfrey (1988) A hexagonal feature around Saturn's North Pole, *Icarus* 76, 335-356.
- R.C. Gonzalez, R.E. Woods, and S.L. Eddins (2004) *Digital Image Processing Using MATLAB*. 7<sup>th</sup> edition. Prentice Hall.
- H.P. Greenspan (1990) *The Theory of Rotating Fluids*. Breukelen Press, Brookline.
- N. Gregory, J.T. Stuart and W.S. Walker (1955) On the stability of three-dimensional boundary layers with application to the flow due to a rotating disk. *Proc. Royal Society London A*. 248, 155-199.
- H. von Helmholtz (1858) Uber integrale der hydrodynamischen gleichungen, welche denwirbelbewegung entsprechen. *Journal fur die Reine and Angewandte mathematic* 55, 25-55.
- R. Hide and C.W. Titman (1967) Detached shear layers in a rotating fluid. *J. Fluid Mech.* 29, 39-60.
- A.H. Hirsra, J.M. Lopez and R. Miraghaie (2002) Symmetry breaking to a rotating wave in a lid-driven cylinder with a free surface: Experimental observation. *Phys. Fluids* 14, L29.
- E.J. Hopfinger and G.J.F. Van Heijst (1993) Vortices in rotating fluids. *Annu. Rev. Fluid Mech.* 25, 241-89.
- T.R.N. Jansson, M.P. Haspang, K.H. Jensen, P. Hersen, and T. Bohr (2006) Polygons on a rotating fluid surface. *Phys. Rev. Lett.* 96, 174502.
- L. Kelvin (1867) On Vortex Atoms. *Philosophical Magazine* 34, 15-24.
- L.G. Kurakina and V. I. Yudovichb (2002) The stability of stationary rotation of a regular vortex polygon. *American Institute of Physics* 12 (3).
- J.M. Lopez (2006) Rotating and modulated rotating waves in transitions of an enclosed swirling flow. *J. Fluid Mech.* 553, 323-346.
- J.M. Lopez, J.E. Hart, F. Marques, S. Kittelman and J. Shen (2002) Instability and mode interactions in a differentially driven rotating cylinder. *J. Fluid Mech.* 462, 383-409.
- J.M. Lopez (1998) Characteristics of endwall and sidewall boundary layers in a rotating cylinder with a differentially rotating endwall. *J. Fluid Mech.* 359, 49-79.

- J.M. Lopez, F. Marques, A.H. Hirta and R. Miraghaie (2004) Symmetry breaking in free-surface cylinder flows. *J. Fluid Mech.* 502, 99-126.
- B.J. Mason (1971) Global atmospheric research programme. *Nature* 233, 382-388.
- T. Maxworthy (1973) A vorticity source for large-scale dust devils and other comments on naturally occurring columnar. *J. of the Atmospheric Sciences* 30, 1717-1722.
- A.M. Mayer (1878) Floating Magnets, *Nature* 17, 487-488.
- R. Miraghaie, J.M. Lopez and A.H. Hirta (2003) Flow induced patterning at the air-water interface. *Phys. Fluids*. 15 (6).
- H. Niño and N. Misawa (1984) An experimental and theoretical study of barotropic instability. *J. Atmospheric Sciences* 41, 1992-2011.
- L.M. Polvani and D.G. Dritschel (1993) Wave and vortex dynamics on the surface of a sphere. *J. Fluid Mech.* 255, 35-64.
- S. Poncet and M.P. Chauve (2007) Shear-layer instability in a rotating system. *J. Flow Visualization and Image Processing* 14, 85-105.
- M. Rabaud and Y. Couder (1983) Instability of an annular shear layer. *J. Fluid Mech.* 136, 291-319.
- C. Roy, N. Schaeffer, S. Le Dizès and M. Thompson (2008) Stability of a pair of co-rotating vortices with axial flow. *Phys. Fluids* 20, 094101.
- A. Spohn, M. Mory and E.J. Hopfinger (1993) Observations of vortex breakdown in an open cylindrical container with a rotating bottom. *Experiments in Fluids* 14, 70-77.
- K. Stewartson (1957) On almost rigid rotations. *J. Fluid Mech.* 3, 17-26.
- V.E. Suomi and S.S. Limaye (1978) Venus: Further evidence of vortex circulation. *Science* 201, 1009-1011.
- Y. Takeda (1999) Quasi-periodic state and transition to turbulence in a rotating Couette system. *J. Fluid Mech.* 389, 81-99.
- Y. Tasaka and M. Iima (2009) Flow transitions in the surface switching of rotating fluid. *J. Fluid Mech.* 636, 475-484.
- J.J. Thomson (1883) *A Treatise on the Motion of Vortex Rings*. Macmillan and Co. 1883.

- J.A. Van De Konijnenberg, A.H. Nielsen, J. Juul Rasmussen and B. Stenum (1999) Shear-flow instability in a rotating fluid. *J. Fluid Mech.* 387, 177-204.
- G.H. Vatistas (1990) A note on liquid vortex sloshing and Kelvin's equilibria, *J. Fluid Mech.* 217, 241-248.
- G.H. Vatistas, H. Ait Abderrahmane and M.H.K. Siddiqui (2008) Experimental confirmation of Kelvin's equilibria. *Phys. Rev. Lett.* 100, 174503.
- G.H. Vatistas, J. Wang and S. Lin (1992) Experiments on waves induced in the hollow core of vortices. *Experiments in Fluids* 13, 377-385.
- H.U. Vogel (1968) *Experimentelle Ergebnisse über die laminare Strömung in einem zylindrischen Gehäuse mit darin rotierender Scheibe*. MPI für Strömungsforschung Bericht 6.
- J. Wang (1995) *On the Wave Activity within Vortex Cores*. Ph.D. Thesis, Concordia University, Montreal, Canada.
- E.J. Yarmchuck and M.J.V. Gordan (1979) Observation of stationary vortex arrays in rotating superfluid Helium. *Phys. Rev. Lett.* 43, 214-217.

## Appendix A

### MATLAB algorithm

```
%=====
close all
clear all
clc
i=3;
fname=int2str(i);
fname1='F:\h33water\266\pattern_000';
fname=strcat(fname1,fname);
fname=strcat(fname,'.bmp');
im=imread(fname);
im=im(1:1024,1:1200);
G=imhist(im)/numel(im);

i=501;
fname=int2str(i);
fname1='F:\h=30mm water\2.72t\pattern_0';
fname=strcat(fname1,fname);
fname=strcat(fname,'.tif');
im=imread(fname);
im=im(1:1024,1:1280);
G1=imhist(im)/numel(im);

i=1013;
fname=int2str(i);
fname1='F:\h=30mm water\2.72t\pattern_';
fname=strcat(fname1,fname);
fname=strcat(fname,'.tif');
im=imread(fname);
im=im(1:1024,1:1280);
G2=imhist(im)/numel(im);

K=1;
for j=1:1500
    K=K+1;
    %i=0000+(j-1);
    i=j;
    fname=int2str(i);
    if i<10
        fname1='F:\h33water\266\pattern_000';
    end
    if i>=10
        fname1='F:\h33water\266\pattern_00';
    end
    if i>=100
        fname1='F:\h33water\266\pattern_0';
    end
end
```

```

if i>=1000
fname1='F:\h33water\266\pattern_';
end
fname= strcat(fname1,fname);
fname= strcat(fname, '.bmp');
im=imread(fname);
im=im(1:1024,1:1200);
im=histeq(im,G);
im=intrans(im,'gamma',0.7);
if i<400
im=histeq(im,G);
end
if i>=400
im=histeq(im,G1);
end
if i>730
im=histeq(im,G2);
end

% figure
% imshow(bim)
h=fspecial('gaussian',25,25);
bim=imfilter(im,h,'replicate');
bim=im2bw(bim,37.5/255);
bim=imfill(bim,'holes');
bim=imclearborder(bim);
%figure;
%imshow(bim);
B0=boundaries(bim);d=cellfun('length',B0);[max_d,k]=max(d);b0=B0{k};[M,N]=size(bim);
a1=ones(1,10)/10;
% figure
% imshow(im)
% hold on
b0=filtfilt(a1,1,b0);
%plot(b0(:,2),b0(:,1));% b0(:,2)=X;b0(:,1)=Y
%plot(466,390,'k','MarkerSize',100);
% pause(0.5)
[st0(:,j),angle0(:,j),x0(j),y0(j)]=signature(b0);
for i=1:max(size(b0))
b0(i,1)=b0(i,1)-x0(2);
b0(i,2)=b0(i,2)-y0(2);
end
%figure,plot(angle0,st0);
fd=3.105/3;
Phi=(k-1)*2*pi*fd/30;
L=[0,0,1]';
C=zeros(max(size(b0)),1)';
D=zeros(3,max(size(b0)));
for i=1:max(size(b0))
A=[b0(i,2); b0(i,1); C(1,i)];
B=RotVecArAxe(A,L,Phi);
D(:,i)=B;
end
b1=D(2,:);b2=D(1,:);
b1=[b1 b2];

```

```

[st1(:,j),angle1(:,j),x1(j),y1(j)]=signature(b0);
[st2(:,j),angle2(:,j),x2(j),y2(j)]=signature(b1);
% figure,plot(angle2,st2);
% hold on
% plot(b1(:,2),b1(:,1),'r');
% pause(0.1)
% close
end
for j=1:360

    [p,f]=spectrum(st2(j,2:1:1500),512,256,512,30);

    P(:,j)=p(:,2);
end
Pm=mean(P');
figure(1)
semilogy(f,Pm,'k')
%=====

```

## Experimental apparatus

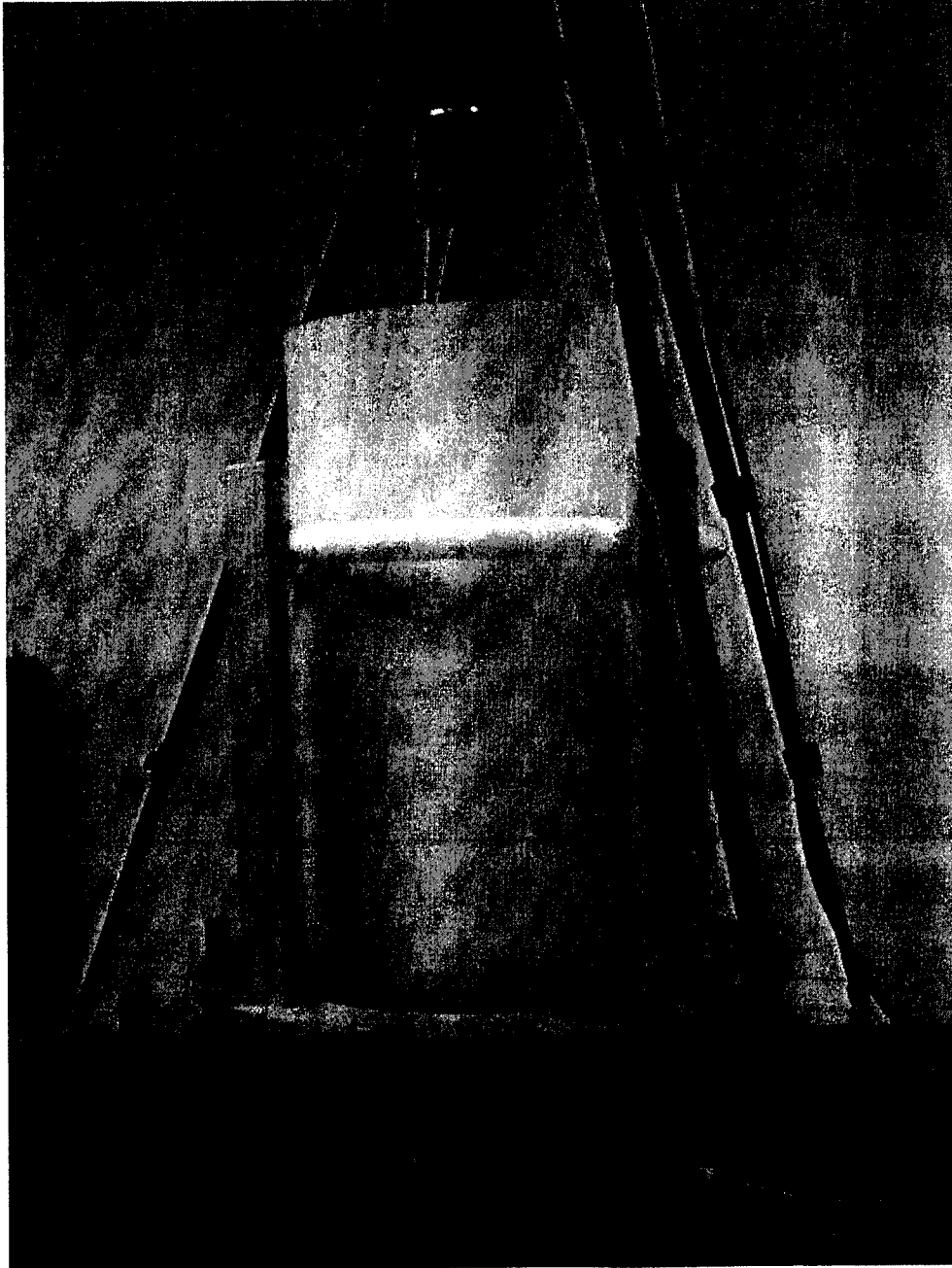


Figure 28 Experimental apparatus

# Viscosity of aqueous glycerine solutions

**Table 3** Viscosity of aqueous glycerine solutions

Glycerine percent weight	Temperature (°C)										
	0	10	20	30	40	50	60	70	80	90	100
0 <sup>(1)</sup>	1.792	1.308	1.005	0.8007	0.6560	0.5494	0.4688	0.4061	0.3565	0.3165	0.2838
10	2.44	1.74	1.31	1.03	0.826	0.680	0.575	0.500	–	–	–
20	3.44	2.41	1.76	1.35	1.07	0.879	0.731	0.635	–	–	–
30	5.14	3.49	2.50	1.87	1.46	1.16	0.956	0.816	0.690	–	–
40	8.25	5.37	3.72	2.72	2.07	1.62	1.30	1.09	0.918	0.763	0.668
50	14.6	9.01	6.00	4.21	3.10	2.37	1.86	1.53	1.25	1.05	0.910
60	29.9	17.4	10.8	7.19	5.08	3.76	2.85	2.29	1.84	1.52	1.28
65	45.7	25.3	15.2	9.85	6.80	4.89	3.66	2.91	2.28	1.86	1.55
67	55.5	29.9	17.7	11.3	7.73	5.50	4.09	3.23	2.50	2.03	1.68
70	76	38.8	22.5	14.1	9.40	6.61	4.86	3.78	2.90	2.34	1.93
75	132	65.2	35.5	21.2	13.6	9.25	6.61	5.01	3.80	3.00	2.43
80	255	116	60.1	33.9	20.8	13.6	9.42	6.94	5.13	4.03	3.18
85	540	223	109	58	33.5	21.2	14.2	10.0	7.28	5.52	4.24
90	1310	498	219	109	60.0	35.5	22.5	15.5	11.0	7.93	6.00
91	1590	592	259	127	68.1	39.8	25.1	17.1	11.9	8.62	6.40
92	1950	729	310	147	78.3	44.8	28.0	19.0	13.1	9.46	6.82
93	2400	860	367	172	89	51.5	31.6	21.2	14.4	10.3	7.54
94	2930	1040	437	202	105	58.4	35.4	23.6	15.8	11.2	8.19
95	3690	1270	523	237	121	67.0	39.9	26.4	17.5	12.4	9.08
96	4600	1580	624	281	142	77.8	45.4	29.7	19.6	13.6	10.1
97	5770	1950	765	340	166	88.9	51.9	33.6	21.9	15.1	10.9
98	7370	2460	939	409	196	104	59.8	38.5	24.8	17.0	12.2
99	9420	3090	1150	500	235	122	69.1	43.6	27.8	19.0	13.3
100	12070	3900	1410	612	284	142	81.3	50.6	31.9	21.3	14.8